Microstructure control and transport properties of incommensurate manganese silicide based alloys for thermoelectricity

Solange Vives

université de BORDEAUX

THÈSE PRÉSENTÉE

POUR OBTENIR LE GRADE DE

DOCTEUR DE L'UNIVERSITÉ DE BORDEAUX

ÉCOLE DOCTORALE DES SCIENCES CHIMIQUES

SPÉCIALITÉ : PHYSICO-CHIMIE DE LA MATIÈRE CONDENSÉE

Par **Solange Vivès**

Microstructure control and transport properties of incommensurate manganese silicide based alloys for thermoelectricity

---

Sous la direction de Stéphane Gorsse

Soutenue le 12 Novembre 2015

Membres du jury :

M. MAGLIONE Mario	Directeur de Recherche à l'ICMCB	Président
M. HAZOTTE Alain	Professeur à l'Université de Lorraine	Rapporteur
M. SNYDER Jeffrey	Professeur à l'Université de Northwestern	Rapporteur
M. ASHBY Michael	Professeur à l'Université de Cambridge	Examinateur
M. GODET Stéphane	Professeur à l'Université Libre de Bruxelles	Examinateur
M. GORSSE Stéphane	Maître de Conférences à Bordeaux INP	Examinateur

Remerciements

Cette étude s'est déroulée au sein de l'Institut de Chimie de la matière condensée de Bordeaux (ICMCB) et je tiens à remercier les deux directeurs successifs Messieurs Claude Delmas et Mario Maglione de m'avoir accueillie au sein de leur laboratoire où j'ai eu la chance de réaliser cette thèse.

Je remercie vivement Messieurs Alain Hazotte, professeur à l'Université de Lorraine, et Jeffrey Snyder, professeur à l'Université de Northwestern, d'avoir évalué ce travail. Messieurs Michael Ashby et Stéphane Godet de m'avoir honorée de leur présence dans ce jury de thèse. Enfin, Monsieur Mario Maglione d'avoir présidé ce jury. J'exprime toute ma reconnaissance à ce jury pour l'enthousiasme dont ils ont fait preuve envers ces travaux de thèse.

Au bout des trois années, une thèse est soutenue individuellement mais pour autant elle reflète un travail d'équipe ainsi que de belles rencontres. A ce titre je tiens à remercier toutes les personnes qui ont contribué à ce travail et je tiens particulièrement à citer les personnes qui suivent.

Mon "exceptionnel" directeur de thèse, Stéphane Gorsse, au delà des enjeux scientifiques liés à la thèse et pour lesquels je tiens à le remercier ; je tiens à souligner sa grande disponibilité, la totale confiance qu'il m'a accordée et les nombreuses occasions où il m'a donné l'opportunité de présenter mes travaux de recherche. Je mesure la chance que j'ai eue d'effectuer une thèse avec lui et au combien nos échanges m'ont permis de progresser dans ce métier.

Les partenaires de l'ANR PHIMS : Christelle Navone et Natalio Mingo (CEA) ; Jean-Claude Tedenac, Philippe Jund et Alexandre Berche (ICGM) et Joël Dufourcq (HBOB) pour les échanges productifs ainsi que pour leur aide lors des caractérisations.

Les personnes travaillant à l'ICMCB et à Placamat : Éric Lebraud (DRX), Étienne Gaudin (JANA), Rodolphe Decourt (diffusivité), François Weill (TEM), Marion Gayot (MEB), Alain Largeteau et U-Chan Chung-Seu (SPS), Michel Lahaye (EPMA), Sébastien Fourcade (expertise technique) pour leur aide lors des caractérisations et des expériences. Sans oublier Stéphane Toulin (Bibliothèque) et l'ensemble du personnel administratif de l'institut : Carole Malburet, Gérard Lebreton, Frédérique

Bonnet, Sylvie Létard et Sandrine Quillateau.

Les collaborations extérieures : Stéphane Godet et Loïc Malet (ULB) pour les analyses EBSD et pour la préparation des lames TEM ; Khalid Hoummada pour les expériences de sonde atomique ; et Gianluigi Botton pour les images en UHR-TEM.

Messieurs Yves Bréchet, Yannick Champion, Frans Spaepen, Hatem Zurob, Benji Maruyama et Dan Miracle pour les discussions autour de la métallurgie.

Les membres des groupes 1 et 4 de l'ICMCB pour les bons moments partagés pendant les pauses café tout au long de la thèse.

Les thésards, post-doc, permanents, CDD et stagiaires que j'ai pu côtoyer pendant ces trois années. Avec un mention spéciale pour : Matthieu, Guy-Marie, Olaia, Samuel, Seb, Maureen, Lionel, Diaa, Guillaume, Belto, Uli, Johann, Stéphanie, Baptiste, Maxime & JC, Lucile, la brigade du style : Olive & Alex, et tout ceux que j'oublie ... et bien sûr les membres du Crazy 23 : Fifi, Madhu, Volatiana, Tadhg & Eliane.

Enfin, ma famille, mes proches, mes amis et Baptiste pour leur soutien sans faille et pour leurs encouragements : merci du fond du cœur et ... vive les piles ! !

Contrôle de la microstructure et des propriétés de transport d'alliages incommensurables de siliciure de manganèse pour la thermoélectricité

Ces premières pages en français constituent un résumé de la thèse qui est par la suite rédigée en anglais. Dans un esprit de synthèse, ces quelques pages sont écrites autour d'une série de figures qui résument les faits marquants ainsi que les conclusions obtenues dans cette étude sur le contrôle de la microstructure et des propriétés de transport d'alliages incommensurables de siliciure de manganèse pour la thermoélectricité.

La thermoélectricité offre la possibilité de convertir directement la chaleur en électricité et inversement. Un générateur thermoélectrique est constitué de jonctions semi-conductrices de type n et p connectées thermiquement en parallèle et électriquement en série [1]. Un gradient thermique appliqué sur les faces du module force les électrons (dans le type n) et les trous (dans le type p) à migrer vers la face froide, ce qui génère un courant électrique entrainé par le flux de chaleur. L'efficacité de conversion d'un module thermoélectrique dépend de l'aptitude du matériau utilisé pour les jonctions à maintenir un gradient thermique entre la source chaude et la face froide, à générer un voltage par effet Seebeck et à conduire un courant électrique. Ces propriétés sont traduites au sein d'un indice de performance appelé figure de mérite (zT) qui permet de comparer les matériaux thermoélectriques (voir figure 1.a.).

Obtenir une telle combinaison de propriétés constitue un défit car elles sont inter-corrélées et s'opposent [2], cependant le meilleur compromis est obtenu pour certains semi-conducteurs (thermoélectriques) remplissant l'espace des propriétés entre les semi-conducteurs classiques et les métaux et alliages (voir figure 1.b.).

Appliquée au domaine de l'automobile la thermoélectricité permettrai de valoriser l'énergie dissipée sous forme de chaleur (70 % de l'énergie primaire combustible) en produisant de l'électricité via un générateur thermoélectrique placé sur le pot catalytique.

Cette thèse s'inscrit dans ce contexte; elle vise à obtenir un matériau thermoélectrique semi-conducteur de type p compatible avec une production de masse et respectant les critères de développement durable. Après une sélection des matériaux prenant en compte la performance dans la gamme de température visée (300-500°C), le monopole et la pénurie des matières premières, la toxicité, le coût

et l'impact environnemental ; les siliciures et notamment les siliciures de manganèse (appelés Higher Manganese Silicide, HMS, en anglais) de formule chimique $MnSi_\gamma$ ont été choisis (voir figure 1.c.).

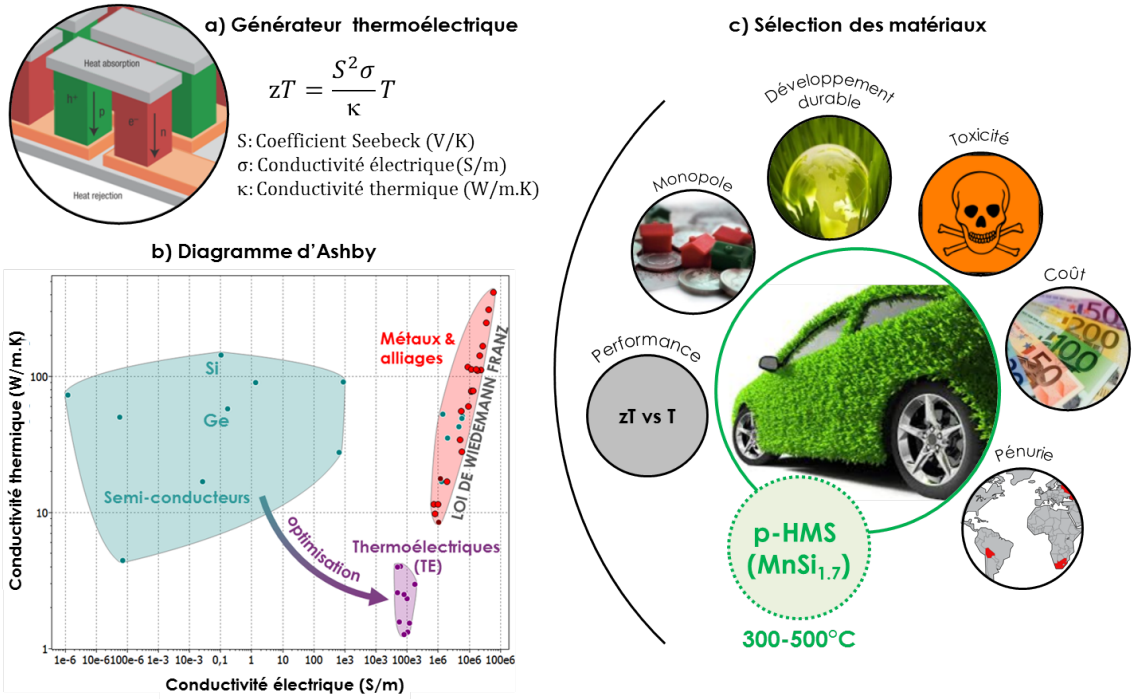

FIGURE 1 – *Schéma d'un module thermoélectrique [1] et de la figure de mérite (zT) (a). Diagramme d'Ashby représentant la conductivité thermique en fonction de la conductivité électrique où l'on constate que les matériaux thermoélectriques remplissent l'espace des propriétés entre les semi-conducteurs classiques et les métaux et alliages (b). Critères pris en compte lors de la sélection des matériaux aboutissant au siliciure de manganèse $MnSi_\gamma$ pour la jonction de type p (c).*

Ces alliages sont des semi-conducteurs dégénérés de type p qui appartiennent à la famille des phases Nowotny Chimney Ladder (NCL) de formule chimique générale M_nX_m (M : métal de transition ; X : élément des groupes 13 ou 14 ; n et m des nombres entiers). Leur structure cristalline dérive de la structure type $TiSi_2$ dans laquelle les atomes M occupent les positions du Ti et forment un sous-système quadratique de type β-Sn (Chimney en anglais, pour cheminée) et les atomes X sont arrangés suivant la direction c et forment une hélice occupant les interstices du sous-système [M] (Ladder en anglais, pour échelle) (voir figure 2.a.). Ces deux sous-systèmes possèdent des périodes différentes suivant la direction c ; la maille élémentaire des phases NCL est donc décrite par la relation suivante :

$$c = nc_M = mc_X$$

où c_M représente le paramètre de maille du sous-système [M] et c_X celui du sous-système [X].

Par conséquent, le ratio atomique X/M des composés $M_nX_m$est relié au ratio c_M/c_X par la relation 1.1 :

$$\frac{X}{M} = \frac{m}{n} = \left(\frac{c_M}{c_X}\right) = \text{ϒ} \tag{1}$$

Pour des raisons de stabilité, les phases NCL respectent la règle des 14 électrons de valence par métal de transition M [3, 4] (voir équation 1.2) :

$$\frac{X}{M} = \frac{14 - e_M}{e_X} \tag{2}$$

avec e_M et e_X le nombre d'électrons de valence pour M et X respectivement.

Pour les composés HMS la phase idéale a pour formule Mn_4Si_7. De nombreux désaccords subsistent dans la littérature quant à l'existence d'un mélange de phases commensurables ou à l'existence d'une seule phase incommensurable [5, 6, 7, 8, 9], **pour lever ces incertitudes nous avons réalisé une étude systématique couplant la diffraction des rayons X et la diffraction des électrons (chapitre 2).**

Au sein de ses alliages, une singularité microstructurale est observée dans les alliages synthétisés par la voie liquide : des fines striations de composition MnSi uniformément distribuées perpendiculairement à l'axe c dans la phase HMS [10, 11] (voir figure 2.b.). La formation et la stabilité de ces striations ne peut être expliquée par le diagramme de phase Mn-Si, **cette étude propose donc d'étudier la microstructure des alliages HMS et la façon dont elle change en fonction du procédé et de la composition (chapitre 2).**

De plus, la mesure des trois propriétés de transport thermoélectriques sur des monocristaux obtenus par voie liquide a montré une forte anisotropie de celles-ci [10, 12, 13, 14, 15, 16, 17, 18] (voir figure 2.c.). De part la présence de la phase MnSi au sein des matériaux synthétisés, nous avons voulu déterminer l'origine de l'anisotropie : intrinsèque à la phase HMS ou due à un effet composite (HMS/MnSi). Grâce à la compréhension des relations entre les phases, la microstructure et le procédé décrites dans le chapitre 2, la production de matériaux HMS purs a pu être réalisée. **Afin de caractériser l'anisotropie, nous avons développé la production de matériaux purs texturés (chapitre 3) afin d'étudier les propriétés intrinsèques de la phase HMS.**

Enfin, les propriétés de transport sont analysées (chapitre 4) afin de révéler des trajectoires dans l'espace des propriétés en vue d'une amélioration du niveau de maturité technologique de ses alliages.

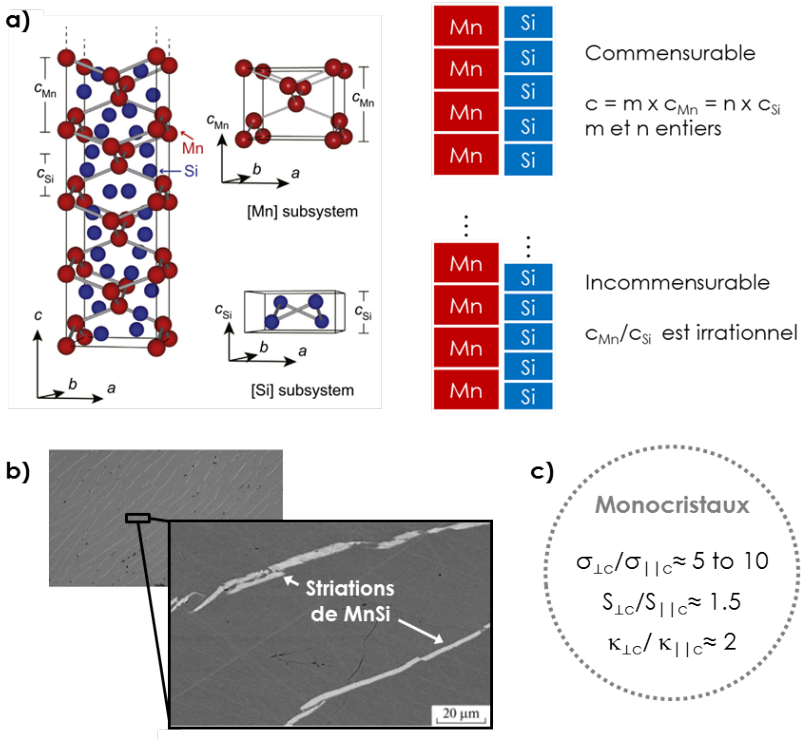

FIGURE 2 – *Présentation des spécificités des alliages HMS : structure cristalline (a), microstructure (b) et anisotropie des propriétés (c).*

Afin de relever les nombreux défis scientifiques de cette thèse, nous avons travaillé au sein du paradigme de la science des matériaux : structure/microstructure/procédé/propriétés où l'on s'est attaché a comprendre les relations entre ces quatre paramètres.

Du procédé au propriétés, les paramètres de la structure et de la microstructure peuvent être utilisés afin d'améliorer les performances thermoélectriques. Ces paramètres sont représentés sur la figure 3 où la zone grise regroupe les paramètres influencés par la chimie et en bleu ceux influencés par la microstructure. Dans notre approche et en raison des spécificités des alliages HMS présentés ci-dessus, nous avons choisi d'agir sur la structure, les striations de MnSi (composite) et les matériaux texturés. Deux autres paramètres seront analysés de façon classique : le dopage et la porosité dans le but d'étudier des matériaux très denses présentant un bon équilibre entre les propriétés électroniques (conductivité électrique et coefficient Seebeck).

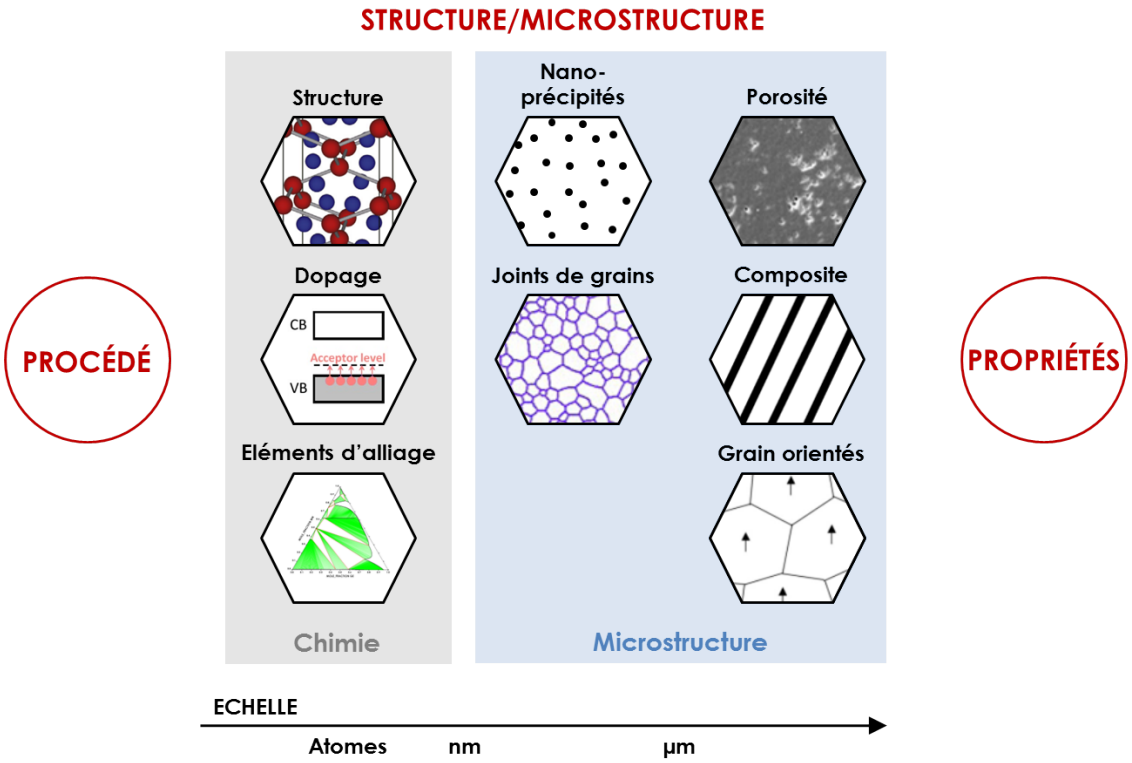

FIGURE 3 – *Lien entre les procédés et les propriétés : les paramètres de la structure et de la microstructure. La zone grise regroupe les paramètres influencés par la chimie et en bleu ceux influencés par la microstructure.*

L'originalité des résultats présentés ci-après réside dans le couplage entre la chimie du solide et la métallurgie en vue de contrôler et d'améliorer ces matériaux pour une utilisation au sein de générateurs thermoélectriques.

- Grâce à une stratégie développée durant cette thèse et basée sur une approche de groupe de super espace (3+1)D, l'interprétation et l'indexation des diagrammes de diffraction des rayons X ainsi que des clichés de diffraction a aboutit à l'identification univoque de la phase HMS.

  Ainsi, nous avons mis en évidence les relations suivantes :

  - la présence des striations de MnSi est reliée à la formation d'un mélange de phases commensurables durant la solidification, alors que l'absence de striations indique la formation d'une seule phase incommensurable.
  - la transition commensurable-incommensurable peut être induite par post-procédé (densification ou traitement thermique) ou par addition d'éléments d'alliage (Ge).

La figure 4 présente deux cartes qui résument les effets du procédé et de la composition sur les spécificités des alliages HMS ie. la présence des striations et le caractère inco/commensurable.

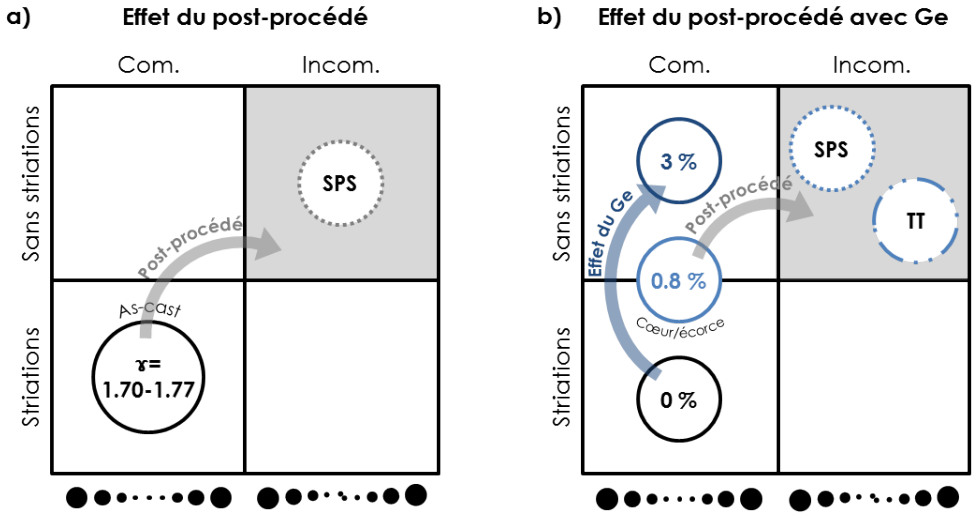

FIGURE 4 – *Carte représentant l'évolution et les liens entre les paramètres structuraux et microstructuraux en fonction du procédé pour un alliage non dopé (a) et pour un alliage dopé avec du Ge (b). Les abréviations com. et incom. désignent le cararactère commensurable et incommensurable de la phase HMS. Les abréviations SPS et TT désignent les post-procédés par Spark Plasma Sintering et par Traitement Thermique.*

- De plus, nous avons démontré par des expériences de couple de diffusion que la voie solide conduit à la formation d'une phase incommensurable. Ce résultat a permis de développer une nouvelle voie de synthèse tout solide assistée par densification (Spark Plasma Sintering). Ainsi le frittage réactif en voie solide entre des poudres de MnSi et de Si aboutit à des matériaux pur, incommensurables et dépourvus de striations, en une seule étape.

- L'utilisation du procédé melt-spinning nous a permis d'obtenir des rubans texturés. La consolidation par SPS de rubans empilés conduit à la formation de matériaux massifs texturés, purs, incommensurables et dépourvus de striations MnSi. La figure 6 présente la texture obtenue à la surface d'un ruban où l'on observe majoritairement des grains de couleur bleu orientés selon la direction <110>. L'analyse des figures de pôles a permis de mettre en évidence une texture de fibre où l'axe c de la structure cristalline possède une rotation libre autour de l'axe de croissance [110] qui est parallèle à la direction normale. Ainsi, lors de la solidification une croissance préférentielle est imposée par le gradient thermique et la structure cristalline ce qui aboutit à l'obtention de rubans texturés.

Grâce au matériaux texturés nous avons montré l'isotropie de la phase HMS. Enfin, lors du dopage au Ge de ces matériaux nous avons mis en évidence une anisotropie forte des propriétés ouvrant de nouvelles perspectives pour améliorer les propriétés thermoélectriques.

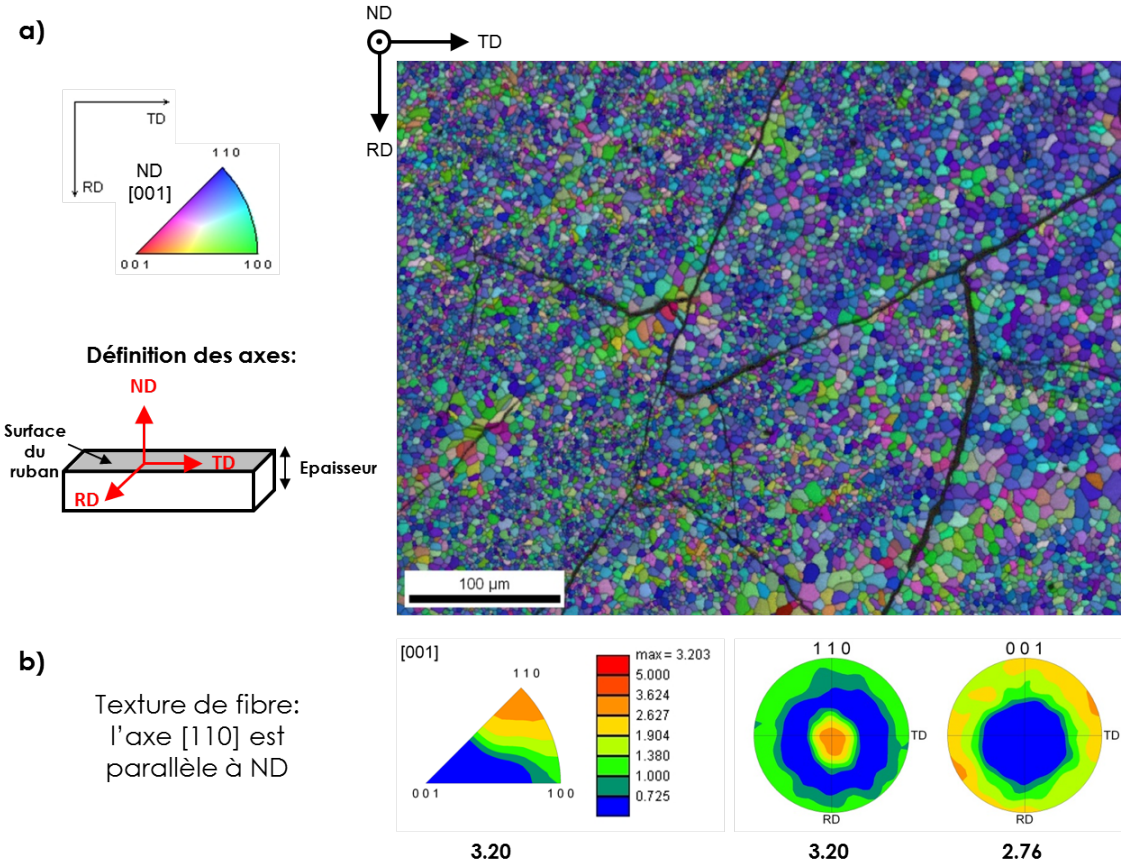

FIGURE 5 – *Description de la texture obtenue après melt-spinning sur la surface d'un ruban. La cartographie EBSD (Electron BackScatter Diffraction) permet de visualiser simultanément les grains ainsi que leur orientation cristallographique grâce au triangle standard (a). La figure inverse de pôle [001]ainsi que les figures de pôles (110) et (001) décrivent le type de texture obtenue sur une échelle colorée normalisée à 5. Ces figures indiquent une texture de fibre avec l'axe [110] parallèle à ND (Normal Direction) (b).*

- Les performances thermoélectriques ont été mesurées pour les deux voies explorées pendant cette thèse. Les résultats obtenus sont illustrés sous forme d'un diagramme d'Ashby (voir figure 6) tracé à 500°C où le facteur de puissance $S^2\sigma$ (numérateur du zT) est représenté en fonction de la conductivité thermique (dénominateur du zT). Au sein de ce diagramme la performance augmente du coin en bas à droite vers le coin en haut à gauche. Les droites représentent des lignes

d'isoperformance : deux matériaux présents sur la même droite auront le même zT. On constate que le frittage réactif est plus performant (zT=0.53) que la voie liquide classique. L'augmentation de 23% du facteur de puissance pour le frittage réactif est obtenue par une augmentation de la conductivité électrique attribuée à une augmentation de la mobilité des porteurs de charge. De plus, le dopage au Ge pour une composition nominale $Mn(Si_{0.992}Ge_{0.008})_{1.73}$ permet d'atteindre un zT de 0.58 pour la voie liquide. Cependant, une optimisation est encore nécessaire afin d'égaler les meilleures performances (zT 0.7) pour le frittage réactif.

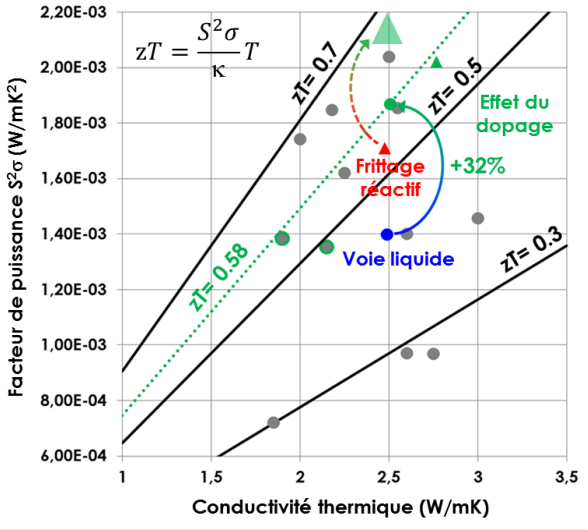

FIGURE 6 – *Diagrammes d'Ashby pour les matériaux thermoélectriques à 500°C. Chaque symbole représente un résultat issu de la littérature (en gris) ou un résultat obtenu durant cette thèse (en couleur). Ce diagramme compare des deux voies de synthèse : voie liquide (rond bleu) et frittage réactif (triangle rouge) ainsi que l'effet du dopage (symboles vert) (b).*

Ce travail a permis de remplir un objectif technologique grâce au développement de procédés de production fiables et reproductibles permettant un contrôle de la composition et de la microstructure. Enfin, les défis scientifiques ont été relevés grâce une étude systématique des relations entre le caractère incommensurable, la microstructure et l'anisotropie dans le but d'optimiser les propriétés électroniques et thermique.

Bibliographie

[1] G.J. Snyder and E.S. Toberer. Complex thermoelectric materials. *Nature Materials*, 7(2) :105–114, 2008.

[2] H. Mun, S.-M. Choi, K.H. Lee, and S.W. Kim. Boundary engineering for the thermoelectric performance of bulk alloys based on bismuth telluride. *Chem. Sus. Chem*, 8(14) :2312–2326, 2015.

[3] D. C. Fredrickson, S. Lee, and R. Hoffmann. The nowotny chimney ladder phases : Whence the 14 electron rule ? *Inorg. Chem.*, 43(20) :6159–6167, 2004.

[4] D. C. Fredrickson, S. Lee, R. Hoffmann, and J. Lin. The nowotny chimney ladder phases : Following the c_{pseudo} clue toward an explanation of the 14 electron rule. *Inorg. Chem.*, 43(20) :6151–6158, 2004.

[5] R. De Ridder and S. Amelinckx. The structure of defect manganese silicides. *Materials Research Bulletin*, 6(11) :1223–1234, November 1971.

[6] H. W. Knott, M. H. Mueller, and L. Heaton. The crystal structure of $mn_{15}si_{26}$. *Acta Crystallographica*, 23(4) :549–555, 1967.

[7] G. Zwilling and H. Nowotny. The crystal structure of the defect manganese silicide, $mn_{27}si_{47}$. *Monatshefte fur Chemie*, 104(3) :668–675, 1973.

[8] H.Q. Ye and S. Amelinckx. High-resolution electron microscopic study of manganese silicides $mnsi_{2-x}$. *Journal of Solid State Chemistry*, 61(1) :8–39, January 1986.

[9] J.M. Higgins, A. L. Schmitt, I. A. Guzei, and S. Jin. Higher manganese silicide nanowires of nowotny chimney ladder phase. *J. Am. Chem. Soc.*, 130(47) :16086–16094, November 2008.

[10] I. Kawasumi, M. Sakata, I. Nishida, and K. Masumoto. Crystal growth of manganese silicide, $mnsi_{1.73}$ and semiconducting properties of $mn_{15}si_{26}$. *Journal of Materials Science*, 16(2) :355–366, 1981.

[11] E.I. Suvorova and V.V. Klechkovskaya. Precipitates of mnsi cubic phase in tetragonal mn_4si_7 crystal. 58(6) :854–861, 2013.

[12] L. M. Levinson. Investigation of the defect manganese silicide mn_nsi_{2n-m}. *Journal of Solid State Chemistry*, 6(1) :126–135, January 1973.

[13] G. Zwilling and H. Nowotny. Anisotropy of the electrical conductivity of $mn_{27}si_{47}$. *Monatshefte fur Chemie*, 105(4) :666–670, 1974.

[14] A.A. Baikov L.D. Ivanova. Higher manganese silicide based materials. *Journal of Thermoelectricity*, 3 :60–66, 2009.

[15] X. Chen, A. Weathers, J. Carrete, S. Mukhopadhyay, O. Delaire, D.A. Stewart, N. Mingo, S.N. Girard, J. Ma, D.L. Abernathy, J. Yan, R. Sheshka, D.P. Sellan, F. Meng, S. Jin, J. Zhou, and L. Shi. Twisting phonons in complex crystals with quasi-one-dimensional substructures. *Nature Communications*, 6 :6723, 2015.

[16] I. Engstrom and B. Lonnberg. Thermal expansion studies of the group iv-vii transition-metal disilicides. *Journal of Applied Physics*, 63(9) :4476–4484, 1988.

[17] H Kaga, Kinemuchi Y., and Watari K. Fabrication of c-axis oriented higher manganese silicide by a high-magnetic-field and its thermoelectric properties. *Journal of Materials Research*, 22 :2917–2923, 2007.

[18] Y. Sadia, Z. Aminov, D. Mogilyansky, and Y. Gelbstein. Texture anisotropy of higher manganese silicide following arc-melting and hot-pressing. *Intermetallics*, 68 :71–77, January 2016.

Contents

List of Figures

List of Tables

Introduction

The present thesis is dedicated to the study of thermoelectric materials: Higher Manganese Silicide (HMS) based alloys that are p-type semiconductors. This work is part of a larger project that aims at developing a thermoelectric generator composed of Silicide based alloys for automotive applications. Although technological progress has moved at a staggering space in the past century, two of the most important sectors in terms of greenhouse gas emissions (transport and electricity) remain largely reliant on a heavily polluting concept dating back to the 19^{th} Century: fossil fueled combustion continues to drive the turbines in power plants and the pistons in cars, trains and buses. Towards improving vehicle fuel economy, functional metallurgy is mandatory to provide a detailed understanding of enhanced thermoelectric materials with considerable potential for large scale production.

The first chapter presents our global approach to improve thermoelectric materials for automotive application. In order to insure the viability of our project, we have applied a materials selection method which uses cost and sustainable requirements as constraints that materials must fulfill. After a careful review of the literature data, an essential aspect that must be controlled for materials implementation was highlighted: the high dispersion of performances due to heterogeneous microstructures. This highlight requires a better understanding of the material science paradigm (processing, structure, microstructure and functional properties). In other words, coupling functional metallurgy and solid-sate chemistry fields is necessary for HMS optimization. The main challenges of this thesis are (1) the establishment of a systematic method to fully characterize the HMS features by applying a multidisciplinary approach, (2) the production of reliable pure HMS with controlled microstructure by an optimization of the process, and (3) the investigation of textured bulk materials with respect to the claimed anisotropy highlighted in the literature.

The second chapter is dedicated to the study of the relationship between structure and microstructure in HMS based alloys. A systematic approach is followed in order to thoroughly characterize the

materials from as-cast state to bulk post-processed state. Two processes are studied: liquid-phase and solid state synthesis and their influence on the HMS highlights is investigated. Thanks to this systematic approach an innovative route to produce pure HMS alloys based on reactive sintering is developed.

The third chapter presents HMS textured bulk materials obtained via the melt-spinning process. The production of textured flakes with a fiber-like texture is evidenced in HMS brittle phase and retained after post-processing by SPS. This part aims at discussing the anisotropy of pure HMS materials produced without MnSi striations.

The fourth chapter aims at defining pathways in the thermoelectric materials properties space in correlation to the processing, the doping and the texture effects. From optimized HMS alloys, trajectories are drawn in the thermoelectric materials properties space, a necessary step to scale-up their production.

Finally, this manuscript ends with a conclusion of the work initiated during these three years and proposes some perspectives that could be developed in the future to bring HMS alloys closer to large-scale waste heat harvesting applications.

Chapter 1

Motivations and objectives

This first chapter presents the positioning, challenges and objectives of this thesis which focuses on the study of Higher Manganese Silicide (HMS) for thermoelectricity. Instead of enumerating a long list of earlier studies, we have compiled the background, our bibliographic analysis, and the conclusions that we drawn using four visual-thinking boards. Each of the sections is connected to a board.

The first one presents the topic and core concept addressed by this work which is concerned by energy and environmental issues.

The second board exposes the materials choice to achieve a sustainable development of the thermoelectric technology for cars' waste heat recovery systems.

The third board describes the basics related to HMS and the progress we want to make beyond the state-of-the-art.

The last board outlines the frame of this project and the approach.

1.1 Rationale

The worldwide growing demand for energy fed by the continuous development of humankind and the consequent impact on both carbon emission and natural resource consumption are becoming a major treat in terms of socio-economical, geo-political and environmental impacts. Innovative solutions are required in energy production, transport, industry, information and communication technologies, in order to decrease our high reliance on fossil fuels. However, the journey to renewable energy based-systems is very challenging, it is why attempts to improve the efficient use of fossil fuel are necessary steps in reducing global consumption and carbon emission.

Transports account for about 20% of all carbon released into the atmosphere [1], thus car passengers are a very good example of this incremental approach (see figure 1.1.a.). To reduce this source of emissions, several nations have target electrical vehicles sales up to around 10% of all cars sales by 2020.

However, a recent sustainable assessment of this measure [2] shows that achieving this development on the scale and time envisaged is a tough challenge due to the high demand created for critical elements (mainly Nd and Li) and the moderate contribution to the reduction of carbon emissions unless the national grid is decarbonized (such as in France, thanks to nuclear power plants) (see figure 1.1.b.). If we want to achieve the passenger car emission objectives (from 130 g/km nowadays to 95 g/km by 2020), alternative solutions should be considered. Of course, cheating software cannot be considered as a reasonable one, so we are left with at least two different strategies: structure light-weighting and energy efficiency increase.

This thesis is concerned by the second strategy. Internal combustion engines are responsible for a high amount of heat losses ($> 50\%$ of the total primary fuel energy). Harvesting this waste heat may represent a very interesting opportunity to significantly reduce global carbon footprint of road transportation (see figure 1.1.c.).

Thermoelectricity (TE) is a promising technology for waste heat recovery system due to its ability to directly convert a heat flow into electricity. TE generators (TEGs) are compact solid-state devices with no moving parts [3]. They are silent, reliable and scalable, making them ideal for distributed power generation and in applications where low maintenance need is crucial (see figure 1.1.d.).

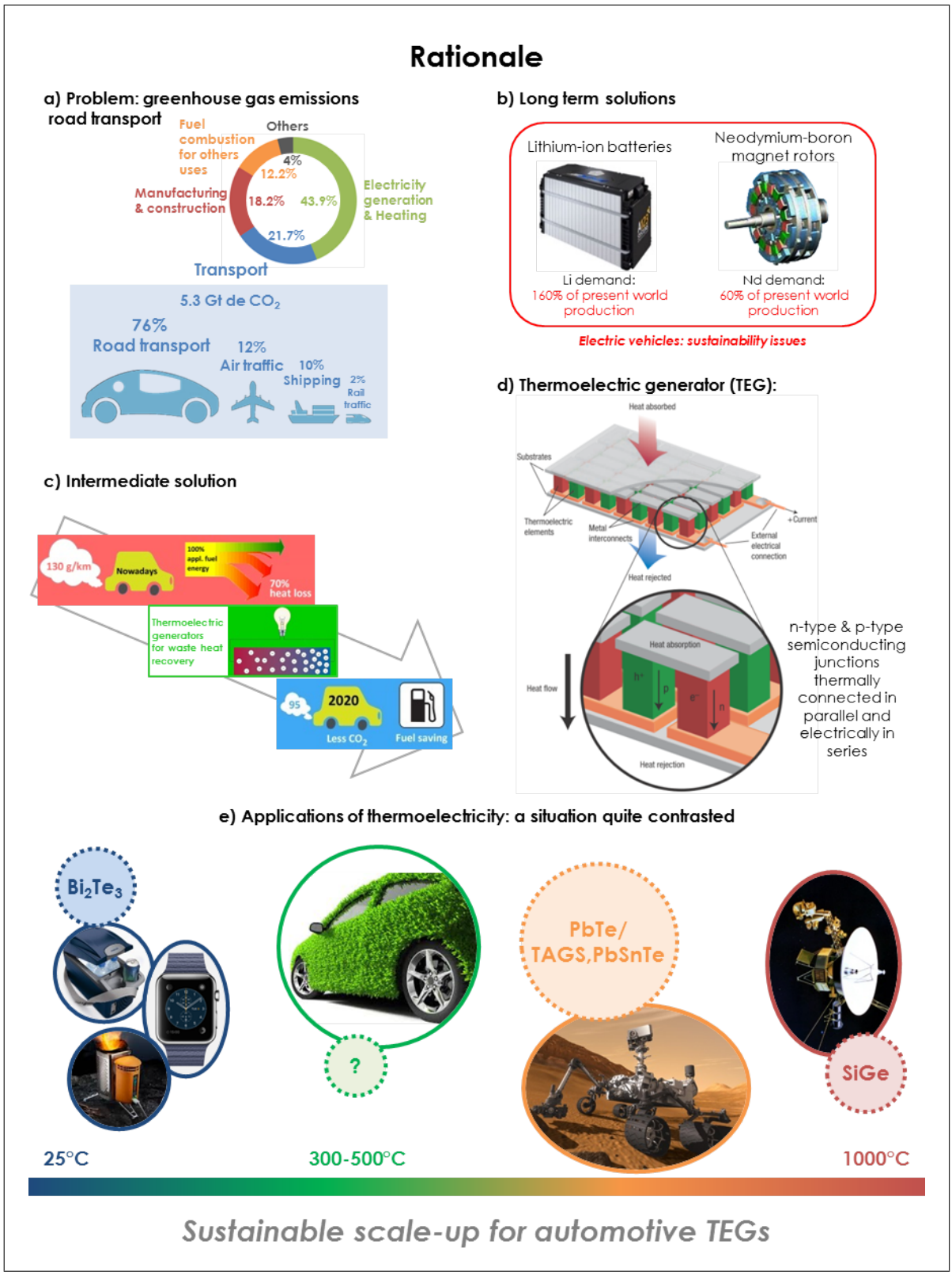

Figure 1.1: *Rationale.*

However, TEGs have not yet found their way into mass production - they have only been sold for low volume and specific applications where reliability (aerospace) or energy access (remote power generation, camping products) are mandatory - despite the successful and plethoric development of efficient bulk TE materials (see figure 1.1.e.). This is because the research and development of TE materials have been only driven by the enhancement of the conversion efficiency whereas the main barrier arises from the inability to achieve sustainable scale-up of this technology for reasons exposed hereafter.

This thesis is committed to contribute to the sustainable scale-up of the TE technology.

1.2 Materials selection

Many limitations on the performances, cost and scalability of TE energy conversion systems are due to the materials' intrinsic properties. The conversion efficiency of TEGs depends on the ability of the materials used to form the junctions (1) to maintain the thermal gradient between the hot source and the cold sink, (2) to generate a voltage due to the Seebeck effect, and (3) to conduct an electrical current. These material requirements are translated into a performance index, called the figure of merit (zT), which measures how well the materials can perform the job (see figure 1.2.a.).

This antagonist combination of properties controlling the performance of thermoelectrics makes difficult to design these materials. Notwithstanding, semiconductors provide the best compromise, and early work on thermoelectricity put more emphasis on them (see figure 1.2.b.) [4]. Over the past 40 years, alloys based on Bi_2Te_3, PbTe, skutterudites, clathrates and (Si,Ge) have been extensively studied and optimized for their use as TE materials to perform very successfully in a variety of solid-state power-generation applications [3, 5, 6, 7]. Unfortunately, none of the above materials would allow a sustainable scale-up of the TE technology because their constituting elements are either toxic, scarce, critical, and/or expensive. In addition to the design requirements (see figure 1.2.c.), car makers and their suppliers are concerned by risks from supply-chain disruption, price fluctuation and legislation. These are very challenging targets for materials R&D, and materials choice must fulfill these constraints if we want to achieve sustainable scale-up of TEGs.

Inspired by the case study on electrical cars provided by M. Ashby in his last book [2], we have examined the supply chain and availability of TE materials in order to make realistic choices of materials. If we consider only 10% of existing passenger car global production to implement TEGs (in order to turn waste heat from the exhaust into a free electrical power source, see figure 1.2.d.), it represents 8 million of vehicles per year [2]. The annual production of 8 million of cars, each containing about 1 kg of TE materials (this is the amount roughly needed to produce enough power), would requires roughly 8000 tonnes of TE materials per year. The Herfindahl-Hirschman Index (HHI) is a measure of risk when the supply of a material is controlled by one or very few nations. An HHI above 0.2 indicates severe supply-chain concentration. Charts in figure 1.2.e. show that most of the state-of-the-art TE materials are inadequate to achieve a sustainable development on a global scale because their supply chain is at present inadequate (annual production too low and/or controlled by only few nations).

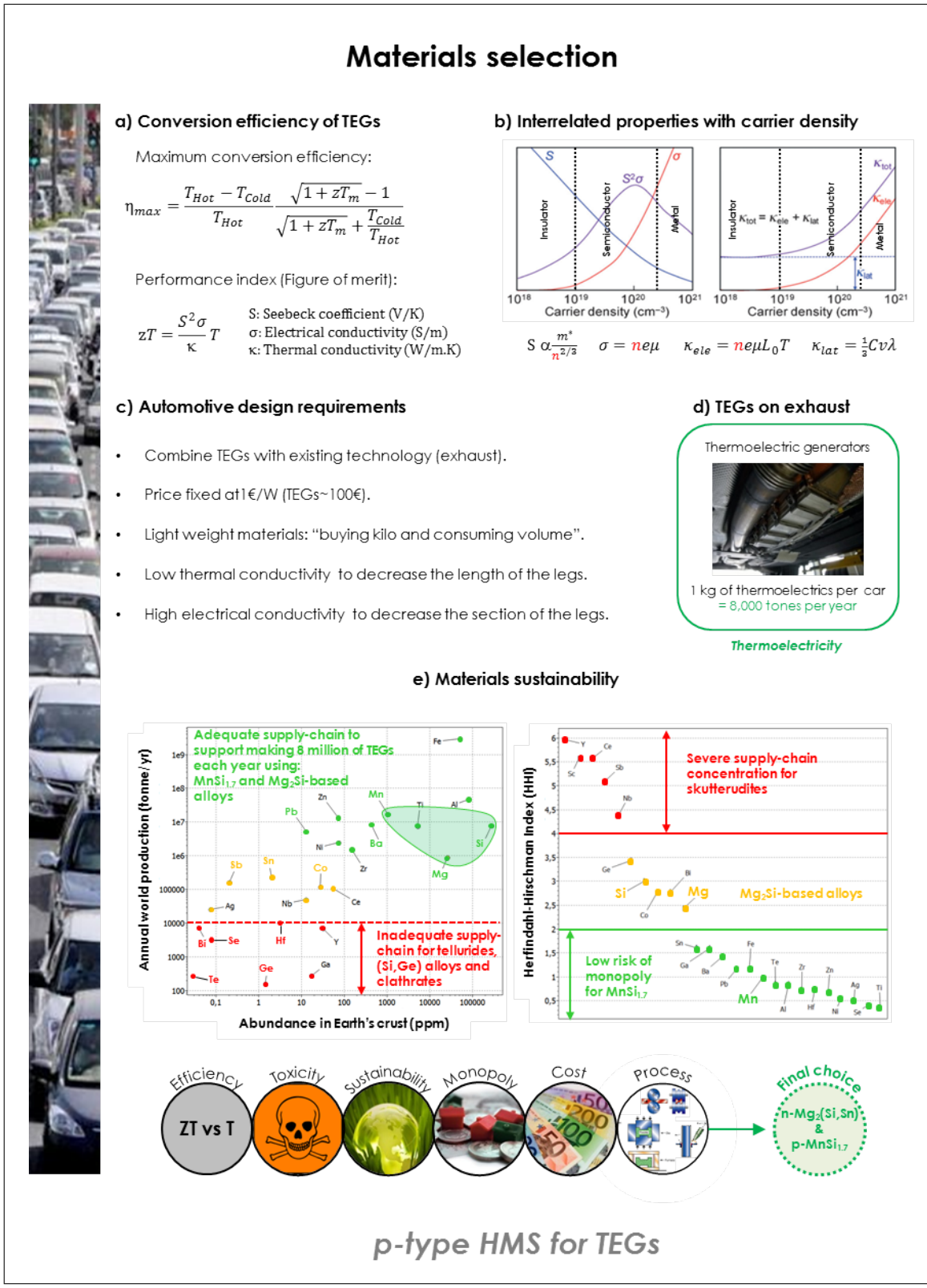

Figure 1.2: *Materials selection.*

We are left with the final choice – manganese and magnesium silicides – for the following reasons: (1) they demonstrate TE performance in the temperature range 300-500°C, (2) they are stable even in severe environmental conditions and require no increase in manufacturing complexity, key properties lacking in current state-of-the-art competitors, (3) they are not made of toxic elements, such as unacceptable heavy metals that damage bio-systems, and (4) they are made of non-monopolistic, non-critical and abundant constitutive elements.

This thesis focuses on the study of Higher Manganese Silicide, HMS.

1.3 HMS highlights and thesis' objectives

Figure 1.3 summarizes the background and issues related to the study of HMS, and outlines the major objectives we propose to achieve in the present work.

HMS is a p-type degenerated semiconductor. It belongs to the group referred as Nowotny Chimney Ladder (NCL) phases with the general chemical formula M_nX_m (M, transition metal element; X, group 13 or 14 elements; n and m, integers) encountered in a variety of intermetallic compounds such as $VGe_{1.82}$, $MoGe_{1.77}$ and $RuSn_{1.5}$ [8, 9]. The crystal structure of the NCL phases derives from $TiSi_2$-type structure in which the atoms of M occupy the Ti positions and form a β-Sn tetragonal sub-system (chimney), while the atoms X are re-arranged in the c-direction and form a helical arrangement (ladders) occupying the interstice of the [M] sub-system (see figure 1.3.a.). Whereas both sub-systems are unchanged along the other two main crystallographic directions, their periods differ in the c direction. Consequently, the unit cell of NCL phase has a c-dimension which is equal to a certain multiple of the [M] sub-system parameter c_M and the [X] sub-system parameter c_X leading to a large lattice parameter in this direction:

$$c = nc_M = mc_X$$

Consequently, the X/M atomic ratio of the NCL compound M_nX_m is related with the c_M/c_X ratio as follows 1.1:

$$\frac{X}{M} = \frac{m}{n} = \left(\frac{c_M}{c_X}\right) = \curlyvee \tag{1.1}$$

For stability reason, the NCL phases follow the 14 Valence Electron Count (VEC) rule per M atoms [10, 11] (see equation 1.2). The stability of a phase seems to be intimately related to the total number of valence electrons per transition metal atoms. For transition metal groups 7, 8, and 9, there is a preponderance of structures with 14 valence electrons per transition metal. So, the X/M ratio of a particular binary NCL phase is controlled by the number of valence electrons of the M atoms:

$$\frac{X}{M} = \frac{14 - e_M}{e_X} \tag{1.2}$$

with e_M and e_X the numbers of valence electrons for M and X respectively.

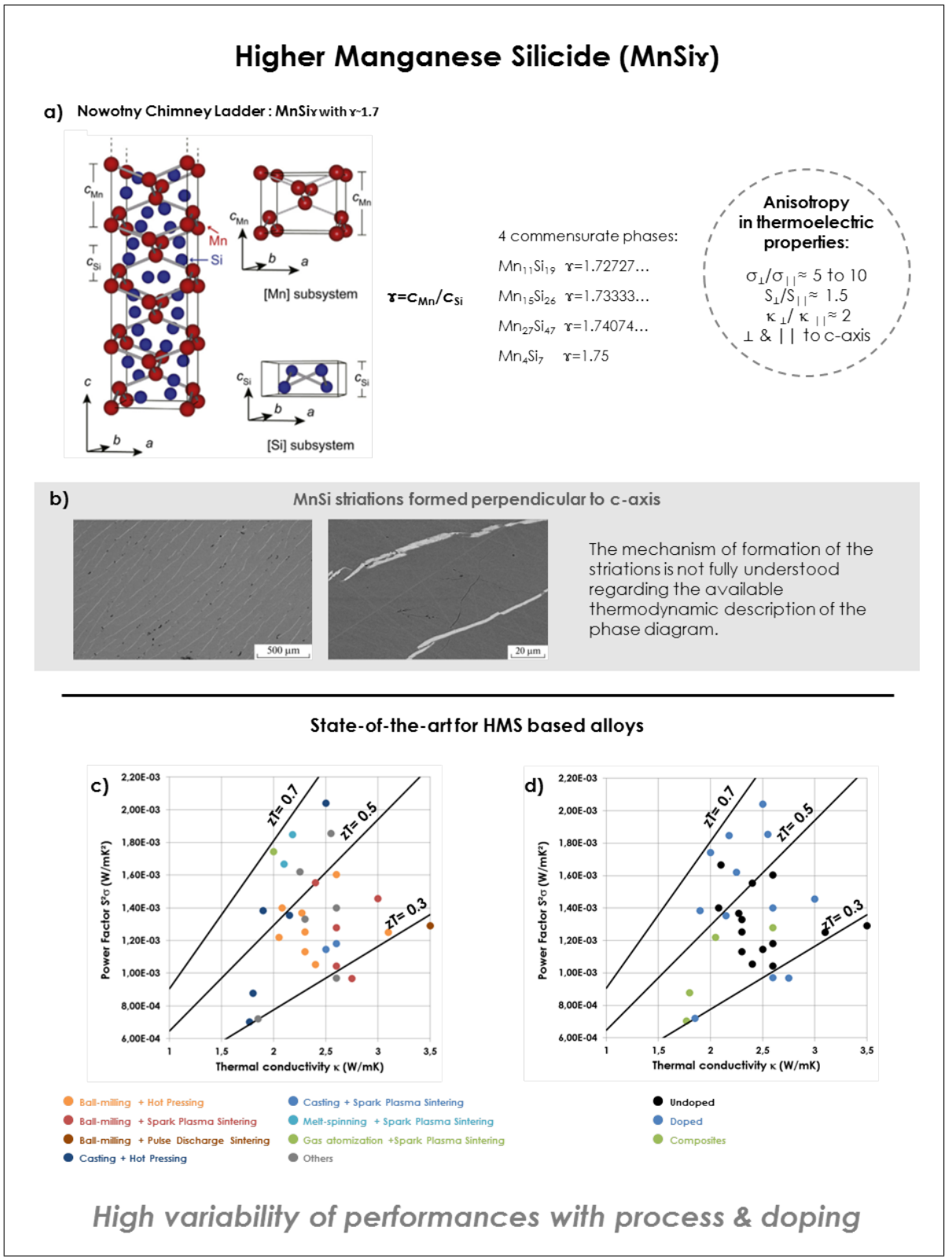

Figure 1.3: *Higher Manganese Silicide.*

For HMS the ideal VEC=14 value gives the chemical formula Mn_4Si_7. This is about the unambiguous statements we can make for HMS. If we dig deeper things become much more confused. Indeed, up to 8 distinct HMS phase have been reported - Mn_4Si_7, $Mn_{11}Si_{19}$, $Mn_{15}Si_{26}$, $Mn_{27}Si_{47}$, Mn_7Si_{12}, $Mn_{19}Si_{33}$, $Mn_{26}Si_{45}$ and $Mn_{39}Si_{68}$ [12, 13, 14, 15, 16] - and a number of authors assumed either the existence of a mixture of different commensurate HMS phases or a single incommensurate phase.

Since the sixties and until now, each contribution of the literature to the debate results to a dissonant cacophony of opinions across an increasing spectrum of interpretations. Instead of stacking a new one, **this work is an attempt at clarifying this issue around the HMS phase identification (chapter 2).** This is to be accomplished through a critical review of the claims and concepts arising from the literature, a better control of the fabrication process of HMS and the application of an approach to interpret the X-ray and electron diffraction patterns in a coherent and unified manner.

Aside to these specific features of the crystal structure of HMS, investigations of the microstructure of melted HMS reveal another special characteristic which is the presence of thin MnSi platelets uniformly distributed perpendicular to the c-axis of HMS [17, 18] (see figure 1.3.b.). Even if these MnSi striations seem to be always observed (in melt-grown single crystal [17, 18, 19, 20], as well as induction melted ingots [21, 22]) with a proportion of about 2 wt.% [19], and are almost impossible to suppress in bulk HMS [19, 23], their formation is not unambiguously explained and the Mn-Si phase diagram [24] appears useless to this respect.

One of the scientific objective of this thesis is to study the microstructure of HMS materials and the way it changes with the processes and the composition (chapter 2). Based on this understanding we should be able to produce highly pure HMS samples to test their intrinsic transport properties (chapter 4).

To discuss the transport properties of HMS, we have plotted the power factor (the numerator of zT) against the thermal conductivity (the denominator of zT) for all the HMS alloys from the literature (see figure 1.3.c.). In this materials properties space (so-called Ashby diagram) for thermoelectrics the different HMS materials of the state-of-the-art are represented by bubbles, and the TE performance by lines of slopes equal to zT. Materials above the line have higher values of zT than those below it, while materials lying on the same line perform equally well.

Charts shown on figure 1.3.c. show that the properties of HMS materials span over a large range of values: from 1.7 to 3.5 W/m.K for the thermal conductivity, from 7.10^{-4} to 2.10^{-3} W/m.K^2 for the power factor and from 0.27 to 0.67 for the figure of merit. These important discrepancies result

from the fact that HMS materials were prepared by a large variety of techniques that rely on the consolidation of powders obtained by ball-milling [25, 26, 27, 28, 29, 30, 31, 32, 33, 34], arc-melting [22, 35, 36, 37, 38, 39], melt-spinning [40, 41], gas atomization [42], ...

However, no pattern appears in the thermoelectric properties charts for HMS that could reveal trends, process trajectories or ways processing route and composition influence the transport properties, and from which we could have outlined design guidances to tune the performance of HMS. A careful examination of the literature shows that most of the published thermoelectric properties of HMS were obtained on samples having impurities: MnSi striations in melt grown HMS, Si and MnSi secondary phases in solidified ingots, and porosities in compacts. In fact, to our best knowledge, the intrinsic properties of HMS have never been truly investigated, and we reach the same conclusion for the anisotropy of the properties reported in several papers [17, 19, 43, 44, 45, 46, 47, 48] as well as the doping/alloying effect.

Another scientific objective of this work is to carry out an analysis of the effect of processes (chapter 4), Ge micro-substitutions (chapter 2) and crystallographic texture on the transport properties (chapters 3 & 4).

1.4 Project concept

The core concept of this project thesis revolves around developing scalable, sustainable and reliable p-type thermoelectric materials with a good control of their microstructures and resulting properties. To achieve efficient thermoelectric devices, it is important to understand how manufacturing processes enable to manipulate the properties of the selected thermoelectric material, i.e. HMS. This is why emphasis is put on the microstructure and transport properties of HMS. An important endeavor is also made to resolve several important questions raised by the state-of-the-art regarding (1) the existence of different commensurate phases or a single incommensurate HMS structure and (2) the intrinsic anisotropy of the transport properties of HMS.

This work rely on a consortium (ANR project) involving two upstream academic partners (ICMCB and the Institute Charles Gerhardt of Montpellier, ICGM), a technology integration center (Laboratory for Innovative in New Energy Technologies and Nanomaterials, CEA-LITEN, in Grenoble), and a start-up whose mission is to bring thermoelectric-enabled competitive energy recovery systems to the market (Hotblock OnBoard) (see figure 1.4.a.).

With respect to the design strategies of HMS alloys, this work rely on Density Functional Theory (DFT) ab-initio calculations (from CEA-LITEN) used to derivate the phonon dispersion, velocity and lifetime, and from which it is possible to estimate the contributions of phonons with different mean free path to the cumulative thermal conductivity of HMS. These simulations suggest that microstructural parameters such as the grain size and the precipitates distribution cannot affect significantly the properties of HMS because their size scale is larger than the mean free path of the most contributive phonons (less than 10 nm) [45].

From these insights, **we have decided not to play with the nanostructuration as it is commonly done when it comes to tune the properties of thermoelectrics, but instead look at the structure, alloying (Ge and Cr doping) and anisotropy** (see figure 1.4.b.).

The interpretation of the microstructures of HMS alloys is based on computational thermodynamic thanks to the thermodynamic assessment of the quaternary Cr-Ge-Mn-Si system provided by ICGM [49, 24, 50, 51]. With respect to measuring thermoelectric transport properties, we have access to a wide range of special techniques for material characterization and take full advantage of round-robin testing campaigns to demonstrate the reproducibility of the transport properties of our TE materials.

Finally, **this thesis illustrates that metallurgical approaches and solid state chemistry concepts can be coupled together to study functional materials** (see figure 1.4.c.).

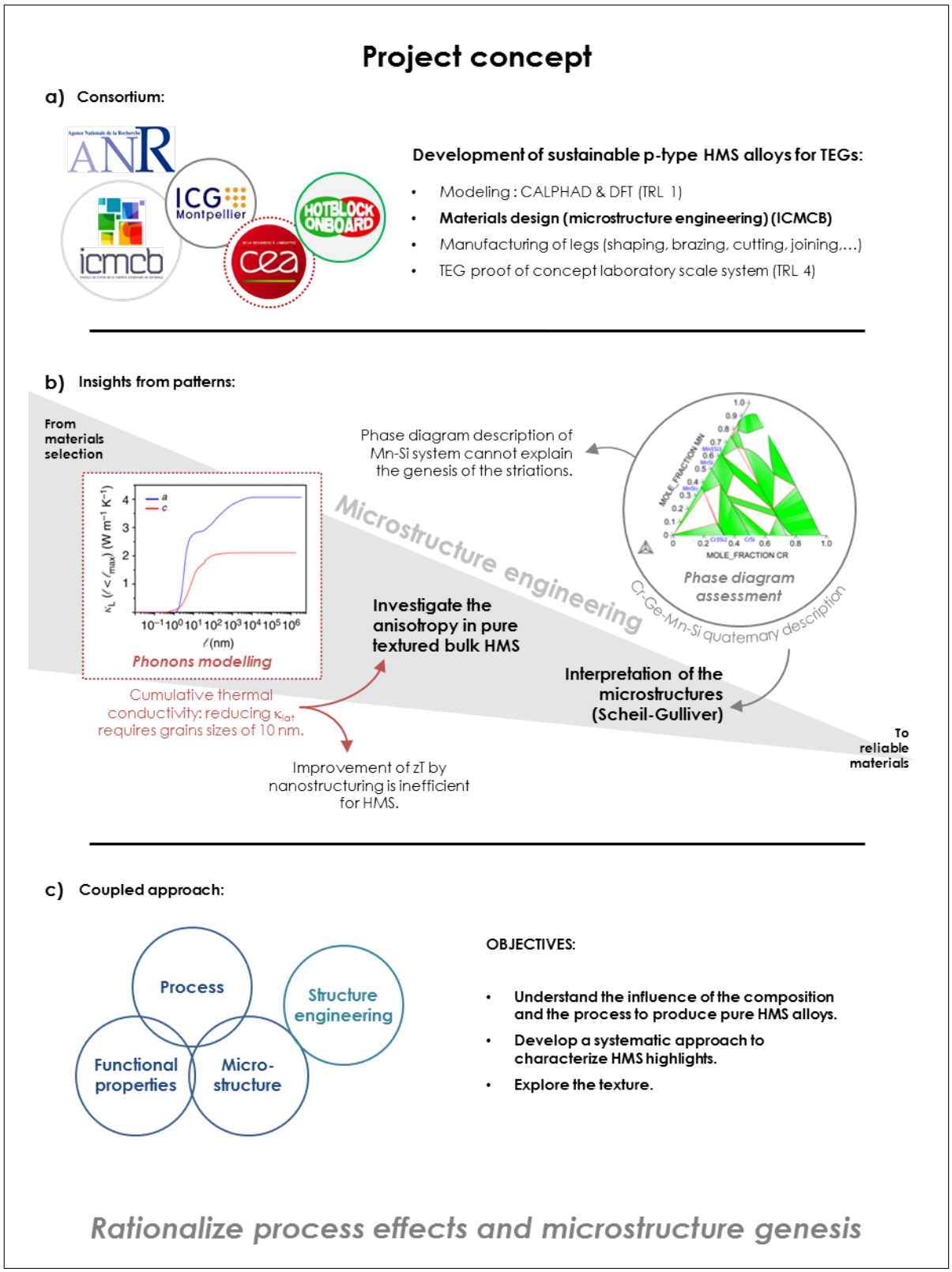

Figure 1.4: *Project concept.*

Bibliography

[1] Siemens. Iea wolrd energy outlook, vattenfall. 2012.

[2] M. Ashby. *Materials and Sustainable Development, 1st Edition*. Butterworth-Heinemann, 2015.

[3] G.J. Snyder and E.S. Toberer. Complex thermoelectric materials. *Nature Materials*, 7(2):105–114, 2008.

[4] H. Mun, S.-M. Choi, K.H. Lee, and S.W. Kim. Boundary engineering for the thermoelectric performance of bulk alloys based on bismuth telluride. *Chem. Sus. Chem*, 8(14):2312–2326, 2015.

[5] N.A. Heinz, T. Ikeda, Y. Pei, and G.J. Snyder. Applying quantitative microstructure control in advanced functional composites. *Advanced Functional Materials*, 24(15):2135–2153, 2014.

[6] Terry M. Tritt. Thermoelectric phenomena, materials, and applications. *Annu. Rev. Mater. Res.*, 41(1):433–448, July 2011.

[7] Terry M. Tritt and M. A. Subramanian. Thermoelectric materials, phenomena, and applications: A bird's eye view. *MRS Bulletin*, 31(03):188–198, 2006.

[8] H. Lind and M. Bostrom. Re-determining the nowotny chimney-ladder structure vge1.82 from powder diffraction data. *Powder Diffraction*, 20(3):198–202, 2005.

[9] G. Zwilling and H. Nowotny. Modifying of $mnsi_{2n-m}$ phases. *Monatshefte fur Chemie*, 107(5):1077–1080, 1976.

[10] D. C. Fredrickson, S. Lee, and R. Hoffmann. The nowotny chimney ladder phases: Whence the 14 electron rule? *Inorg. Chem.*, 43(20):6159–6167, 2004.

[11] D. C. Fredrickson, S. Lee, R. Hoffmann, and J. Lin. The nowotny chimney ladder phases: Following the c_{pseudo} clue toward an explanation of the 14 electron rule. *Inorg. Chem.*, 43(20):6151–6158, 2004.

[12] R. De Ridder and S. Amelinckx. The structure of defect manganese silicides. *Materials Research Bulletin*, 6(11):1223–1234, November 1971.

[13] H. W. Knott, M. H. Mueller, and L. Heaton. The crystal structure of $mn_{15}si_{26}$. *Acta Crystallographica*, 23(4):549–555, 1967.

[14] G. Zwilling and H. Nowotny. The crystal structure of the defect manganese silicide, $mn_{27}si_{47}$. *Monatshefte fur Chemie*, 104(3):668–675, 1973.

[15] H.Q. Ye and S. Amelinckx. High-resolution electron microscopic study of manganese silicides $mnsi_{2-x}$. *Journal of Solid State Chemistry*, 61(1):8–39, January 1986.

[16] J.M. Higgins, A. L. Schmitt, I. A. Guzei, and S. Jin. Higher manganese silicide nanowires of nowotny chimney ladder phase. *J. Am. Chem. Soc.*, 130(47):16086–16094, November 2008.

[17] I. Kawasumi, M. Sakata, I. Nishida, and K. Masumoto. Crystal growth of manganese silicide, $mnsi_{1.73}$ and semiconducting properties of $mn_{15}si_{26}$. *Journal of Materials Science*, 16(2):355–366, 1981.

[18] E.I. Suvorova and V.V. Klechkovskaya. Precipitates of mnsi cubic phase in tetragonal mn_4si_7 crystal. 58(6):854–861, 2013.

[19] L. M. Levinson. Investigation of the defect manganese silicide mn_nsi_{2n-m}. *Journal of Solid State Chemistry*, 6(1):126–135, January 1973.

[20] I. Aoyama, M. I. Fedorov, V. K. Zaitsev, F. Y. Solomkin, I. S. Eremin, A. Y. Samunin, M. Mukoujima, S. Sano, and T. Tsuji. Effects of ge doping on micromorphology of mnsi in mnsi 1.7 and on their thermoelectric transport properties. *Japanese Journal of Applied Physics*, 44(12R):8562, 2005.

[21] A.J. Zhou, H.G. Cui, J.Z. Li, and X.B. Zhao. Structure and morphology of induction-melted higher manganese silicide. *Acta Phys.Chim. Sin.*, 27(12):2915–2919, 2011.

[22] A.J. Zhou, T.J. Zhu, X.B. Zhao, S.H. Yang, T. Dasgupta, C. Stiewe, R. Hassdorf, and E. Mueller. Improved thermoelectric performance of higher manganese silicides with ge additions. *Journal of Electronic Materials*, 39(9):2002–2007, 2010.

[23] I. Nishida, K. Masumoto, I. Kawasumi, and M. Sakata. Striations and crystal structure of the matrix in the mnsi-si alloy system. *Journal of the Less Common Metals*, 71(2):293–301, June 1980.

[24] A. Berche, E. Ruiz-Theron, J.-C. Tedenac, R.-M. Ayral, F. Rouessac, and P. Jund. Thermodynamic description of the mn-si system: An experimental and theoretical work. *Journal of Alloys and Compounds*, 615:693–702, December 2014.

[25] G. Liu, Q. Lu, X. Zhang, J. Zhang, and Y. Shi. InÂ situ synthesis and thermoelectric properties of cr-doped higher manganese silicides. *Journal of Electronic Materials*, 41(6):1450–1455, 2012.

[26] A. Famengo, S. Battiston, M. Saleemi, S. Boldrini, S. Fiameni, F. Agresti, M.S. Toprak, S. Barison, and M. Fabrizio. Phase content influence on thermoelectric properties of manganese silicide-based materials for middle-high temperatures. 42(7):2020–2024–, 2013.

[27] M. Saleemi, A. Famengo, S. Fiameni, S. Boldrini, S. Battiston, M. Johnsson, M. Muhammed, and M.S. Toprak. Thermoelectric performance of higher manganese silicide nanocomposites. *Journal of Alloys and Compounds*, 619(0):31–37, January 2015.

[28] Z. Zamanipour, X. Shi, M. Mozafari, J. S. Krasinski, L. Tayebi, and D. Vashaee. Synthesis, characterization, and thermoelectric properties of nanostructured bulk p-type $mnsi_{1.73}$, $mnsi_{1.75}$, and $mnsi_{1.77}$. *Ceramics International*, 39(3):2353–2358, April 2013.

[29] D.-K. Shin, K.-W. Jang, S.-C. Ur, and I.-H. Kim. Thermoelectric properties of higher manganese silicides prepared by mechanical alloying and hot pressing. *Journal of Electronic Materials*, 42(7):1756–1761, 2013.

[30] X. Shi, Z. Zamanipour, K.F. Ede, J.S. Krasinski, and D. Vashaee. Enhancement of thermoelectric efficiency of $mnsi_{1.75}$ with the addition of externally processed nanostructured mnsi. In *Green Technologies Conference, 2012 IEEE*, pages 1–3, 2012.

[31] T. Itoh and M. Yamada. Synthesis of thermoelectric manganese silicide by mechanical alloying and pulse discharge sintering. *Journal of Electronic Materials*, 38(7):925–929, 2009.

[32] X. Shi, Z. Zamanipour, A.M. Dehkordi, K.F. Ede, J.S. Krasinski, and D. Vashaee. Cost effective synthesis of bulk thermoelectric higher manganese silicide for waste heat recovery and environmental protection. In *Green Technologies Conference, 2012 IEEE*, pages 1–3, 2012.

[33] D. Y. N. Truong, H. Kleinke, and F. Gascoin. Thermoelectric properties of higher manganese silicide/multi-walled carbon nanotube composites. *Dalton Trans.*, 43(40):15092–15097, 2014.

[34] D.Y.N. Truong, H. Kleinke, and F. Gascoin. Preparation of pure higher manganese silicides through wet ball milling and reactive sintering with enhanced thermoelectric properties. *Intermetallics*, 66:127–132, 2015.

[35] A.J. Zhou, X.B. Zhao, T.J. Zhu, S.H. Yang, T. Dasgupta, C. Stiewe, R. Hassdorf, and E. Mueller. Microstructure and thermoelectric properties of sige-added higher manganese silicides. *Materials Chemistry and Physics*, 124:1001–1005, 2010.

[36] V. Ponnambalam, Donald T. Morelli, S. Bhattacharya, and Terry M. Tritt. The role of simultaneous substitution of cr and ru on the thermoelectric properties of defect manganese silicides mnsiδ ($1.73<\delta<1.75$). *Journal of Alloys and Compounds*, 580:598–603, December 2013.

[37] T-H An, S-M Choi, W-S Seo, C Park, I-H Kim, and S-U Kim. Effects of spark plasma sintering temperature on thermoelectric properties of higher manganese silicide. *Journal of Electronic Materials*, 42(7):2269–2273, 2013.

[38] T.-H. An, S.-M. Choi, W.-S. Seo, C. Park, I.-H. Kim, and S.-U. Kim. The effect of microstructure on the thermoelectric properties of polycrystalline higher manganese silicides. *Japanese Journal of Applied Physics*, 52(10S):10MC11, 2013.

[39] A.J. Zhou, X.B. Zhao, T.J. Zhu, Y.Q. Cao, C. Stiewe, R. Hassdorf, and E. Mueller. Composites of higher manganese silicides and nanostructured secondary phases and their thermoelectric properties. *Journal of Electronic Materials*, 38(7):1072–1077, 2009.

[40] W. Luo, H. Li, Y. Yan, Z. Lin, X. Tang, Q. Zhang, and C. Uher. Rapid synthesis of high thermoelectric performance higher manganese silicide with in-situ formed nano-phase of mnsi. *Intermetallics*, 19(3):404–408, March 2011.

[41] W. Luo, H. Li, F. Fu, W. Hao, and X. Tang. Improved thermoelectric properties of al-doped higher manganese silicide prepared by a rapid solidification method. *Journal of Electronic Materials*, 40(5):1233–1237, 2011.

[42] G. Bernard-Granger, M. Soulier, H. Ihou-Mouko, C. Navone, M. Boidot, J. Leforestier, and J. Simon. Microstructure investigations and thermoelectrical properties of a p-type polycrystalline higher manganese silicide material sintered from a gas-phase atomized powder. *Journal of Alloys and Compounds*, 618:403–412, 2014.

[43] G. Zwilling and H. Nowotny. Anisotropy of the electrical conductivity of $mn_{27}si_{47}$. *Monatshefte fur Chemie*, 105(4):666–670, 1974.

[44] A.A. Baikov L.D. Ivanova. Higher manganese silicide based materials. *Journal of Thermoelectricity*, 3:60–66, 2009.

[45] X. Chen, A. Weathers, J. Carrete, S. Mukhopadhyay, O. Delaire, D.A. Stewart, N. Mingo, S.N. Girard, J. Ma, D.L. Abernathy, J. Yan, R. Sheshka, D.P. Sellan, F. Meng, S. Jin, J. Zhou, and L. Shi. Twisting phonons in complex crystals with quasi-one-dimensional substructures. *Nature Communications*, 6:6723, 2015.

[46] I. Engstrom and B. Lonnberg. Thermal expansion studies of the group iv-vii transition-metal disilicides. *Journal of Applied Physics*, 63(9):4476–4484, 1988.

[47] H Kaga, Kinemuchi Y., and Watari K. Fabrication of c-axis oriented higher manganese silicide by a high-magnetic-field and its thermoelectric properties. *Journal of Materials Research*, 22:2917–2923, 2007.

[48] Y. Sadia, Z. Aminov, D. Mogilyansky, and Y. Gelbstein. Texture anisotropy of higher manganese silicide following arc-melting and hot-pressing. *Intermetallics*, 68:71–77, January 2016.

[49] A. Berche, J.C. Tedenac, and P. Jund. Thermodynamic modeling of the germanium-manganese system. *Intermetallics*, 47:23–30, April 2014.

[50] A. Berche, E. Theron-Ruiz, J.-C. Tedenac, and P. Jund. Thermodynamic study of the ge-mn-si system. *Journal of Alloys and Compounds*, 632:10–16, 2015.

[51] A. Berche, J.C. Tedenac, and P. Jund. Ab-initio calculations and calphad description of cr-ge-mn and cr-ge-si. *Calphad*, 49:50–57, June 2015.

Chapter 2

Microstructure control of HMS

In the previous chapter we have highlighted the specific features of the crystal structure of HMS and the large discrepancies regarding the possible existence of different commensurate phases or a single one dimensionally incommensurate structure. This situation is due to the confusions that arise from the number of various approaches applied to perform the difficult task of identification of HMS phases. One of the objectives of this chapter is to contribute to the resolution of this long lasting debate. The production of pure HMS alloys is another challenge due to the inevitable formation of secondary phases during the solidification of this incongruent compound. Another intriguing and detrimental highlight associated to solidified HMS microstructure is the systematic appearance of thin MnSi platelet precipitates (striations) periodically distributed in the HMS grains, and for which the formation cannot be explained by the Mn-Si phase diagram. This is an important issue towards the characterization of the intrinsic functional properties of HMS and the control of its performance as a matured thermoelectric material. Another objective of the work presented in this chapter is to design the processing route allowing the production of highly pure and fully dense HMS materials in a reproducible manner.

This is to be accomplished through the experimental investigations of the microstructural and structural parameters associated with the synthesis of HMS. The goal is to evaluate the influence of the composition (Mn/Si ratio), the process (liquid-phase, spark plasma sintering and reactive sintering), the doping (Ge and Cr micro-substitutions) on the HMS highlights (γ value, inco/commensurate character and lack or presence of MnSi striations).

Various techniques and approaches, coupling metallurgy and solid state chemistry, are combined

to characterize the microstructure of HMS materials and identify the particular $MnSi_\gamma$ phase:

- The microstructure is characterized with SEM, EPMA and EBSD techniques, and rationalized using CALPHAD approach and the Scheil-Gulliver simulation.
- The structure is studied by refining the X-ray powder diffraction diagrams using a pattern-matching approach based on a (3+1)D superspace group concept. This allows to treat the different HMS phases as a unique modulated superstructure with a modulated vector γ in the c direction. It is then possible to correlate the composition to the crystal structure via the value of γ and thus precisely identify which HMS phase is formed.
- The inco/commensurate character of HMS alloys is examined by electron diffraction in a transmission electron microscope through the detection of spot anomalies.

This chapter is structured in four sections that propose a detailed process-dependent study of microstructural and structural parameters for HMS based alloys.

The first section details the methodology we have developed to systematically study HMS alloys.

The second section is dedicated to the characterization of HMS alloys prepared by solidification and the effects of Ge and Cr doping on the microstructure and commensurability. The results are discussed in the third section.

Finally, the fourth section introduces an innovative route to synthetize HMS alloys via reactive sintering. The development of this new route is achieved thanks to the careful study of HMS formation in the previous sections.

Through this chapter we will see how metallurgy and solid state chemistry fields can be coupled to gain a better understanding of HMS alloys.

2.1 Methodology

In this first part, the experimental techniques and methods used to characterize and to interpret the microstructure, the phases and the inco/commensurate character of HMS alloys will be presented.

Microstructure characterization and interpretation

Microstructural characterization was performed by Scanning Electron Microscopy (SEM, Vega Tescan). The microstructures will be presented in Back-Scattered Electron (BSE) mode to image the chemical contrast or in Secondary Electron (SE) mode for topography analysis. In addition, Electron Back-Scattered Diffraction (EBSD) is also performed with EDAX system in order to analyze the grain size, shape and orientation. Orientation Imaging Micrograph (OIM) of as-cast alloys highlights the grain shape and crystallographic orientation simultaneously. A detailed description of the EBSD technique will be presented in chapter 3 as this chapter is dedicated to the investigation of the texture in HMS alloys. Electron Probe Micro-Analyzer (EPMA, CAMECA SX100) device is used to evaluate the phase compositions.

The formation of the microstructures in the Mn-Si binary system and in the ternary Ge-Mn-Si and Cr-Mn-Si systems will be interpreted with the help of the computational thermodynamic using the ThermoCalc software and a CALPHAD description of the Cr-Ge-Mn-Si quaternary system investigated by the Institut Charles Gerhardt Montpellier (member of the present ANR consortium) [1, 2, 3, 4]. The CALPHAD (CALculation of PHAse Diagrams) method can be understood as minimization process of the total Gibbs free energy from well established phenomenological models to experimental values and observations. This requires that the Gibbs free energy of all the competing phases can be assessed. In order to generate the most accurate free energy functions, prototype alloy samples were produced, and first principles calculations were carried out to complete the literature data. The results of the Density Functional Theory calculations were introduced as "pseudo-experimental" parameters in order to complement the available data set. Emphasis was put on the description of the phases involved in the microstructure of HMS-based alloys. The diamond_A4 solid solution was treated as a substitutional solid solution with one sub-lattice $(Mn,Si,Ge)_1$. Its molar Gibbs energy of mixing was expressed by a sub-regular solution model in which composition dependence is based on the Redlich-Kister equation. The MnSi intermetallic phase was treated as a stoechiometric compound exhibiting extensions in the ternary Cr-Mn-Si and Ge-Mn-Si systems. It was described by the following sub-lattice model: $(Cr,Mn)_{0.5}(Ge,Si)_{0.5}$. In order to take into ac-

count the narrow homogeneity range of the HMS phase in the binary Mn-Si system, this compound was treated with four sub-lattices: $(Mn)_{0.146}(Mn,VA)_{0.22}(Mn,Si)_{0.244}(Si)_{0.39}$. HMS phase is modeled with vacancies in Mn site and anti-sites for the Si site. To take into account the extensions in the Cr-Mn-Si and Ge-Mn-Si systems, Cr and Ge where introduced in the 4 sub-lattices as follows: $(Cr,Mn)_{0.146}(Cr,Mn,VA)_{0.22}(Ge,Mn,Si)_{0.244}(Ge,Si)_{0.39}$ leading to a Cr substitution on Mn sites and a Ge one on Si sites. The thermodynamic parameters evaluated in the description of the Cr-Ge-Mn-Si system are listed in table 2.1.

Figure 2.1 presents Mn-Si phase diagram and a zoom close to HMS phase field calculated using ThermoCalc and the above thermodynamic description. HMS phase presents a non-congruent melting point and its formation during cooling is the result of the invariant peritectic reaction:

$$\text{MnSi} + \text{Liq} \rightarrow \text{MnSi}_\gamma$$

The solidification of HMS alloy is achieved after the eutectic invariant reaction. From the phase diagram the solidified microstructure of HMS alloys is expected to contain primary MnSi dendrites, HMS phase and Si eutectic aggregates.

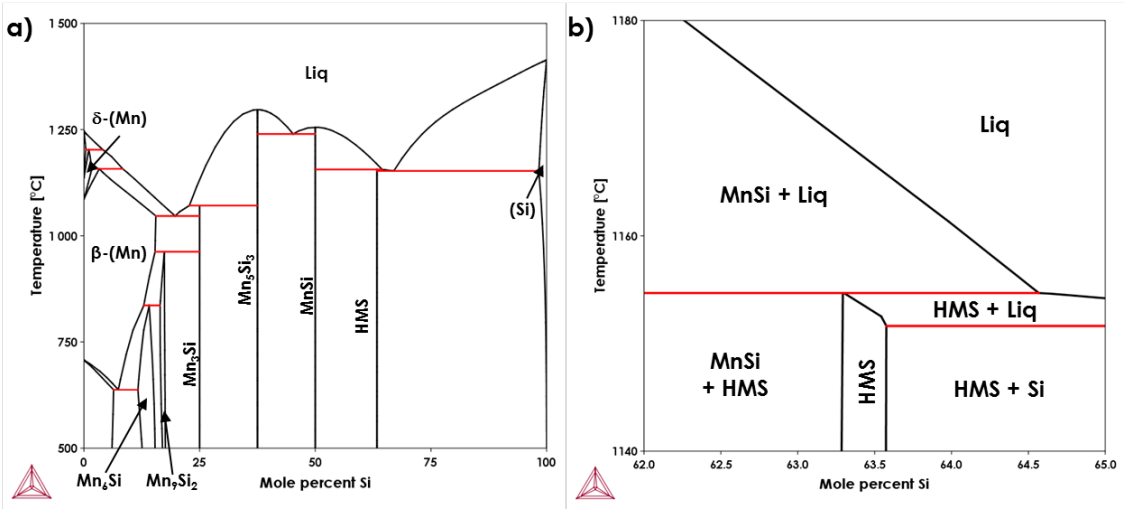

Figure 2.1: *Calculated Mn-Si binary phase diagram (a) and enlargement close to HMS phase field (b) from CALPHAD assessment showing the non-congruent melt of HMS.*

Phase and Model	Parameters (J/mol)
Diamond_A4 $(Mn,Si,Ge)_1$	G(Diamond_A4,Si) = G_{Si}^{SER}
	G(Diamond_A4,Mn) = G_{Mn}^{SER} + **1 000**
	G(Diamond_A4,Ge) = G_{Ge}^{SER}
	L(Diamond_A4,Mn,Si) = **-21 330**
	^{0}L(Diamond_A4,Ge,Mn) = **22 000**
	^{0}L(Diamond_A4,Ge,Mn,Si) = **-140 000**
B20_MnSi $(Cr,Mn)_{0.5}$ $(Ge,Si)_{0.5}$	G(B20_MnSi) = **29**
	G(B20_MnSi,Mn:Ge) = **- 8 000 - 0.5*T** + 0.5*G_{Mn}^{bcc} + 0.5*G_{Si}^{diam}
	L(B20_MnSi,Mn:Ge,Si) = **8 000**
	^{0}L(Cr,Mn:Ge) = **700 - 27*T**
	^{1}L(Cr,Mn:Ge) = **-5 500 + 5*T**
	^{2}L(Cr,Mn:Ge) = **6 500 - 7*T**
	^{0}L(Cr:Ge,Si) = **6 000 - 1.5*T**
	^{1}L(Cr:Ge,Si) = **100 + 3*T**
MnSi$_\gamma$ $(Cr,Mn)_{0.146}$ $(Cr,Mn,VA)_{0.22}$ $(Ge,Mn,Si)_{0.244}$ $(Ge,Si)_{0.39}$	G(MnSi$_\gamma$,Mn:Mn:Si:Si) = **-35 930 + 7.68*T** + 0.366*G_{Mn}^{SER} + 0.634*G_{Si}^{SER}
	G(MnSi$_\gamma$,Mn:VA:Si:Si) = **-12 000 + 4*T** + 0.146*G_{Mn}^{SER} + 0.634*G_{Si}^{SER}
	G(MnSi$_\gamma$,Mn:Mn:Mn:Si) = **-25 000 + T** + 0.610*G_{Mn}^{SER} + 0.390*G_{Si}^{SER}
	G(MnSi$_\gamma$,Mn:VA:Si:Si) = **-15 000 + 4*T** + 0.146*G_{Mn}^{SER} + 0.634*G_{Si}^{SER}
	^{0}L(MnSi$_\gamma$,Mn:Mn,VA:Si:Si) = **-6 990**
	^{0}L(MnSi$_\gamma$,Mn:Mn,VA:Mn,Si:Si) = **425 800**
	^{0}L(MnSi$_\gamma$,Mn:Mn:Mn,Si:Si) = **-4 460**
	G(MnSi$_\gamma$,Mn:Mn:Si:Ge) = **-11 000 - 0.5*T** + 0.366*G_{Mn}^{bcc} + 0.39*G_{Ge}^{diam} + 0.244*G_{Si}^{diam}
	G(MnSi$_\gamma$,Mn:Mn:Ge:Si) = **-11 000 - 0.5*T** + 0.366*G_{Mn}^{bcc} + 0.244*G_{Ge}^{diam} + 0.39*G_{Si}^{diam}
	G(MnSi$_\gamma$,Mn:Mn:Ge:Ge) = 0.366*G_{Mn}^{bcc} + 0.634*G_{Ge}^{diam}
	G(MnSi$_\gamma$,Mn:VA:Ge:Ge) = 0.146*G_{Mn}^{bcc} + 0.634*G_{Ge}^{diam}
	G(MnSi$_\gamma$,Mn:Mn:Mn:Ge) = 0.61*G_{Mn}^{bcc} + 0.39*G_{Ge}^{diam}
	G(MnSi$_\gamma$,Mn:VA:Mn:Ge) = 0.39*G_{Mn}^{bcc} + 0.39*G_{Ge}^{diam}
	G(MnSi$_\gamma$,Cr:Si) = **-30 000 + 6*T** + 0.366*G_{Cr}^{bcc} + 0.634*G_{Ge}^{diam}
	^{0}L(Mn:Mn:Si:Ge,Si) = **-5 000**
	^{0}L(Mn:Mn:Ge,Si:Si) = **- 5 000**
	^{0}L(Mn:Mn:Ge,Si:Ge,Si) = **-7 000**
	^{0}L(Cr:Ge,Si) = **5 000**

Table 2.1: *Model and optimized thermodynamic parameters for the phases involved during HMS formation, VA designates vacancies and optimized values are in bold type [1, 2, 4, 3].*

HMS phase identification

As mentioned in chapter 1, the need of identifying a particular HMS phase arises from the specificity of HMS. The difficulty of this task is due to the number of different concepts and methods used to describe the HMS structure, and there is a controversy regarding the existence of a series of different commensurate phases or a single incommensurate structure. It is commonly recognized that HMS are Nowotny Chimney-Ladder phases based on two interpenetrating sub-systems: a β-Sn tetragonal arrangement of Mn atoms (chimney) and a helical arrangement of Si atoms (ladders), with both being aligned along the c-axis of the tetragonal unit cell (see figure 2.2).

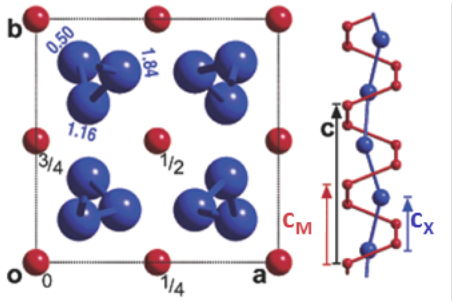

Figure 2.2: *Example of Nowotny Chimney Ladder structure for Ru_2Sn_3 with a view down the c axis (left) and a perpendicular view showing the helices (b) (reproduction of [5]).*

Notwithstanding, there are two different concepts to describe the structure of HMS: the concept of several commensurate phases which differ slightly in their composition and the concept of a single one-dimensionally incommensurate phase. These two concepts arise from a simple structure building principle: since the [Mn] and [Si] periods have different length along the c-axis, different numbers of stacked sub-systems are possible to form a repeatable unit cell. If the ratio can be expressed as simple integers the crystal structure can be represented by a single unit cell with a finite parameter c. In contrast, if the ratio is irrational, the lattice is infinite in the c direction, and we then have to assume an incommensurate modulated structure. In the concept of commensurate phases, a relative large unit cell has to be assumed to account for the c-axis lengths difference. For this approach, the agreement between the approximate commensurate structure and the observed X-ray reflections is enhanced as the number of independent positional fitting parameters increases. That is how four different HMS phases, i.e. Mn_4Si_7 [6], $Mn_{11}Si_{19}$ [7], $Mn_{15}Si_{26}$ [6, 8] and $Mn_{27}Si_{47}$ [9, 10], have been reported between 1964 and 1973 with atomic positions determined with X-ray diffraction. Their unit cell parameters are reported in table 2.2.

Parameters	$\mathbf{Mn_4Si_7}$	$\mathbf{Mn_{11}Si_{19}}$	$\mathbf{Mn_{15}Si_{26}}$	$\mathbf{Mn_{27}Si_{47}}$
a	5.526	5.530	5.502	5.530
c	17.517	47.763	65.284	117.9
m	16	44	60	108
n	28	76	104	188
m/n	1.75	1.72727...	1.73333...	1.74074...

Table 2.2: *Lattice parameters for Mn_4Si_7, $Mn_{11}Si_{19}$, $Mn_{15}Si_{26}$ and $Mn_{27}Si_{47}$ from* [11, 12, 6, 10]. *a and c in Å, m and n respectively the numbers of Mn and Si atoms in the unit cell and the m/n ratio are reported for the different HMS phases.*

Other commensurate phases, i.e. Mn_7Si_{12}, $Mn_{19}Si_{33}$, $Mn_{26}Si_{45}$ and $Mn_{39}Si_{68}$ have been mentioned in high-resolution electron microscopy studies [13] and electron diffraction studies [13, 14, 15]. Their identification results from the methodology applied to interpret electron diffraction patterns. Due to the long c-parameter, electron diffraction patterns for [uv0] zone axes contain intense spots and linear sequence of regularly spaced weaker spots (see figure 2.3).

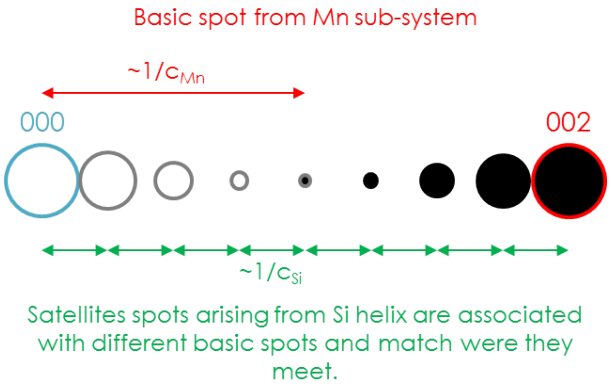

Figure 2.3: *Schematic representation of an electron diffraction pattern taken along [-120] zone axis. The basic spot arising from [Mn] sub-system is highlighted with a red contour and in between the (000) and (002) basic spots a sequence of 7 satellites spots is drawn.*

According Ye and Amelinckx [13] and De Ridder and Amelinckx [14] the most intense spots are basic reflections arising from the tetragonal [Mn] sub-system, and with each of these basic spots the row containing equidistant satellite spots are caused by the Si helix. These satellite reflections denote the periodicity and c-length of the Si helix, and so are the finger print of a particular commensurate HMS phase. When the sequences of satellites associated with different basic spots do not match where

they meet, it is interpreted as the manifestation of slight difference in c_{Si}, and the method to derivate the theoretical composition consists to find the common multiple for c_{Mn} and c_{Si}. In other words, the analysis of the spot positions and number is used to distinguish between different HMS phases.

An alternative and perhaps better approach to describe the structure of HMS can be found in the crystallography of aperiodic crystals (incommensurate modulated crystals, composite crystals and quasicrystals) [16]. The building principle of incommensurate crystals considers a periodic superstructure in which the displacement of atoms are obtained as the value of a modulation function that does not have a periodicity equaling the superlattice period (see figure 2.4). Incommensurate composite crystals are compounds that can characterized as the intergrowth of several incommensurately modulated subsystems. The resulting structure does not have translation symmetry but long-range order exists, provided that the shapes and amplitudes of the modulation waves are known. Consequently, the determination of the modulation vectors is the main task to identify to characterize incommensurate crystals.

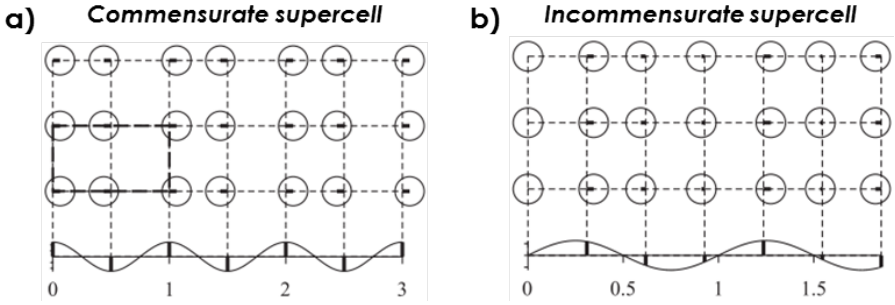

Figure 2.4: Crystal structures with displacement modulations for commensurate (a) and incommensurate cases (b) (reproduction of [16]).

Because perfect long-range order exist in aperiodic crystals, they scatter X-rays (and electrons) in the form of Bragg reflections as periodic crystals do. Electron diffraction pattern of incommensurate composite crystals are obtained as the superposition of diffraction patterns of each substructure exhibiting basic reflections surrounded by equally spaced satellite reflections that result from the interaction between the sub-systems (see figure 2.5). When the [Mn] and [Si] sub-systems have independent periods along the c direction (incommensurate phase), the diffraction pattern exhibit spacing and orientation anomalies of the satellite spots (see figure 2.6) which reveal that the periodicity and position of the Si helices changes continuously. For such situations, it can be conclude that the HMS phase is

incommensurate. In contrast, if both [Mn] and [Si] sub-systems match for a given number of stacking the satellites spots are superposed (see figure 2.6) and for such situations it can be conclude that the HMS phase is commensurate.

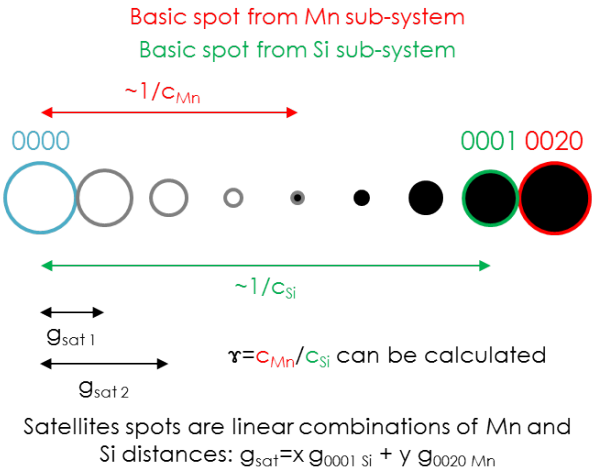

Figure 2.5: *Schematic representation of an electron diffraction pattern taken along [-120] zone axis. The basic spots arising from [Mn] and [Si] sub-systems are respectively highlighted with a red and green contour, and in between the (0000) and (0020) [Mn] basic spots a sequence of 6 satellites spots is drawn that are linear combinations of Mn and Si distances. In this description the spots are indexed with 4 indices.*

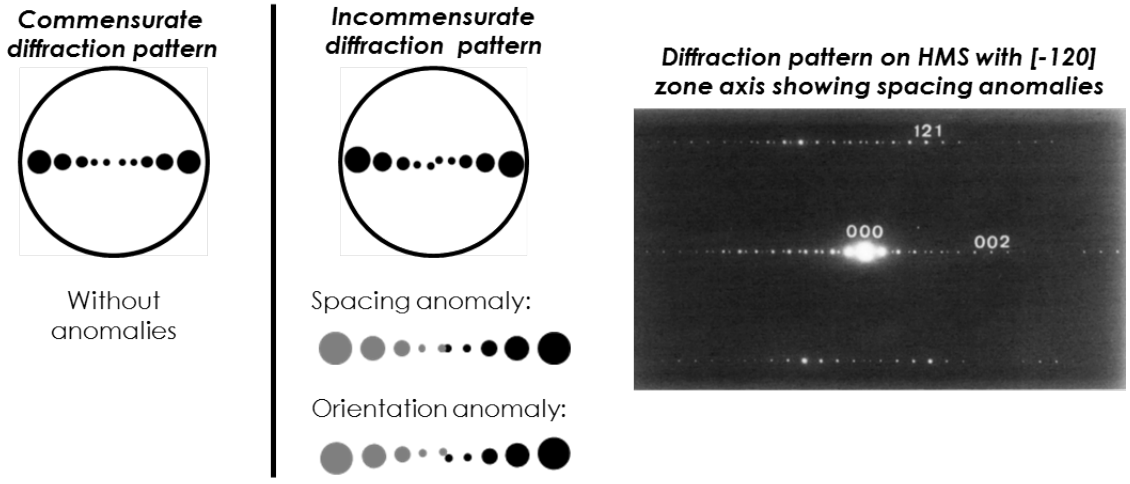

Figure 2.6: Commensurate (left) and incommensurate (middle) diffraction patterns taken along [-120] zone. For the incommensurate case spacing and orientation anomalies are represented. An example of diffraction pattern taken along [-120] zone for HMS alloys showing spacing anomalies from Ye et al. work [13] is reported (right).

An elegant solution to index the diffraction patterns of composites crystals is provided by the superspace group approach which involves four reflection indices (hklm): 3 for the main Bragg reflections of the basic structure (hkl) and a fourth (m) for the satellite reflection. The superspace is a 4-dimensional space in which the first three coordinate axes represent the 3D physical space, and the fourth coordinate axis represent the modulation [17].

In the case of HMS, only one modulation vector is required to describe the displacement of atoms in the incommensurate c-direction. Based on these considerations, Kikuchi and Miyazaki [18, 19] developed an approach that allow to uniformly treat all the HMS phases as a single compound MnSi$_\gamma$ where γ is the ratio c_{Mn}/c_{Si}. It is then possible to directly correlate the composition to the crystal structure, provided that γ is accurately determined. Miyazaki *et al.* [19] employed a high resolution neutron powder diffraction technique and the superspace group approach to investigate the modulated structure of HMS produced by arc-melting.

However, to our best knowledge, no structure analysis based on the refinement of XRD and electron diffraction data using the superspace group concept has been systematically applied to evaluate the effect of the processing route on the structure of HMS. Inspired by the work of Kikuchi and Miyazaki, we have performed a global least square refinement of the X-ray diffraction diagrams (with JANA2006 software) to precisely extract the intensity and position of the peaks without structural model (profile-matching using the Le Bail method).

To perform the profile matching we first fit the peaks corresponding to the [Mn] sub-system with β-Sn type arrangement using a 3D space group: $I4_1/amd$. Secondly, we use a (3+1)D superspace group: $I4_1/amd(00\gamma)00ss$ to perform the complete profile refinement including [Si] sub-system and satellite peaks (see figure 2.7). Each sub-system will be indexed with a space group with a common a parameter and differs in c direction depending on the atomic arrangement. Increase the order in satellites peaks is linked to an increase of their intensity with order.

The fundamental reflections for [Mn], [Si] and satellites peaks are respectively denoted *hkl0, hk0m* and *hklm*. With this approach a fine change in γ value is easily observed in the diffraction pattern and results in a change on the position of the main peak of [Si] (1101) located near 42.5°. To illustrate this point, simulated XRD profiles obtained by fixing the γ value are superposed and shown on figure 2.8.

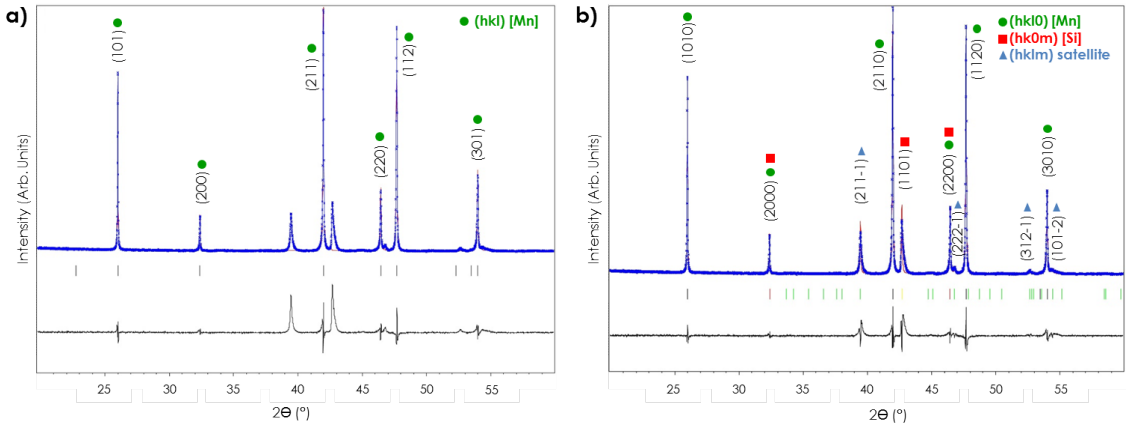

Figure 2.7: *Profile matching for [Mn] sub-system with $I4_1/amd$ space group (a) and complete profile matching with $I4_1/amd(00\gamma)00ss$ (3+1)D superspace group (b). Observed (blue), calculated (red), and difference (black) patterns of powder XRD for $MnSi_{1.73}$ as-cast alloy measured at 298 K. Short vertical lines below the pattern indicate positions of Bragg reflections: black for [Mn], yellow for [Si] and green for satellites. The red short lines indicate common reflections of [Mn] and [Si]. The difference line shows the agreement between the observed and calculated intensities. The XRD patterns are indexed with 3 indices (a) and 4 indices (b) for respectively 3D space and (3+1)D superspace groups.*

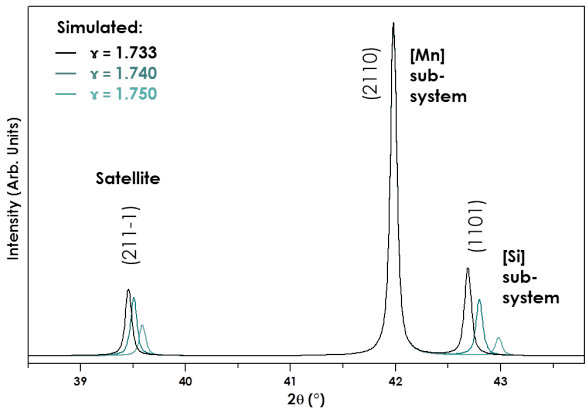

Figure 2.8: *Simulated XRD patterns for different values of c-axis ratio (γ) illustrating the sensitivity of the applied method.*

We can see that a small variation of γ value has a strong impact on the positions of the main peak of [Si] (1101) and the satellite (211-1) meanwhile the main [Mn] peak (2110) is not affected. This simulation highlights the sensitivity of the approach.

To perform this study long XRD acquisition conditions were used in order to limit the fluorescence phenomenon of the Mn with the copper radiation and obtain high resolution data. XRD patterns were collected for more than 60 h with a step of 0.0084 in 15° to 130° range on PANalytical X'Pert Pro Cu

$K_{\alpha 1}$ device (equipped with a monochromator).

The refinement of high resolution XRD patterns using the superspace group approach will provide a precise measurement of the γ value allowing to identify a particular commensurate phase, however it is not enough to discriminate between a commensurate phase and an incommensurate compound because it is not possible to experimentally distinguish between an irrational number and some rational approximant. To solve this problem, we relied on electron diffraction technique as explained above.

Electron diffraction patterns were obtained thanks to Transmission Electron Microscopy (TEM, JEOL 2100). The analysis of HMS alloys is performed on powder or on foils depending on their aim. The foils are extracted from as-cast alloys by Focused Ion Beam (FIB) technique with Ga^+ ions. The diffraction patterns are observed with an axis zone permitting the observation along the c-axis of the crystal structure: [-120] zone axis.

2.2 Synthesis, structure and microstructure of HMS alloys

2.2.1 Effect of the nominal composition

Experimental procedure

To investigate the microstructural parameters involved during HMS alloys production we choose a liquid-phase process: arc melting technique (Bülher MAM-1 device) that is classically used to produce HMS alloys. Commercial Mn (99.9%) and Si (99.9999%) chips provided respectively by Strem Chemical CAS [7439-96-5] and Alfa Aesar CAS [7440-21-3] were weighted in appropriate amounts and placed in the copper crucible of the arc melter. Batches of 4 g were melted three times under Argon atmosphere in order to ensure the homogeneity of the samples. Pure titanium was melted prior to any melting step to guarantee oxygen free atmosphere in the chamber. After the synthesis the samples were weighted in order to control the losses. Samples exhibiting a loss less than 0.5% of sample mass were selected for characterization.

Long annealing treatments were conducted on as-cast ingots to equilibrate the samples and explore the structural stability of HMS. The thermal treatments were performed in quartz tubes (sealed under vacuum) at 700°C and 900°C during 43 days followed by quench into water.

Four nominal compositions $MnSi_\gamma$ with γ=1.70, 1.73, 1.75 and 1.77 were prepared and are reported in Mn-Si binary system (see figure 2.9). The nominal compositions are selected to surround the region close to HMS phase field. Through this set of experiments we sought for nominal composition influence on HMS phase and secondary phases amount.

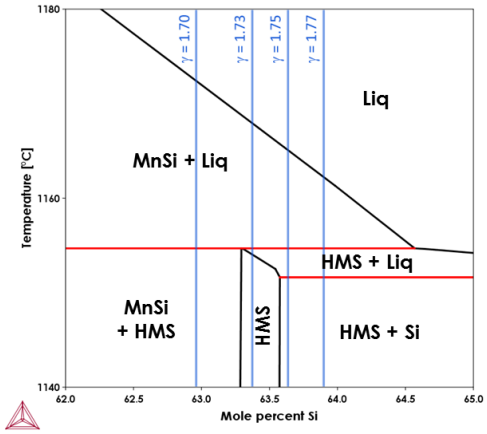

Figure 2.9: *Mn-Si binary phase diagram close to HMS phase field from CALPHAD assessment from Berche et al. [1]. The four studied nominal compositions MnSiγ with γ=1.70, 1.73, 1.75 and 1.77 used to scan HMS phase field region are reported.*

Microstructure characterization

Figure 2.10 presents the powder XRD patterns for the four as-cast compositions.

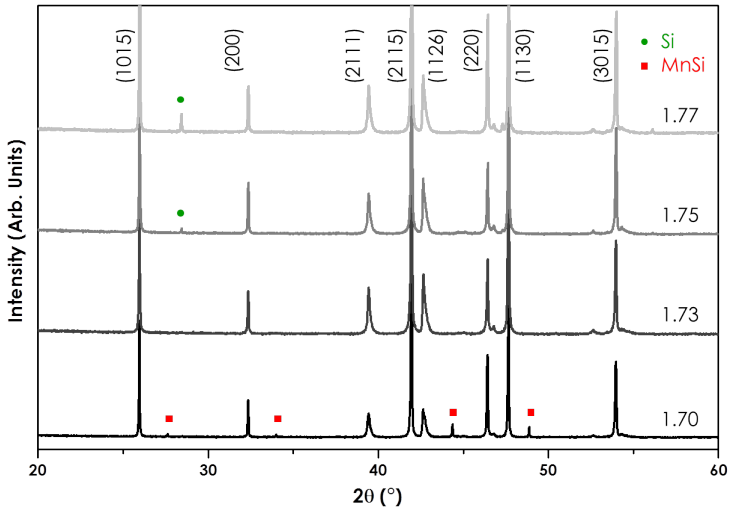

Figure 2.10: *XRD patterns for four different nominal compositions (γ=1.70-1.77) as-cast. HMS phase peaks are indexed with the commensurate $Mn_{15}Si_{26}$ phase (ICSD #15339). Si and MnSi secondary phases are shown in green circle and blue square, respectively.*

All the different alloys exhibit HMS phase and different secondary phases: MnSi for nominal composition γ=1.70 and pure Si for γ=1.75 and 1.77. For γ=1.73 no secondary phases are detected (within the detection limit of XRD technique). In addition, an increase in Si content from γ=1.75 to

γ=1.77 in nominal composition leads to an increase in pure Si phase amount. As expected for liquid phase process the proportion of the secondary phases depends on the nominal composition.

The typical microstructures for the four as-cast alloys as a function of the nominal composition are shown on figure 2.11. Si eutectic aggregates located at HMS grain boundaries and primary MnSi dendrites typical of HMS casted alloys are observed. Defects as micro-cracks are evidenced due to thermal stress because of rapid melting and cooling rates during arc melting process. Phase composition EPMA confirm the presence of Si and MnSi in agreement with previous XRD results. For γ=1.73 a low content of MnSi and Si secondary phases is evidenced on figures 2.11.e. and 2.11.g. (not detected by XRD).

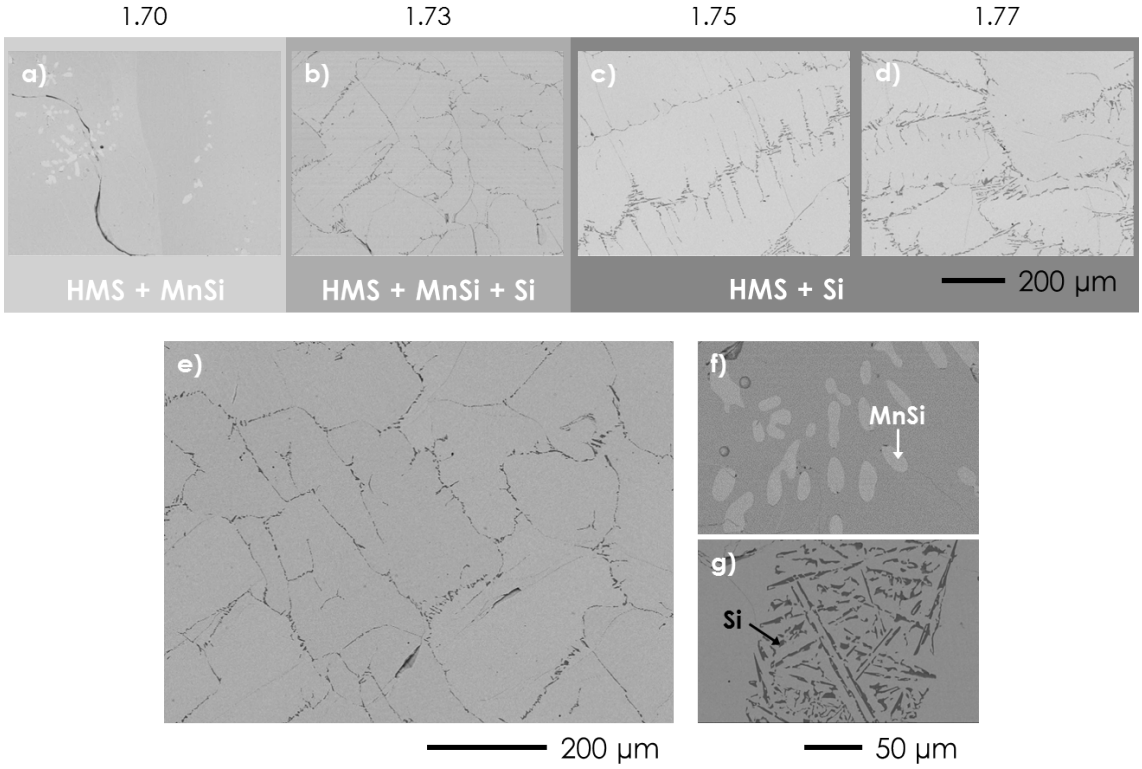

Figure 2.11: *BSE images for four different nominal compositions (γ=1.70-1.77) as-cast (a-d) and detailed microstructures for γ=1.73 as-cast alloy (e-g).*

To further analyze HMS alloys we will focus our analysis on $MnSi_{1.73}$ as-cast alloy. Its microstructure is well interpreted from the calculated phase diagram shown on figure 2.1 and the Scheil-Gulliver simulation shown in figure 2.12. The sequence of transformation leading to the microstructure is as follows. At 1168°C the liquidus is reached and the alloy starts to solidify with nucleation of MnSi.

Upon cooling the liquid moves along the liquidus line and reaches the peritectic point where it reacts with the primary MnSi dendrites to form HMS. Because the rate of the peritectic reaction is too slow, it does not go to completion and the remaining liquid follows the liquidus leading to the solidification of HMS. This regime remains until the liquid reaches the eutectic point at 1152°C where it completely solidifies without further cooling.

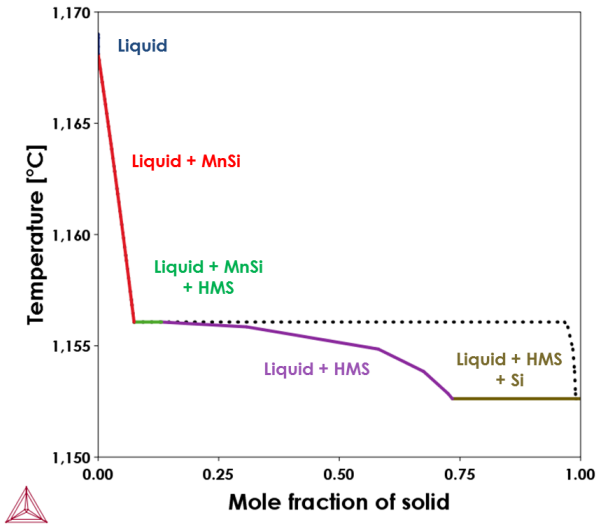

Figure 2.12: *Solidification path for an alloy of nominal composition* $MnSi_{1.73}$ *calculated with Scheil-Gulliver model.*

Besides that when an additional polishing or etching step is performed on the alloy shown on figure 2.11.e., a new feature of the microstructure is evidenced into HMS matrix: MnSi striations periodically distributed in each grain (see figure 2.13). From the thermodynamic description of Mn-Si phase diagram [1] the formation of the striations during the solidification cannot be explained by the two invariant phase transformations previously discussed.

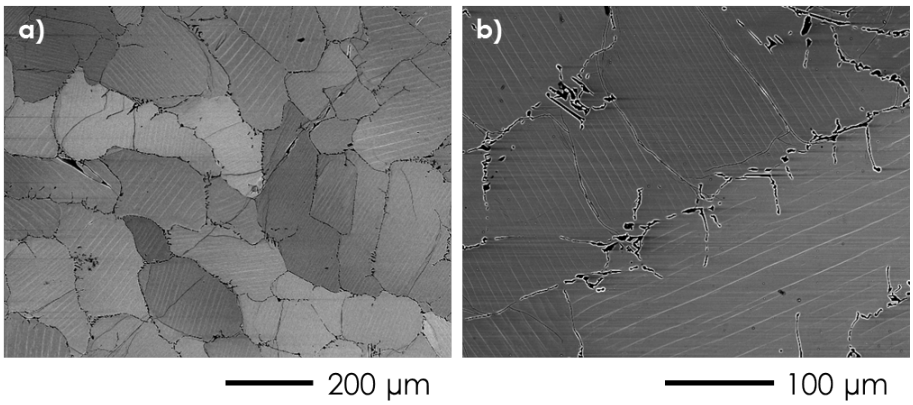

Figure 2.13: *BSE images in crystallographic contrast highlighting MnSi striations in HMS matrix (a) and enlargement (b) for $MnSi_{1.73}$ as-cast alloy.*

Figure 2.14 shows an OIM map where we can observe that the sample is composed of large grains of few hundreds of µm. We can also note an orientation relation between the grain and the striations. As a consequence, the inter-striation distance observed in 2D is function of the grain orientation. These results are supported by the literature [20, 21] where striations with composition corresponding to MnSi are found to be perpendicular to the c-axis of the crystal structure.

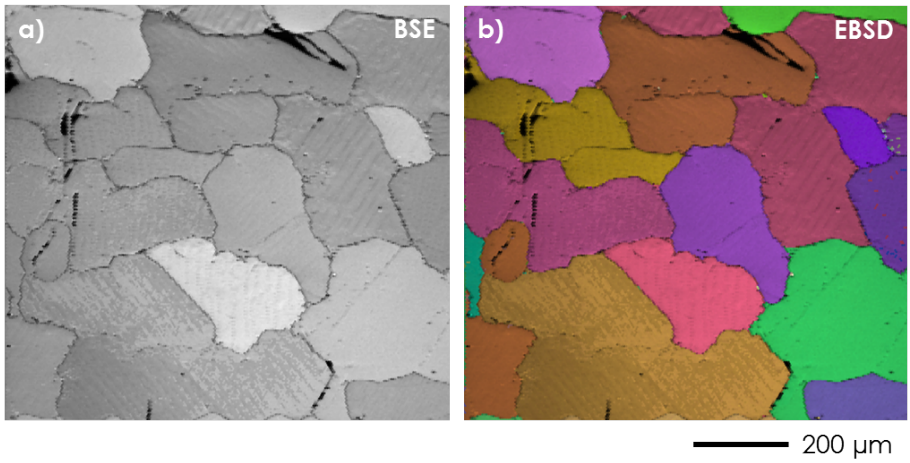

Figure 2.14: *BSE image (a) and the corresponding OIM map (b) for $MnSi_{1.73}$ as-cast alloy.*

To characterize the striations a foil was extracted from an as-cast alloy (see figure 2.15.a.). The fine short black lines correspond to the print of (001) basal planes, we therefore confirm that MnSi striations are parallel to (001) planes. A view of the foil analyzed by TEM is shown on figure 2.15.b.

where we can distinguish two striations.

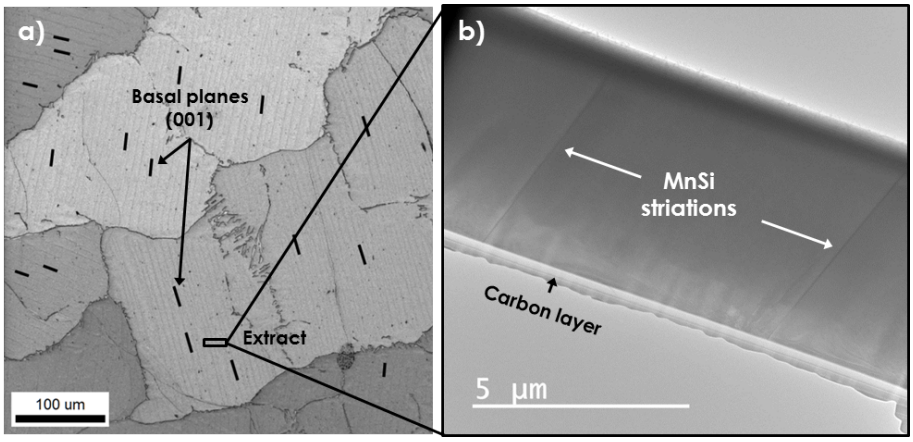

Figure 2.15: *BSE image of as-cast $MnSi_{1.73}$ alloy (a) where MnSi striations orientation is found to be parallel to the (001) basal planes (indicated with short black lines). View of TEM foil (b) extracted by FIB technique where MnSi striation and the inter-striation region will be characterized.*

The thickness of the striation measured on the TEM image shown on figure 2.16.a. is about 30 nm. Close to the striations it is then possible to observe the atomic planes of HMS phase. The waves formed by the atomic planes of the HMS matrix are due to the non-constant thickness of the foil. A diffraction pattern (see figure 2.16.b.) is taken in the center of the striation with a narrow diaphragm (∼6 nm) and a diffraction ring pattern is produced meaning that the striation is amorphous. The results obtained for the characterization of the striation are in agreement with Zhou *et al.* work [22].

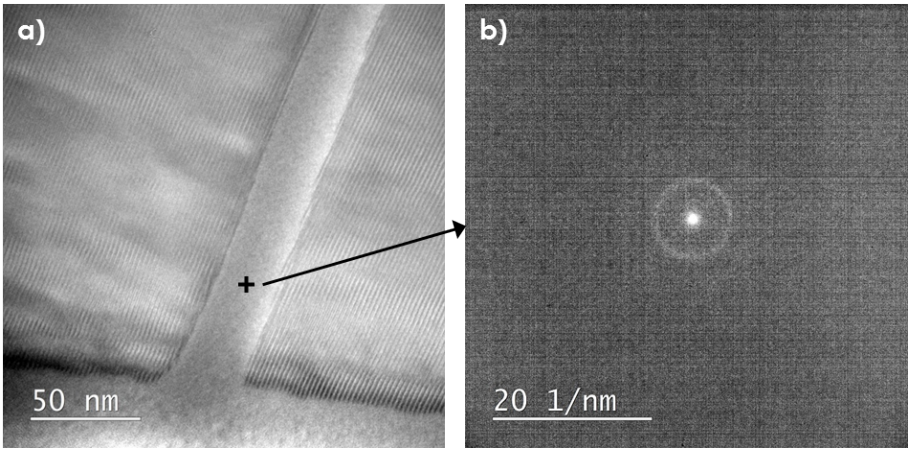

Figure 2.16: *View of the MnSi striation (a) and diffraction pattern of the analyzed zone (arrow) (b) showing an amorphous behavior of the striation.*

The thermal stability of MnSi striations is investigated by an annealing treatment at 1000°C during

43 days. The microstructures before and after annealing are shown in figure 2.17. We can see that despite the thinness of the striations, they present a remarkable stability even at 1000°C and cannot be solution treated. From Nishida *et al.* work [23] the stability of the MnSi striations in arc melted alloys is observed after a thermal treatment at 1100°C. At this stage, additional information are needed to understand the mechanism involved in the formation of the striations.

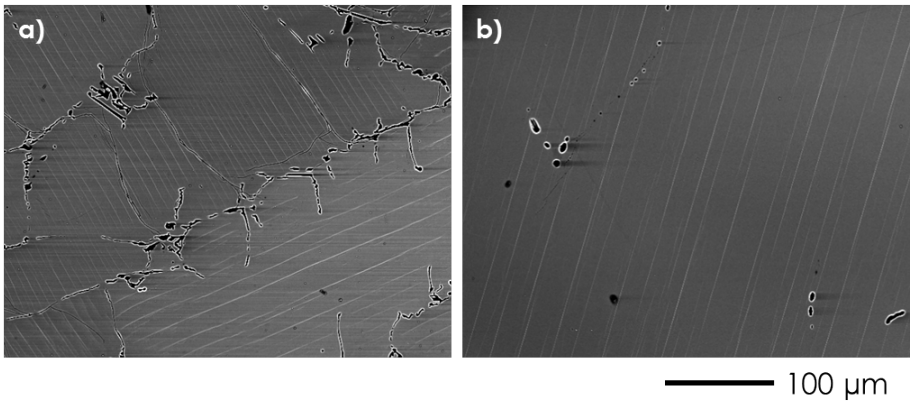

Figure 2.17: *BSE images of MnSi striations in $MnSi_{1.73}$ alloy before (a) and after annealing treatment at 1000°C during 43 days (b).*

HMS phase identification

In order to evaluate if the nominal alloy composition forms a particular HMS phase, we performed XRD profile matching analysis with the superspace group formalism for the 12 alloys: 4 different compositions and 3 different thermal history (as-cast and equilibrated at 700°C and 900°C).

Figure 2.18 presents a typical profile matching performed on an as-cast sample with nominal composition $MnSi_{1.73}$. The refined lattice parameters from profile matching are: a=5.5237(9) Å, c_{Mn}=4.3646(6) Å, c_{Si}=2.5177(3) Å and c-axis ratio γ=1.7339(8).

Table 2.3 summarizes the profile matching refinements for the 12 samples (as-cast and equilibrated). From the refined lattice parameters slight changes are observed for c-axis ratio (γ ranges from 1.7334(7) to 1.7389(2) value).

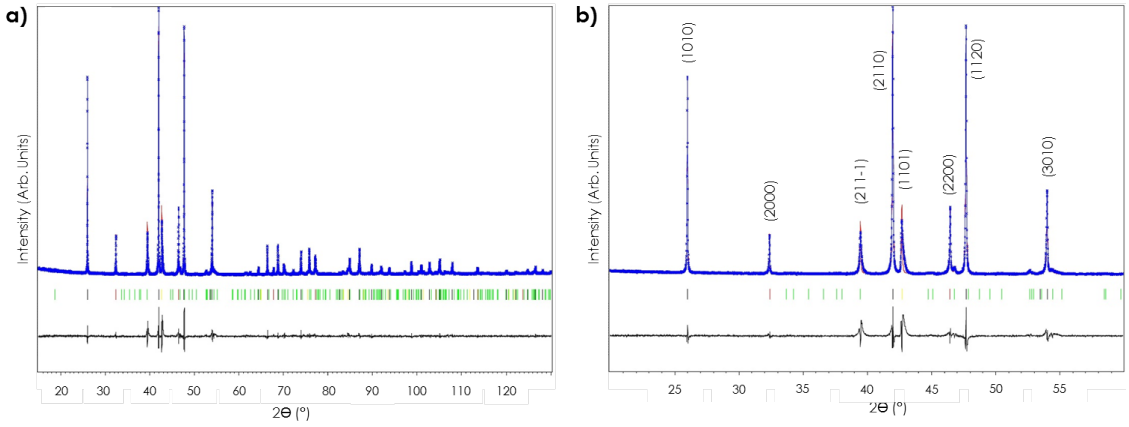

Figure 2.18: *Observed (blue), calculated (red), and difference (black) patterns of powder XRD for $MnSi_{1.73}$ as-cast alloy measured at 298 K. Short vertical lines below the pattern indicate positions of Bragg reflections: black for [Mn], yellow for [Si] and green for satellites. The red short lines indicate common reflections of [Mn] and [Si]. The difference line shows the agreement between the observed and calculated intensities. The left figure shows complete profile matching (a) and the right one shows an enlargement (b). Peaks are indexed with the $I4_1/amd(00\gamma)00ss$ superspace group.*

Nominal composition	State	a (Å)	c_{Mn} (Å)	c_{Si} (Å)	γ
1.70	As-cast	5.5235(5)	4.3651(6)	2.5181(4)	1.7334(8)
	Equilibrated at 700°C	5.5248(7)	4.3652(2)	2.5118(3)	1.7378(6)
	Equilibrated at 900°C	5.5255(0)	4.3650(1)	2.5101(8)	1.7389(2)
1.73	As-cast	5.5237(9)	4.3646(6)	2.5177(3)	1.7339(8)
	Equilibrated at 700°C	5.5256(5)	4.3648(1)	2.5117(3)	1.7377(7)
	Equilibrated at 900°C	5.5255(0)	4.3650(1)	2.5101(8)	1.7389(2)
1.75	As-cast	5.5234(6)	4.3646(0)	2.5178(3)	1.7334(7)
	Equilibrated at 700°C	5.5252(7)	4.3650(0)	2.5117(8)	1.7378(1)
	Equilibrated at 900°C	5.5236(8)	4.3648(5)	2.5171(1)	1.7340(7)
1.77	As-cast	5.5237(1)	4.3647(3)	2.5176(6)	1.7336(4)
	Equilibrated at 700°C	5.5250(3)	4.3651(2)	2.5119(8)	1.7377(2)
	Equilibrated at 900°C	5.5234(7)	4.3648(2)	2.5176(7)	1.7336(7)

Table 2.3: *Refined lattice parameters a, c_{Mn}, c_{Si} and γ obtained by profile matching for the four nominal compositions (γ=1.70, 1.73, 1.75 and 1.77). Each nominal composition is analyzed in the as-cast, equilibrated at 700°C and 900°C state.*

A close examination of the peak shape shows an asymmetric broadening of the Si reflections (see figure 2.19.a.). To our knowledge, it is the first time that such observations are reported. Peak broadening can arise from various phenomena such as stresses, strains, crystallize size, powder morphology,... However, we cannot invoke such origins because in the present case Mn reflections are not affected by the broadening but only the peaks arising from Si helices and to a less extend those resulting from the interaction between both sub-systems. This suggests that the broadening is intimately related to the period of the Si sub-system. As visible in the simulated pattern (see figure 2.19.b.), the asymmetric broadening can results from the mixture of different HMS phases. From this simulation, we can assume that the as-cast $MnSi_{1.73}$ alloy is composed of the three different commensurate phases: $Mn_{15}Si_{26}$ (i.e. γ=1.73333...) is the preponderant phase, and $Mn_{11}Si_{19}$ (i.e. γ=1.72727...) and Mn_4Si_7 (i.e. γ=1.75) phases are present in minority. Another explanation we can put forward to explain the asymmetric broadening of particular peaks is the existence of disorder of the helical arrangement of Si atoms along c-axis of the [Mn] sub-system. In others words we cannot exclude that such broadening of Si peaks is due to an incommensurate structure.

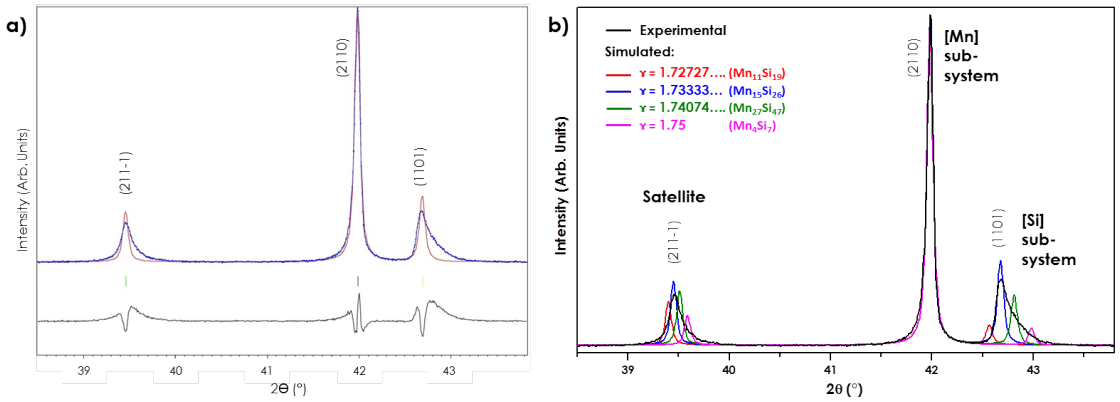

Figure 2.19: *Enlargement in PM for as-cast $MnSi_{1.73}$ alloy (a) and simulated XRD patterns of the four commensurate phases superposed on experimental data for as-cast $MnSi_{1.73}$ alloy (b).*

In an attempt to clarify this point, we have performed diffraction analysis in the [-120] HMS zone axis. The experiment was carried out on the FIB foil showed on figure 2.15.b. A typical diffraction pattern taken along [-120] HMS zone axis of the as-cast $MnSi_{1.73}$ alloy composition is provided in figure 2.20. The most intense spots are due to the basic reflections arising from the tetragonal [Mn] sub-system, i.e. 0020, 4200 marked with red contour and for [Si] sub-system the spot 0001 is highlighted with a green contour. With each of these basic spots a row containing 6 weaker equidistant satellite

spots are caused by the Si helix periodicity. The satellite spots are not shifted with respect to the basic spots (there is no spacing neither orientation anomalies observed in the diffraction pattern of the analyzed as-cast $MnSi_{1.73}$ alloy). It should be noted that the satellite spots are sharp, they intensity decrease with increasing order. One can conclude that the Si lattice period is well defined.

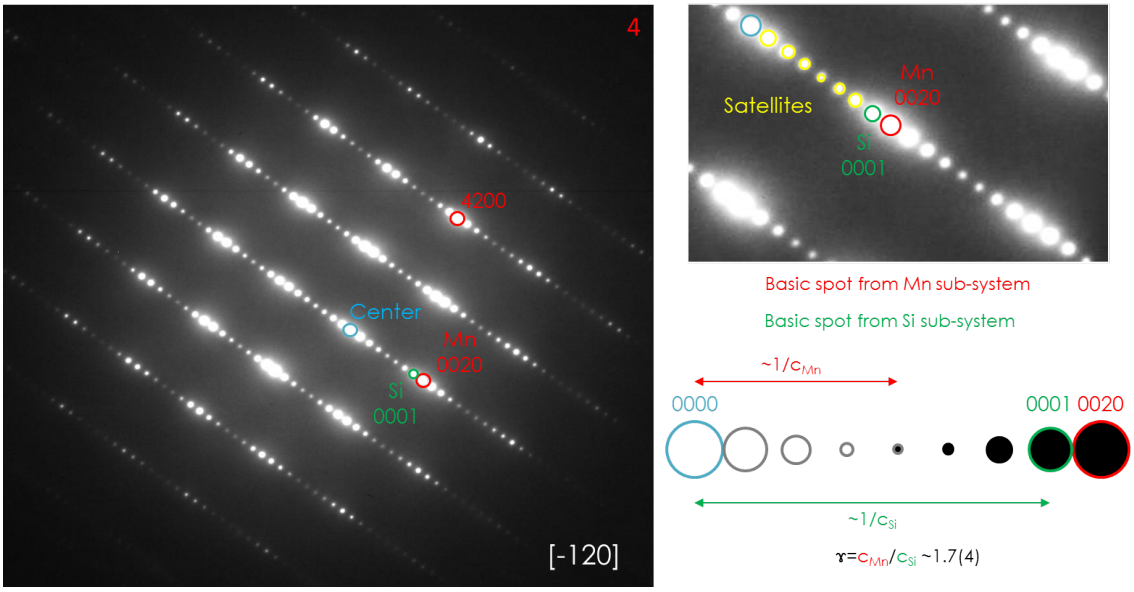

Figure 2.20: *Indexed commensurate diffraction pattern with [-120] zone axis (number 4 according to figure 2.21) taken in the inter-striation zone for an as-cast* $MnSi_{1.73}$ *alloy.*

Diffraction patterns were taken across the foil and the intensity of satellites spots was found to vary (see figure 2.21). The intensity of satellites spots increases from the center of the inter-striation region to the edges. This phenomenon is due to the lattice period, if the atomic sequence is well defined we can see many satellites peaks due to an increase in their intensity. In others words, if the ordering sequence of the helical Si atoms is periodically repeated the diffraction pattern will present a large number of satellite spots. We evidenced on a bulk sample in between two striations a continuously graded sequence in satellite spots intensity. The ordering sequence is well defined close to the striation and disorder is introduced when we get far to the striation.

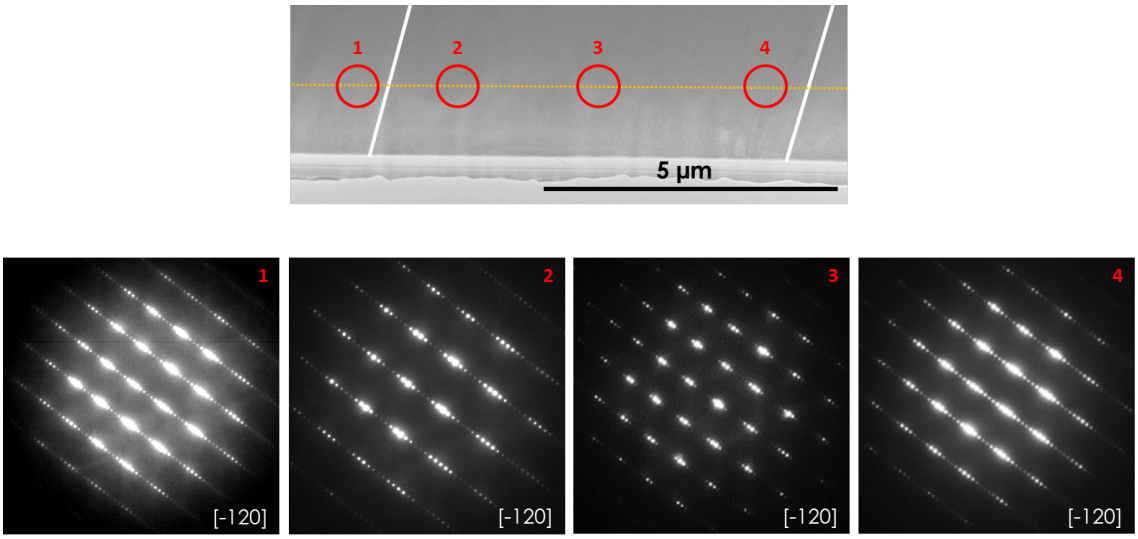

Figure 2.21: *Diffraction patterns taken across the foil for an as-cast $MnSi_{1.73}$ alloy. The diameter of the circle corresponds to the diaphragm surface. MnSi striations location are indicated with two white lines. This series of diffraction patterns highlights a change in satellite spot intensities between two MnSi striations.*

Casted materials present a mixture of HMS commensurate phases evidenced thanks to XRD and TEM analysis.
MnSi amorphous striations are periodically distributed in HMS matrix and are stable till 1000°C.
The nominal composition controls the amount of secondary phases but doesn't affect HMS structural highlights.

2.2.2 Effect of the spark plasma sintering

Ingots are too brittle in as-cast condition due to cracks and poor mechanical properties (pure elastic behavior). Thus, a post-processing step is required to improve their mechanical behavior and make them suitable for properties measurement and the fabrication of thermoelectric legs. The ingot is ground and consolidated by spark plasma sintering technique.

Densification Spark Plasma Sintering (SPS) technology was used to shape and densify the materials studied in this thesis. SPS is a non conventional technology that belongs to the Field Assisted Sintering Technology (FAST). SPS experiments were performed with Dr. Sinter lab 515S that is an Electrical Current Applied Sintering (ECAS) with uni-axial pressure. The sintering can be done under vacuum (<10 Pa) or with specific atmosphere. The electrical current that is delivered by series of DC current

pulses will increase the sample temperature thanks to Joule heating. In our case we have fix this ON-OFF DC pulsed current path at 12:2 (12 ON and 2 OFF). During the sintering few volts and an intensity up to 8000 A are applied that allows a very fast increase/decrease in temperature (hundreds of °C/min), the maximum heating rate is 500°C/min. For this technique no inductive nor capacitive effect is found only resistive effect is observed. The temperature is controlled by a pyrometer placed outside the chamber and pointing in a central hole designed in the mold. This technique can be used to many purposes: densification, reactive sintering, diffusion study, graded materials, welding, coating,... The advantages of this technique are numerous: sintering without additive, short time cycle, uniform density, high productivity and energy gain,... leading to high quality materials with low process cost, controlled porosity or highly dense materials [24].

The sintering cycle optimized for HMS alloys is shown on figure 2.22, various dwell temperatures are applied in this thesis depending on their aim.

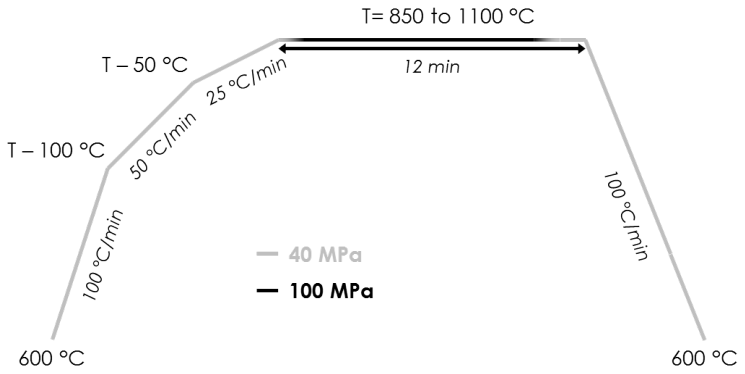

Figure 2.22: *SPS cycle optimized for HMS alloys where the pressure is applied during the dwell.*

The influence of the SPS parameters: heating/cooling rates, duration of the dwell , pressure cycle have been fixed after a set of experiments to end with their best combination to produce bulk dense HMS pellets. The sintering is achieved in a carbon die of 10 mm diameter that can support a maximum pressure of 100 MPa and a temperature of 2500°C. The pellets are done with 1.2 g of powder (sieved up to 40 µm) and the powder is surrounded by flexible graphite (Papyex ®) during the sintering.

The best sintering conditions were explored to end with highly dense materials in order to measure intrinsic transport properties (chapter 4). To this end, the dwell temperature was varied from 850°C to 1100°C every 50°C and the 6 corresponding microstructures after SPS densification are shown on figure 2.23. This optimization was achieved on $MnSi_{1.73}$ grounded powders.

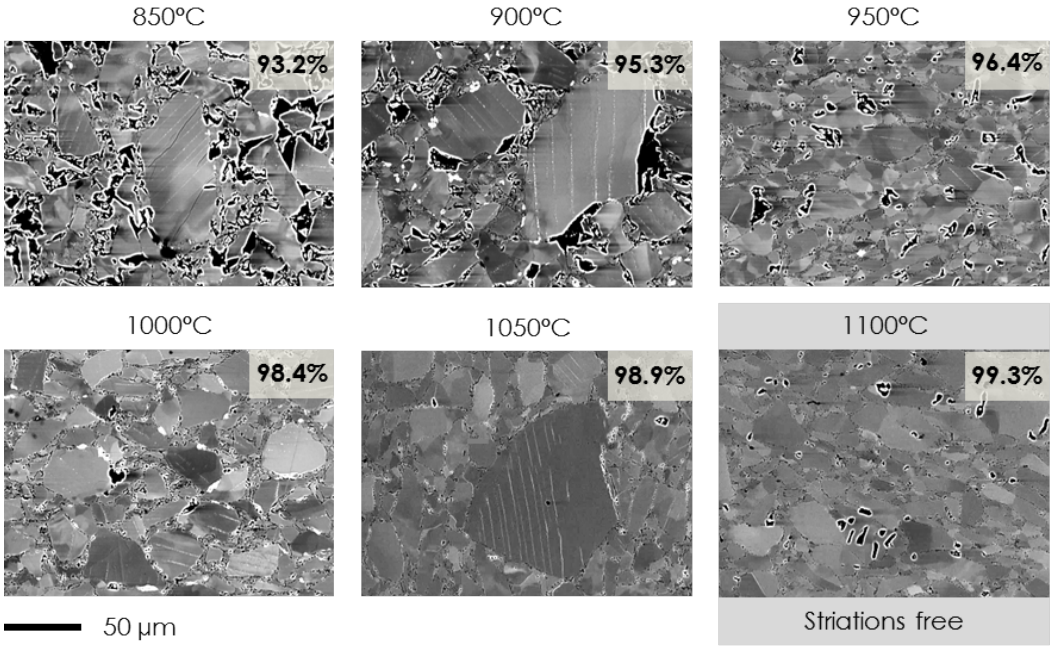

Figure 2.23: *Effect of SPS dwell temperature on the densification of MnSi* $_{1.73}$ *grounded powders. At 1100°C the MnSi striations are removed from HMS matrix. The relative density is calculated from theoretical density of 5.159 for HMS.*

The decrease in porosity content due to the increase of the dwell temperature leads to highest relative density for T=1100°C. In parallel, for this sintering temperature the MnSi striations are removed from HMS matrix.

The refined lattice parameters from profile matching performed on as-SPS material sintered at 1100°C are: a=5.5247(5) Å, c_{Mn}=4.3656(4) Å, c_{Si}=2.5135(5) Å and c-axis ratio γ=1.7368(4). The γ value is consistent with the values previously evidenced and no significant change is observed for cell parameters. A detailed analysis of the diffraction pattern (see figure 2.24) shows that SPS post-processing results in a change in peaks profiles from asymmetric (in the as-cast condition) to symmetric for the main peak of [Si] (1101) and the second one (211-1).

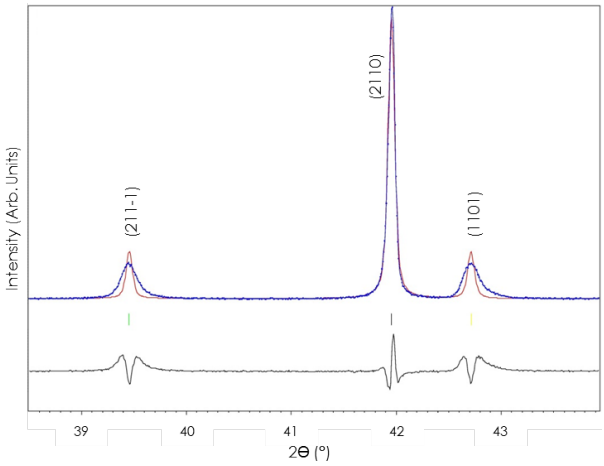

Figure 2.24: *Enlargement in profile matching for as-SPS material sintered at 1100°C were (1101) [Si] peak presents a symmetric profile.*

In addition, the electron diffraction pattern exhibit spacing and orientations anomalies as shown on figure 2.25. A view of the particle where TEM diffraction was performed is presented with the corresponding diffraction pattern. The zone axis is kept as [-120] to compare the material in as-cast and as-SPS states.

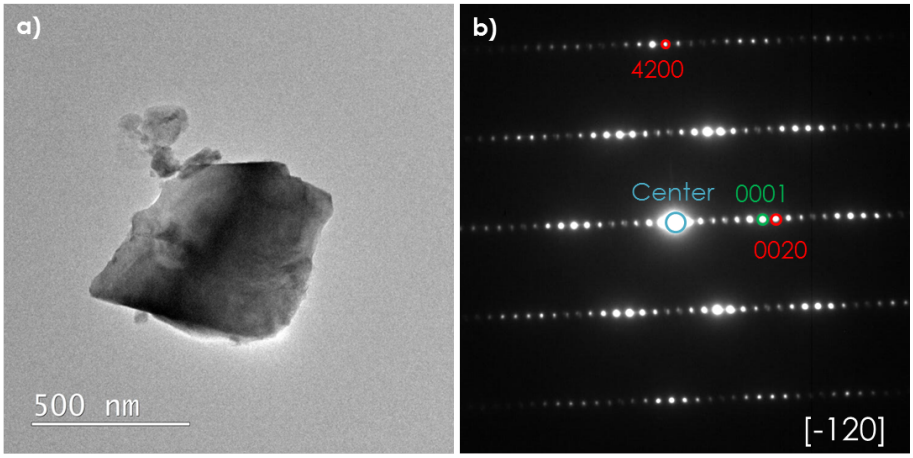

Figure 2.25: *View of the powder of as-SPS material sintered at 1100°C were TEM analysis was performed (a) and the corresponding diffraction pattern (b) taken with [-120] zone axis.*

Thanks to the spot intensities along c-axis extracted from the diffraction patterns we can compare the as-cast and as-SPS materials (see figure 2.26). For the as-SPS state, the sequence of satellites spots associated with different basic spots do not match where they meet. Spacing and orientations

anomalies are observed which indicates that the structure is incommensurate. In light of these facts, it can be stated that after SPS the MnSi striations are removed from HMS matrix leading to an incommensurate HMS phase.

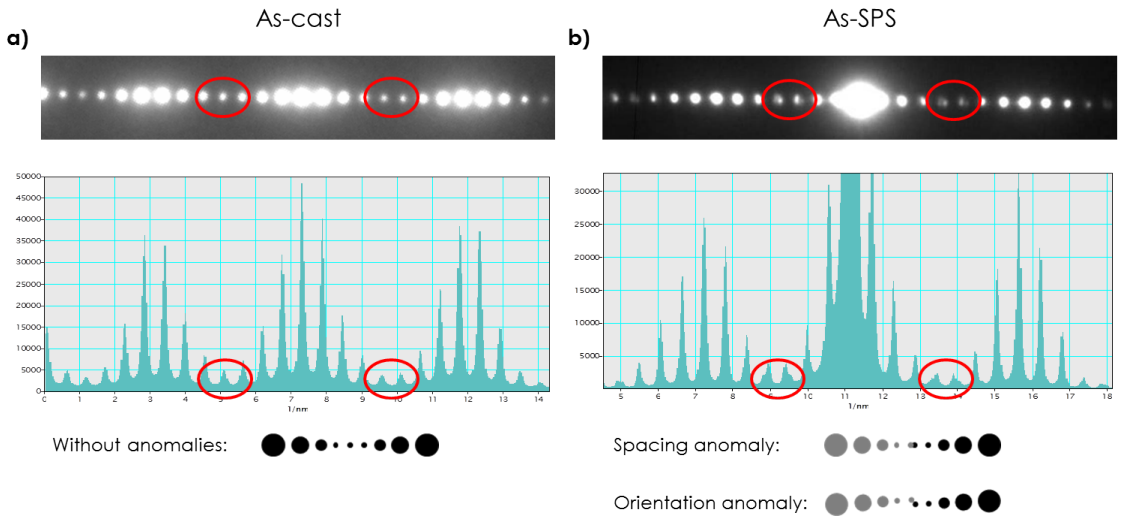

Figure 2.26: *Enlargement of diffraction patterns along c-axis and the corresponding spot intensities for as-cast (a) and as-SPS 1100°C (b) states for* $MnSi_{1.73}$ *alloy.*

After post-processing by SPS at 1100°C casted materials are free of MnSi striations.

From XRD and TEM analysis after SPS the incommensurate character of HMS phase is associated with a change in the [Si] (1101) peak profile from asymmetric broadening for as-cast state to symmetric.

2.2.3 Effect of the micro-substitutions

In this section we sought for a systematic evaluation of the effect of two alloying elements used in the literature as doping elements. Cr and Ge elements are selected to be respectively substituted on the Mn and Si atomic sites of HMS crystal structure; a modification of the periodicity of Mn and Si period is expected.

Since the previous section suggests that there is a causal relationship between the lack/presence of striations and the inco/commensurate character of the HMS phase, the perturbation of the periods with doping elements might affect the microstructure. We sought for a correlation between microstructure and structure.

Synthesis Arc melted materials with Ge (99.99%) chips and Cr (99%) powder respectively provided by Good Fellow CAS [7440-56-4] and by Strem Chemicals CAS [7440-47-3] were obtained through the same process as explained in 1.2.1.

Core-shell duplex microstructure of $Mn(Si,Ge)_{1.73}$

Germanium is evidenced in the literature as a good doping element for HMS. Usually a doping element has an influence on the structure due to substitution, on physical properties (band gap) [25] and can change the nature of the grain boundaries (segregation of the doping element) [26, 27]. In HMS alloys Ge doping was found to affect the MnSi distribution in HMS matrix [28]. Composition $Mn(Si_{0.992}Ge_{0.008})_{1.73}$ is thereafter studied because this composition presents good thermoelectric properties with maximum ZT of 0.6 at 560°C [28].

Figure 2.27 shows the typical microstructure of solidification of this alloy. In addition to the presence of (Si,Ge) secondary phase, one of the most striking feature associated with Ge micro-substitutions is the core/shell microstructure of the HMS grains exhibiting an homogeneous region at the edges and a refined striated region in the center.

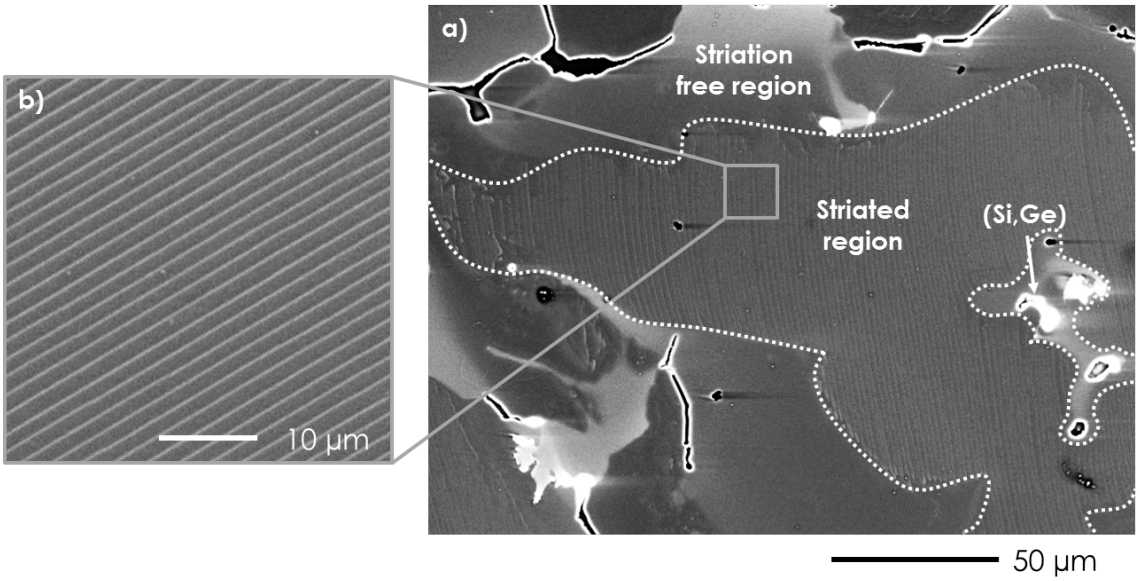

Figure 2.27: *BSE images of $Mn(Si_{0.992}Ge_{0.008})_{1.73}$ as-cast alloy showing the core/shell duplex microstructure of HMS grains (a) and enlargement of the striated region (b).*

EPMA analysis evidence that this duplex microstructure is associated to a gradient of Ge from the center to the edge of each grain. The striation-free region is richer in Ge than the striated region (see

table 2.4).

Composition (at.%)		Mn	Si	Ge
HMS	with striations	36.9	63.0	0.1
	without striations	36.6	63.0	0.4

Table 2.4: *EPMA on HMS phase for* $Mn(Si_{0.992}Ge_{0.008})_{1.73}$ *as-cast alloy. For each zone three points were measured and the average compositions are presented.*

This results suggest that above a concentration threshold of Ge the formation of the MnSi striations is prevented. This was verified with an alloy of nominal composition: $Mn(Si_{0.97}Ge_{0.03})_{1.73}$. The obtained microstructure is presented on figure 2.28 where HMS phase is entirely striation free. It is to note that the (Si,Ge) secondary phase amount increases since Ge amount is higher.

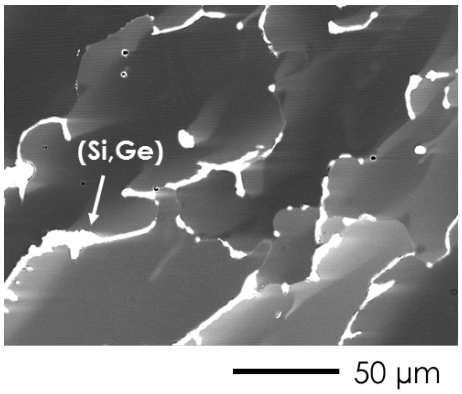

Figure 2.28: *BSE image of* $Mn(Si_{0.97}Ge_{0.03})_{1.73}$ *as-cast alloy showing a complete striation free HMS phase and (Si,Ge) secondary phase.*

The projection of the liquidus surface in the ternary system is calculated along with the solidification paths for the two alloys with 0.8 at.% and 3 at.% of Ge on figure 2.29.a. The projection of the liquidus surface shows the monovariant lines that separate the liquidus surfaces. During the solidification the liquidus composition goes down the liquidus surface, crosses the HMS domain and follows the peritectic line until it reaches the eutectic line which corroborates the structural observations.

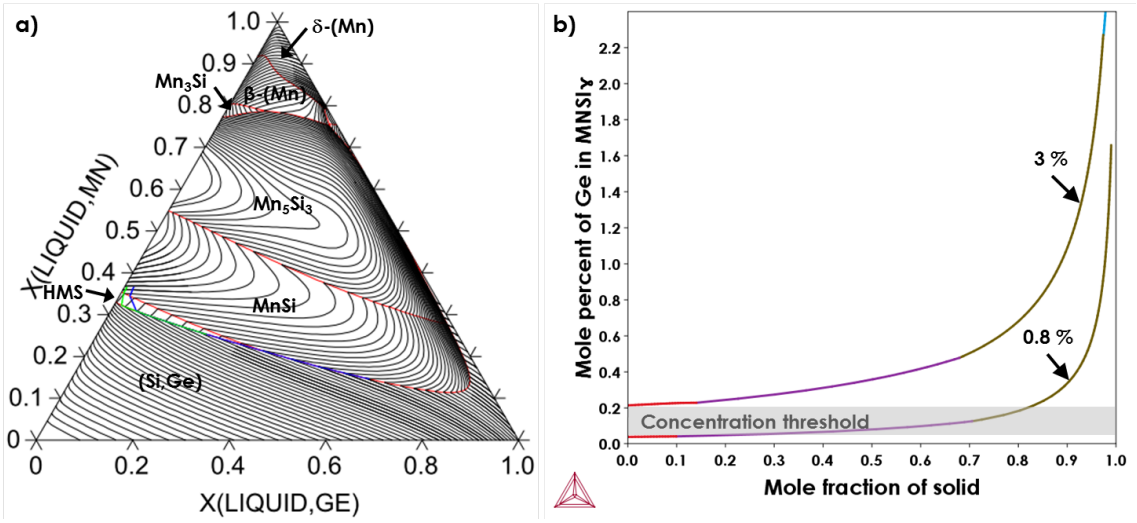

Figure 2.29: *Projection of the liquidus (calculated every 10°C) in the Ge-Mn-Si ternary phase diagram and solidification paths for 0.8 at.% (in green) and 3 at.% (in blue) Ge substitutions (a). Distribution of Ge in HMS phase for 0.8 at.% and 3 at.% Ge substitutions (b) during the solidification showing a concentration threshold.*

Figure 2.29.b. shows the calculated composition changes of the HMS phase as a function of the mole fraction of solids: as the amount of solid increases during the solidification, the Ge concentration in the HMS phase increases too. This phenomena, called micro-segregation, explains the observed concentration gradient inside the HMS grains as evidenced by EPMA. By comparison of the Scheil-Gulliver simulation performed for 0.8 at.% and 3 at.% Ge substitution on Si sites, respectively, we can deduce that the composition threshold above which the formation of the MnSi striations is avoided at about 0.2 at.%.

The core/shell microstructure observed by SEM results in the doubling of the Si peaks on the XRD patterns as shown on figure 2.30. Between 42-43°, two Si peaks are well defined. In order to refine this XRD pattern two HMS phases with different γ values are required. The refined lattice parameters from profile matching are listed in table 2.5.

The first phase (γ~1.72) exhibits a symmetric peak whereas the second one (γ~1.73) exhibits an asymmetric peak. By comparison with an undoped alloy (see figure 2.19), the phase with c-axis ratio value close to γ~1.73 can be attributed to the striated HMS phase, and consequently the peak at γ~1.72 arises from the striation-free zone. This conclusion is further supported by the XRD pattern of $Mn(Si_{0.97}Ge_{0.03})_{1.73}$ alloy which exhibits a single symmetric Si peak between 42-43° (see figure 2.30.b).

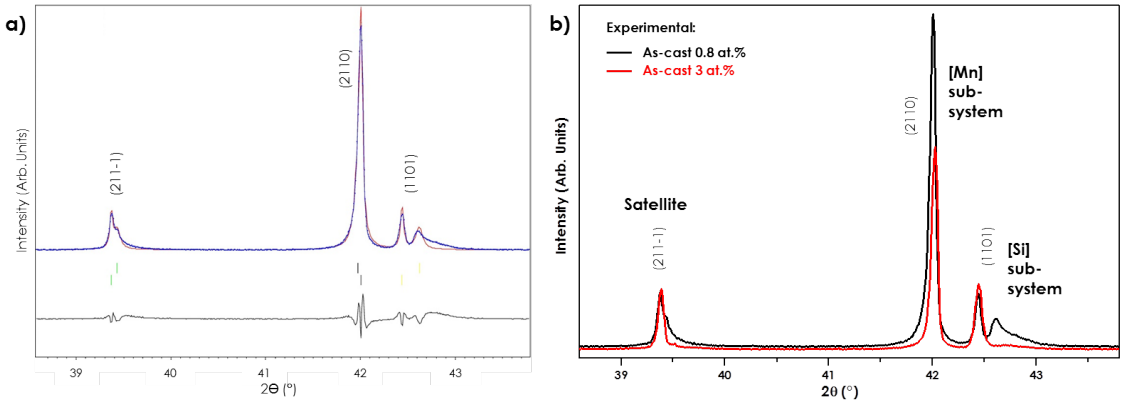

Figure 2.30: *Enlargement in profile matching for* $Mn(Si_{0.992}Ge_{0.008})_{1.73}$ *as-cast alloy (a) and XRD profiles for 0.8 and 3 % at. for* $Mn(Si,Ge)_{1.73}$ *as-cast alloys.*

Nominal composition	**State**	**a (Å)**	$\mathbf{c}_{Mn}$ **(Å)**	$\mathbf{c}_{Si}$ **(Å)**	$\boldsymbol{\gamma}$
$Mn(Si_{0.992}Ge_{0.008})_{1.73}$	As-cast	5.5192(3)	4.3651(7)	2.5380(0)	1.7199(2)
		5.5232(4)	*4.3669(4)*	*2.5228(4)*	*1.7309(6)*
$Mn(Si_{0.97}Ge_{0.03})_{1.73}$	As-cast	5.5200(7)	4.3666(5)	2.5388(8)	1.7199(1)

Table 2.5: *Refined parameters from profile matching for* $Mn(Si_{0.992}Ge_{0.008})_{1.73}$ *and* $Mn(Si_{0.992}Ge_{0.008})_{1.73}$ *as-cast alloys. For* $Mn(Si_{0.992}Ge_{0.008})_{1.73}$ *as-cast alloy two HMS phases are refined due to the core/shell duplex microstructure. The second phase in italic means that this phase is in minority.*

The [-120] HMS electron diffraction pattern observed for the striated region (center of the grain) and for the striation-free region (edge of the grain) evidence a commensurate structure for both regions (see figure 2.31). Facing these results to XRD analysis, we can associate the asymmetric peak ($\gamma \sim 1.73$) to a mixture of commensurate HMS phases as for the undoped alloy (see figure 2.19) and the symmetric peak ($\gamma \sim 1.72$) to a single doped commensurate HMS phase. It is to note that the decrease in satellite spots intensity previously observed for an undoped alloy is not evidenced when Ge atoms are substituted in Si position, which can be attributed to an increase of the periodicity of the Si helices due to the insertion of Ge.

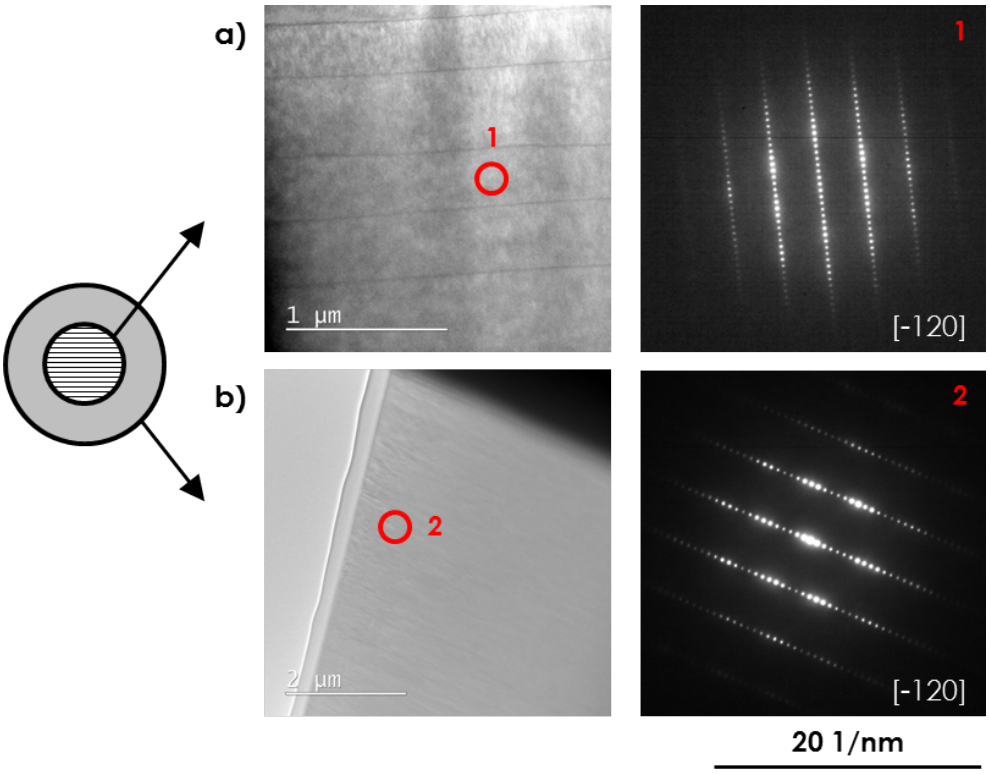

Figure 2.31: *View of the TEM foils and the corresponding diffraction patterns for the striated region (a) and for the striation-free region (b) of HMS for* $Mn(Si_{0.992}Ge_{0.008})_{1.73}$ *as-cast alloy.*

Figure 2.32 presents the lattice parameters variation with micro-substitution rate. As expected from Ge substitution on Si sites c_{Mn} parameter is not affected. In parallel, c_{Si} increases with the substitution rate whereas a parameter follows the opposite trend. Ge insertion in the crystal structure leads to an extension in c direction associated to a shrinkage in a direction. Above 0.8 at.% no further increase (decrease) is observed for c_{Si} (for a) parameter showing the limit of solubility of Ge. This finding is important with respect to the thermoelectric properties because it shows that above 0.8 at.%, an increase of Ge will not lead to an increase of the doping but will results to the formation of a larger amount of (Si,Ge) secondary phase. This is the reason why thermoelectric properties will be measured on 0.8 at.% Ge substituted alloy in chapter 4.

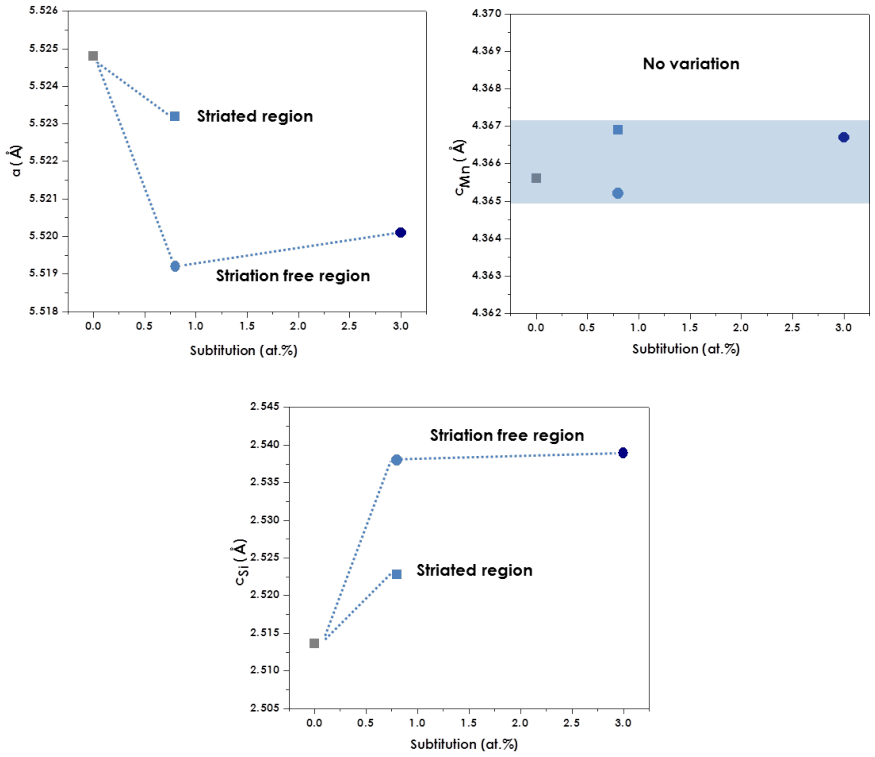

Figure 2.32: *Evolution of the lattice parameters a, c_{Mn} and c_{Si} for $Mn(Si_{1-x}Ge_x)_{1.73}$ as-cast alloys with x=0, 0.8 and 3 at.%. The striated HMS phase is reported with squares and the HMS striation free region with circles.*

The formation of the secondary phase and the Ge gradient is consistent with combined XRD, TEM, EMPA and Scheil-Gulliver analysis.

The duplex core/shell microstructure of the $Mn(Si_{0.992}Ge_{0.008})_{1.73}$ alloy results from Ge micro-segregation:

- striated region: mixture of undoped commensurate HMS phases
- striation free region: single Ge-doped commensurate HMS phase

Effect of thermal treatments and spark plasma sintering on the microstructure of $Mn(Si_{0.992},Ge_{0.008})_{1.73}$

Herein, we present the microstructure evolution of the $Mn(Si_{0.992}Ge_{0.008})_{1.73}$ alloy during annealing at 1000°C (see figure 2.33) and sintering (see figure 2.36), respectively.

Figure 2.33 shows the rapid changes that occurs during annealing at 1000°C. First, we observe a

change in the shape of the MnSi phase from platelet (striations) to spheres. This process of spheroidization occurs very rapidly (after 1h at 1000°C) and is followed by the complete dissolution of MnSi striations after 1 day at the same temperature. It is important to note that the situation was totally different for undoped alloys (see figure 2.17) for which we observed the thermal stability of the MnSi striations up to 43 days at 1000°C. Since we have previously evidenced that an increase of the Ge content above a concentration threshold of 0.2 at.% prevents the formation of MnSi striations, we can attribute their complete dissolution after annealing as the result of the homogenization of the Ge concentration. This assumption is corroborated by EPMA analysis (see table 2.6). This would imply a diffusion coefficient of 10^{-14} m^2/s for Ge atoms.

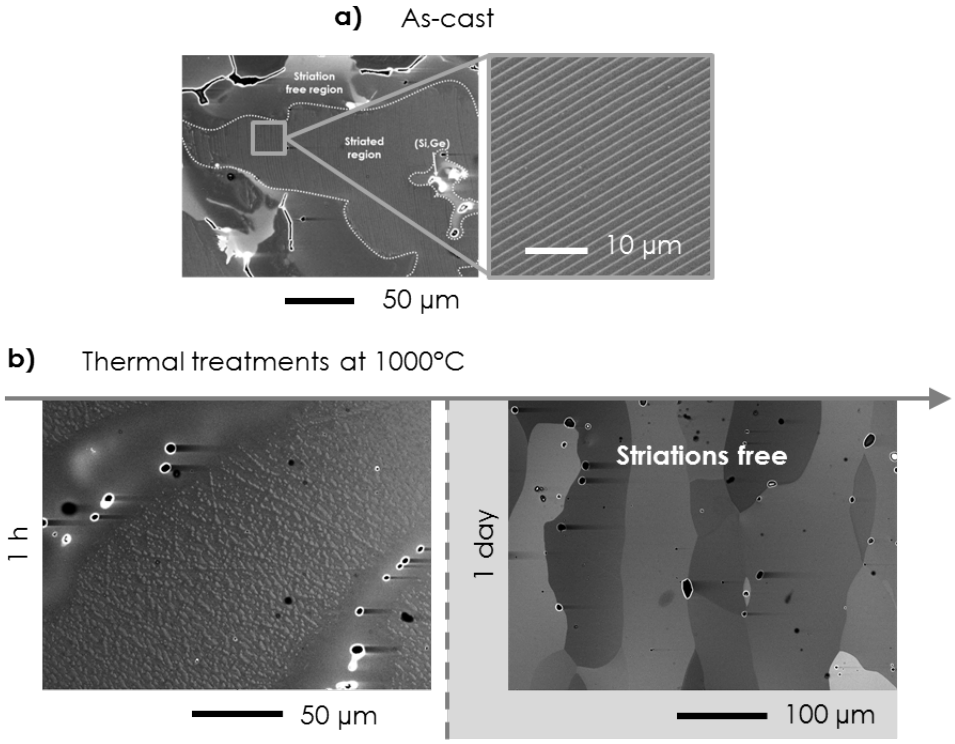

Figure 2.33: *BSE images of as-cast (a) and thermal treated* $Mn(Si_{0.992}Ge_{0.008})_{1.73}$ *alloys at 1100°C during: 1 h and 1 day (b).*

Composition (at.%)		Mn	Si	Ge
As-cast	with striations	36.9	63.0	0.1
	without striations	36.6	63.0	0.4
Annealed at 1000°C	without striations	37.2	62.4	0.4
As-SPS at 1100°C	without striations	36.9	62.7	0.4

Table 2.6: *EPMA on $Mn(Si_{0.992}Ge_{0.008})_{1.73}$ alloys before and post-processing showing that both As-SPS and annealed materials are leading to a single doped striation free HMS phase.*

Figure 2.34.a. shows the experimental XRD patterns for the $Mn(Si_{0.992}Ge_{0.008})_{1.73}$ alloy in the as-cast state and after annealing at 1000°C during 1h and 43 days. The microstructure of the alloys annealed during 43 days at 1000°C is similar to what is obtained after 1 day. The refined lattice parameters are recapitulated in table 2.7. When annealing time increases, the peak associated with the $\gamma \sim 1.72$ phase increases (homogenous doped HMS) while the peak corresponding to the $\gamma \sim 1.73$ phase (striated HMS) progressively disappears. We can observe that the peak corresponding to $\gamma \sim 1.72$ is symmetric which is associated with the formation of an incommensurate HMS phase as evidenced on the electron diffraction pattern shown on figure 2.35.

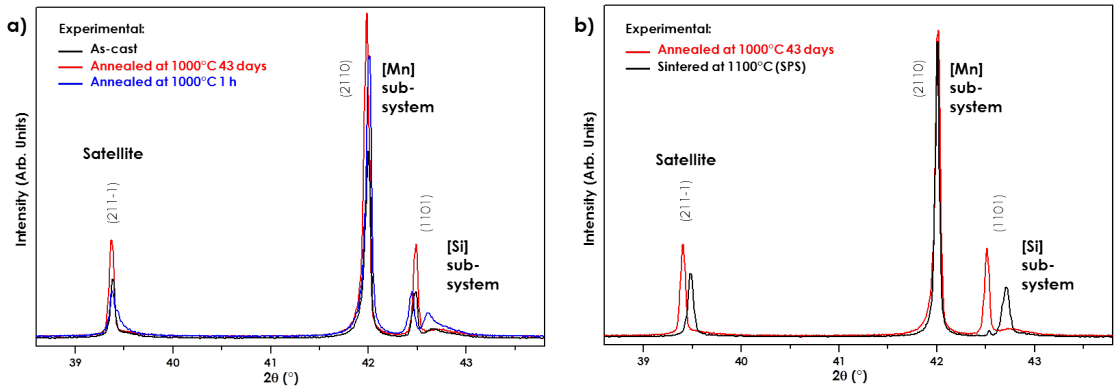

Figure 2.34: *Evolution of the XRD profiles with annealing time for $Mn(Si_{0.992}Ge_{0.008})_{1.73}$ alloys showing the transformation of HMS duplex microstructure to homogeneous one (a). Comparison of XRD profiles for $Mn(Si_{0.992}Ge_{0.008})_{1.73}$ alloys after post-processing (b) leading to two different γ values.*

Nominal composition	State	a (Å)	c_{Mn} (Å)	c_{Si} (Å)	γ
$Mn(Si_{0.992}Ge_{0.008})_{1.73}$	As-cast	5.5192(3)	4.3651(7)	2.5380(0)	1.7199(2)
		5.5232(4)	*4.3669(4)*	*2.5228(4)*	*1.7309(6)*
$Mn(Si_{0.992}Ge_{0.008})_{1.73}$	Annealed at 1000°C 43 days	5.5205(0)	4.3658(1)	2.5327(9)	1.7237(1)
$Mn(Si_{0.992}Ge_{0.008})_{1.73}$	Annealed at 1000°C 1 h	5.5199(1)	4.3653(1)	2.5344(6)	1.7223(8)
		5.5259(3)	*4.3680(5)*	*2.5152(7)*	*1.7366(1)*
$Mn(Si_{0.992}Ge_{0.008})_{1.73}$	As-SPS 1100°C	5.5256(4)	4.3671(6)	2.5179(2)	1.7344(3)

Table 2.7: *Refined parameters from profile matching for $Mn(Si_{0.992}Ge_{0.008})_{1.73}$ alloys before and post-processing. The second phase in italic means that this phase is in minority.*

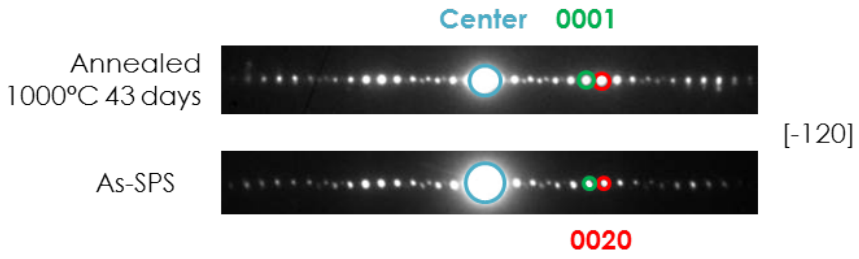

Figure 2.35: *Diffraction pattern from TEM analysis for annealed 1000°C 43 days (a) and as-SPS (b) $Mn(Si_{0.992}Ge_{0.008})_{1.73}$ alloys.*

Sintering by SPS leads to the total disappearance of the striations and the homogenization of the microstructure and Ge content, but surprisingly the sintered sample (as-SPS) exhibits XRD and electron diffraction patterns slight different compared to the annealed: it has a single and symmetric Si peak between 42-43° and spot anomalies but the γ value is about 1.73 as observed for the undoped alloy. So, despite the same Ge substitution rate, different processing routes lead to the stabilization of different HMS phases.

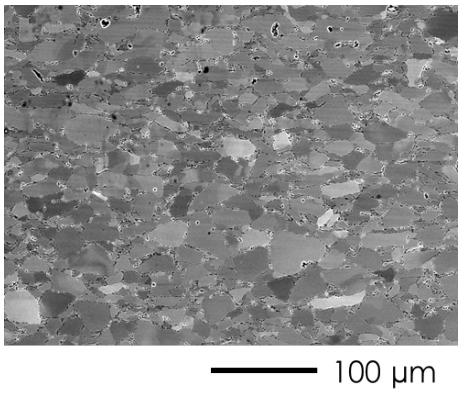

Figure 2.36: *BSE images of as-SPS material sintered at 1100°C for* $Mn(Si_{0.992}Ge_{0.008})_{1.73}$ *alloy.*

At 1000°C the MnSi striations are removed in HMS phase leading to an homogenous HMS microstructure.

Both post-processed materials present a symmetric peak on XRD patterns and anomalies in electron diffraction patterns associated to an incommensurate homogeneous doped HMS phase. However, the c-axis ratio stabilized is post-processed dependent:

- $\gamma \sim 1.72$ for annealed state
- $\gamma \sim 1.73$ for as-SPS state

Random duplex microstructure of (Mn,Cr)$Si_{1.73}$

Two compositions are thereafter studied to highlight the Cr micro-substitution effect on HMS phase: $(Mn_{0.995}Cr_{0.005})Si_{1.73}$ and $(Mn_{0.97}Cr_{0.03})Si_{1.73}$ (see figure 2.37). For the 0.5 at.% as-cast alloy we observe no change compared to the undoped alloy: MnSi striations are homogeneously distributed in all the HMS grains. For the 3 at.% as-cast alloy a perturbation of the MnSi striations is observed but contrary to Ge effect the perturbation is not associated to the grain shape: from center to edge. In this case the MnSi striations are randomly distributed in HMS phase as showed on figure 2.37.c.

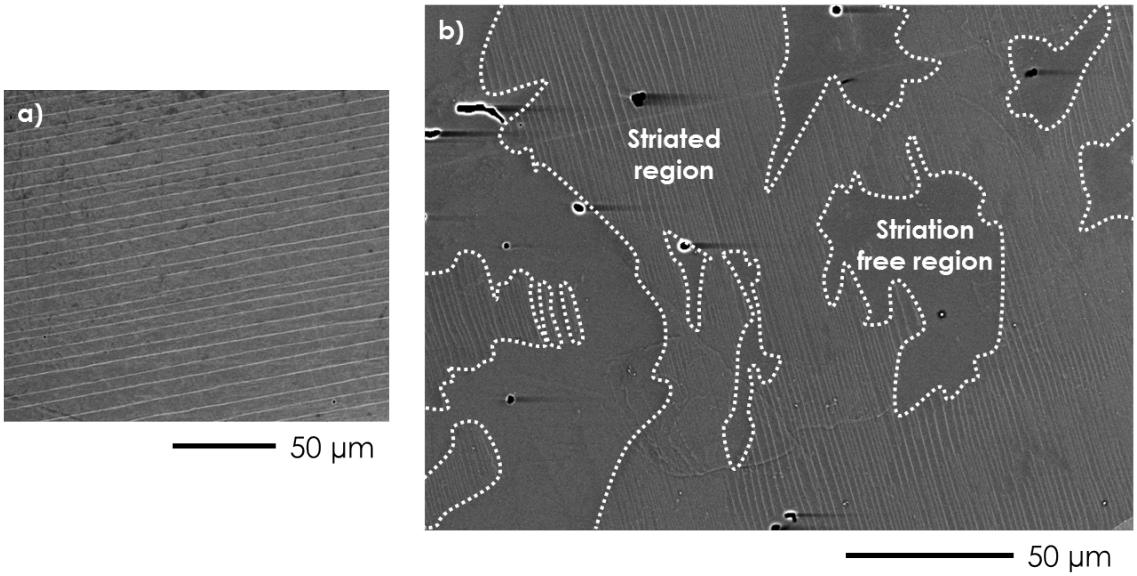

Figure 2.37: *BSE images of* $(Mn_{0.995}Cr_{0.005})Si_{1.73}$ *(a) and* $(Mn_{0.97}Cr_{0.03})Si_{1.73}$ *(b) as-cast showing a random duplex microstructure when Cr content is increased.*

EPMA analysis confirms that the two regions are associated to different Cr content, similar to what was previously discussed for the Ge (see table 2.8).

Composition (at.%)		Mn	Cr	Si
0.5 at%	with striations	35.1	0.2	64.7
3 at.%	with striations	34.5	0.7	64.8
	without striations	33.6	1.5	64.9

Table 2.8: EPMA on HMS phase for $(Mn_{0.995}Cr_{0.005})Si_{1.73}$ *and* $(Mn_{0.97}Cr_{0.03})Si_{1.73}$ *as-cast alloys. For each zone three points were measured and the average compositions are presented.*

From XRD profile matching performed on the 3 at.% as-cast alloy we confirm the coexistence of two HMS phases (see figure 2.38 and table 2.9) corresponding to the two microstructural states of HMS phase.

Nominal composition	State	a (Å)	c_{Mn} (Å)	c_{Si} (Å)	γ
$(Mn_{0.995}Cr_{0.005})Si_{1.73}$	As-cast	5.5230(8)	4.3644(2)	2.5173(6)	1.7337(2)
$(Mn_{0.97}Cr_{0.03})Si_{1.73}$	As-cast	*5.5237(1)*	*4.3681(1)*	*2.5320(6)*	*1.7251(2)*
		5.5273(3)	4.3696(1)	2.5192(6)	1.7344(8)

Table 2.9: *Refined parameters from profile matching for $(Mn_{0.995}Cr_{0.005})Si_{1.73}$ and $(Mn_{0.97}Cr_{0.03})Si_{1.73}$ as-cast alloys. For $(Mn_{0.97}Cr_{0.03})Si_{1.73}$ as-cast alloy two HMS phases are refined due to the random duplex microstructure. The second phase in italic means that this phase is in minority.*

In addition, XRD profiles between 0.5 at.% to 3 at.% highlight the microstructural change from fully striated HMS to duplex microstructure. According to what was stated for Ge micro-substitution the two regions evidenced for $(Mn_{0.97}Cr_{0.03})Si_{1.73}$ alloy can be attributed to two different HMS phases: commensurate doped ($\gamma \sim 1.72$ symmetric peak) and commensurate undoped ($\gamma \sim 1.73$ asymmetric peak) (see figure 2.38).

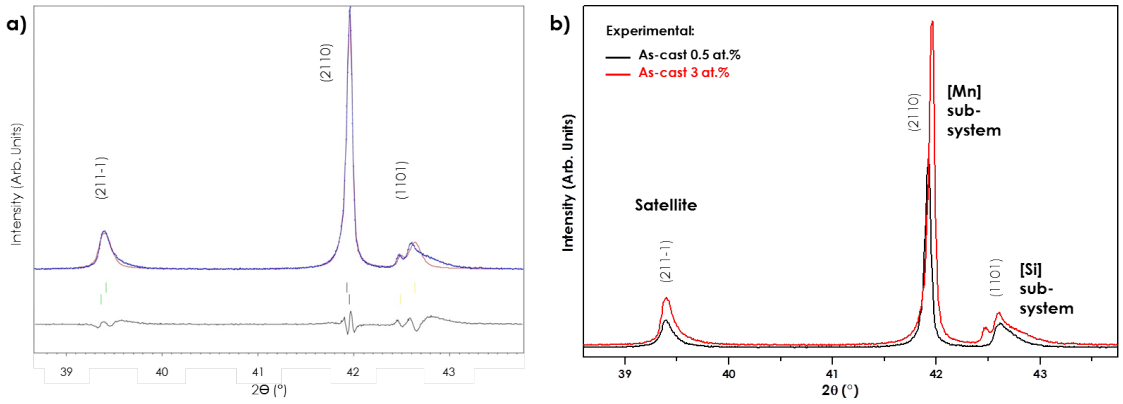

Figure 2.38: *Enlargement in profile matching for $(Mn_{0.97}Cr_{0.03})Si_{1.73}$ as-cast alloy (a) and profiles for 0.5 and 3 at.% of Cr for as-cast alloys. Change from striated to duplex is evidenced.*

Cr micro-substitution on Mn position has an important effect on the microstructure of arc-melted HMS alloys.

Contrary to what is found for Ge, a random duplex microstructure is evidenced with Cr.

For Cr microsubstitution it is necessary increase the amount of Cr to observe a concentration threshold and thus the duplex microstructure.

Duplex microstructures interpretation

We evidenced experimentally that the micro-substitutions of Ge on Si sites and Cr on Mn sites are leading to the same effects: the progressive disappearance of the MnSi striations and to the formation of an HMS phase with $\gamma \sim 1.72$. However, we can notice two differences in the concentration threshold and on the duplex microstructures morphologies. We showed that the core/shell duplex microstructure obtained for Ge was due to the micro-segregation effect, in others words due to an enrichment of Ge afront of the moving liquid/solid interface during the solidification. As shown on figure 2.39 the situation differs for Cr micro-substitution. In this case, we observe a decrease of the Cr concentration of the liquidus and of the HMS phase upon cooling. The different behaviors observed for Ge and Cr are due to the high solubility of Cr in MnSi phase (see figure 2.40). As a consequence most of the Cr is incorporated in the MnSi phase leading to depleted liquidus and HMS phases. These results are supported by EMPA analysis where Cr concentration in the striation free region increases with the substitution content whereas for Ge micro-substitution this value is stable with respect to the substitution (see tables 2.4 and 2.8).

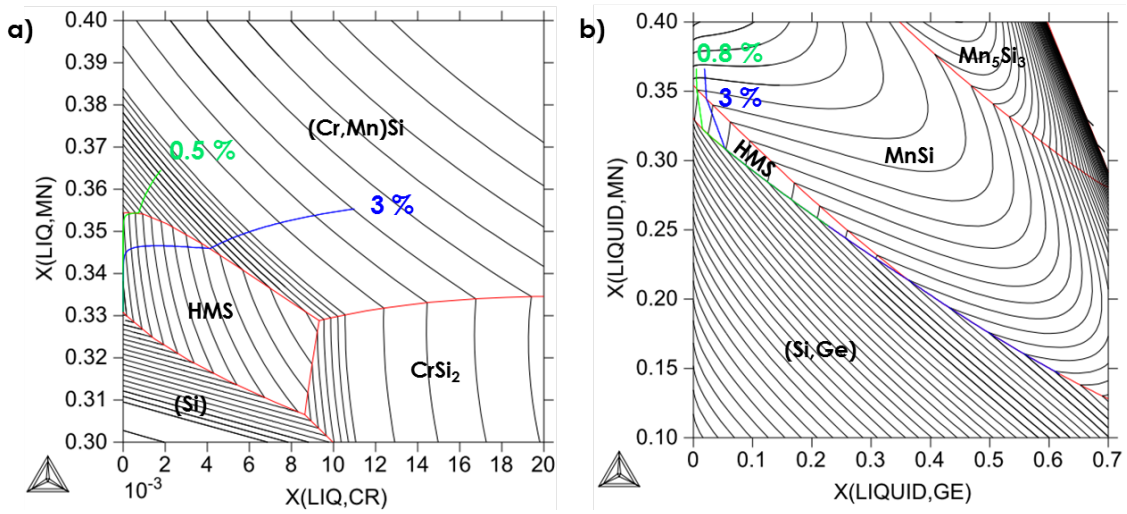

Figure 2.39: *Projection of the liquidus (calculated every 20°C) in the Cr-Mn-Si ternary phase diagram and solidification paths for 0.5 at.% (in green) and 3 at.% (in blue) alloys (a). Projection of the liquidus in the Ge-Mn-Si ternary phase diagram and solidification paths for 0.5 at.% (in green) and 3 at.% (in blue) alloys (b).*

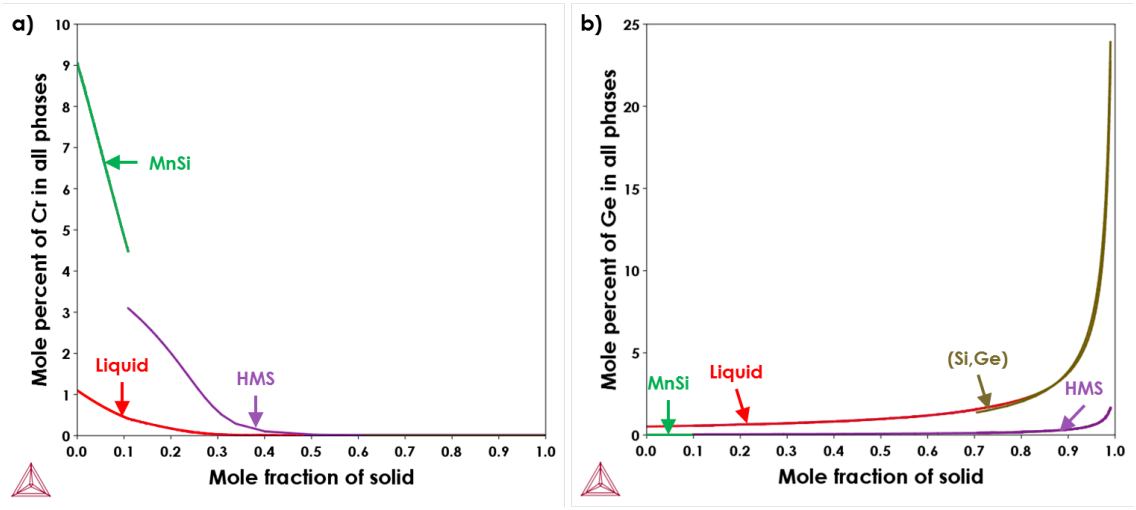

Figure 2.40: *Distribution of Cr (a) and Ge (b) in the phases (Liquid, MnSi, HMS and (Si,Ge)) during the solidification for* $(Mn_{0.97}Cr_{0.03})Si_{1.73}$ *and* $Mn(Si_{0.992}Ge_{0.008})_{1.73}$ *as-cast alloy, respectively.*

The different microstructural features associated with Ge and Cr duplex microstructures are consistent with Scheil-Gulliver simulation.

2.3 Discussion

The investigations by XRD and electron diffraction we have performed on solidified and sintered HMS phases have revealed the intriguing nature of this NCL compound which can exist either as (i) a mixture of commensurate composite crystals which slightly differ in composition but are structurally closely related, or (ii) a single incommensurate modulated phase.

We have evidenced that the commensurate phases result from solidification while the commensurate-incommensurate transition occurs during sintering by SPS. We have also observed that commensurate phases are separated by amorphous regions (so-called MnSi striations). Finally, shown on figure 2.41 are the composition (x values) of the HMS phases, determined from XRD analysis as a function of the temperature and the nominal alloy composition, reported in the calculated Mn-Si phase diagram along with the results from the literature. We can note a continuous composition shift with temperature changes and a narrow homogeneity range. These observations differ from the interpretation proposed by Allam *et al.* [29] and Kikuchi *et al.* [18] who assumed a step-wise succession of two line-compounds (first-order phase transition). We do not agree either with the assumption of Berche *et al.* [1] who describe the HMS phase as a solid solution to explain the homogeneity range whereas our results suggest

the coexistence of multiple discrete and fully ordered structures.

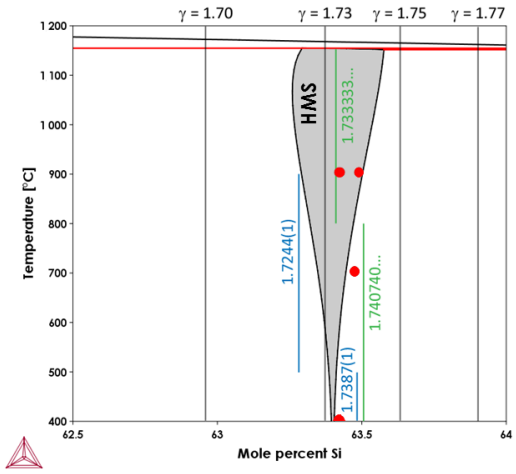

Figure 2.41: *Mn-Si binary phase diagram close to HMS phase field from CALPHAD assessment from Berche et al. [1] (in gray) and experimental phase transformations from Allam et al. [29] (in green) and from Kikuchi et al. [18] (in blue). Our experimental points for the four nominal compositions (γ=1.70, 1.73, 1.75 and 1.77) as-cast and equilibrated at 700°C and 900°C are reported (in red).*

This situation can be recognized as infinitely adaptive structures [30] for which every composition orders into a superlattice which can accommodate subtle changes in composition by a change in the number of its sub-units. This situation has been rationalized by a model introduced by McMillan [31] in which an array of atoms connected with harmonic springs interacts with a periodic potential. The potential modulates the chain and if it is strong enough, it can lock the chain into commensurate structures. By analogy, for HMS, it is the ability of the Si helices to adjust to an almost continuous series of Mn/Si ratio that leads to the existence of a large number of commensurate phase. With this scheme, the MnSi striations can be understood as walls separating two different commensurate regions, and the effects of Ge and Cr micro-substitutions as the result of perturbations of the Si helices and the Mn periodic potential, respectively. It is also to note that the locking into commensurate phases occurs only during solidification, and that additional post-processing in the solid state induce the formation of an incommensurate structure. Adopting the designation of Aubry [32], it appears that the "devil's staircase" – leading to the formation of consecutive commensurate phases (with different periods) as a function of temperature – takes place between the peritectic and the eutectic invariant reaction. These ideas are supported by three additional sets of experiments. The first one is the no-effect of elements that cannot enter in the [Mn] or [Si] sub-systems. This is for example the case for La and W. As shown in figure 2.42, additions of these elements in various amounts do not change the density

number of the MnSi striations, whereas substitution on Mn sites by Cr or on Si sites by Ge leaded to a tremendous enhancement of the MnSi striations number and their total disappearance above a concentration threshold.

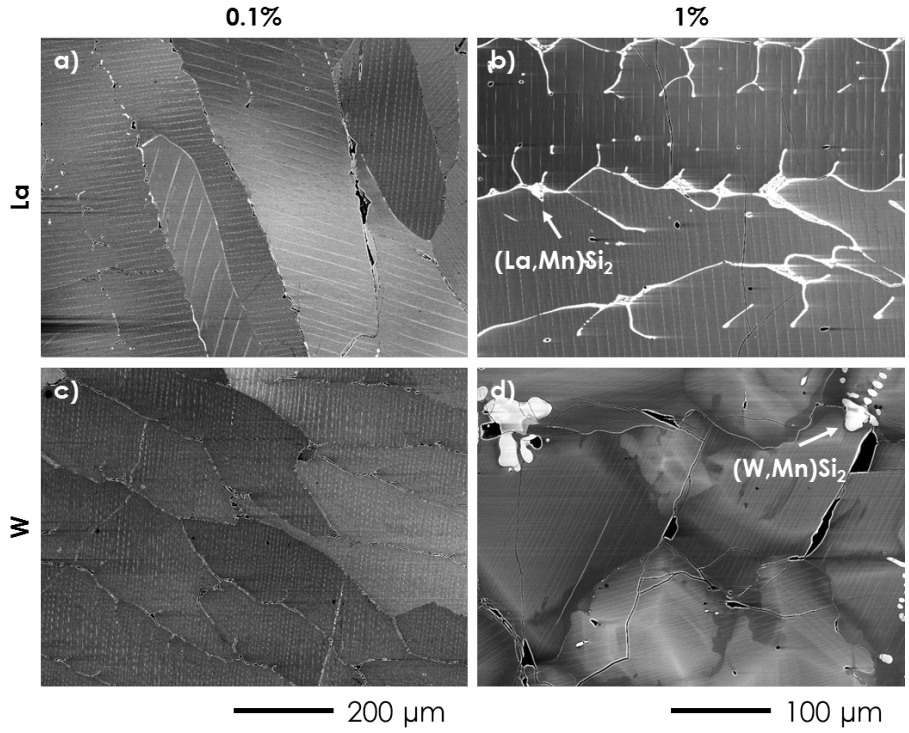

Figure 2.42: *BSE images for $MnSi_{1.73}X_{0.001}$ and $MnSi_{1.73}X_{0.1}$ as-cast alloys for X=La (a,b) and for X=W (c,d) showing a typical striated HMS phase. The increase in X elements is leading to an increase of the secondary phases: (La,Mn)Si_2 and (W,Mn)Si_2 without disturbing the distribution of the MnSi striations.*

The second confirmation is provided by the striation-free microstructure obtained for a solidified eutectic composition (see figure 2.43). In such alloy, the HMS phase is incommensurate (see figure 2.44) and do not present any MnSi striations.

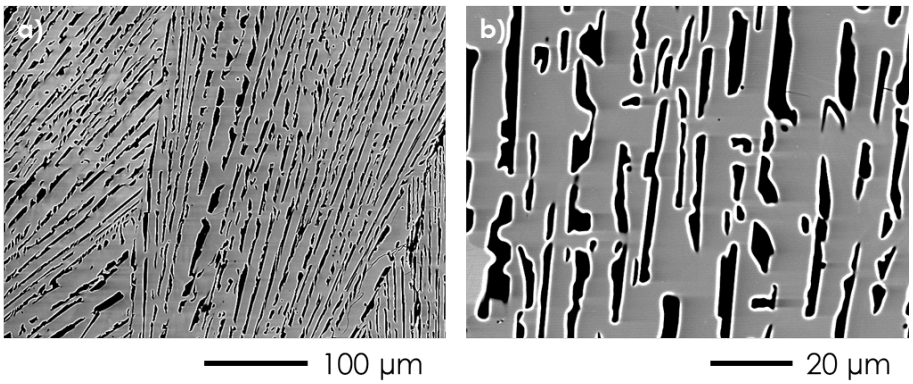

Figure 2.43: *BSE images of as-cast $Mn_{32}Si_{68}$ alloy (a) and enlargement (b).*

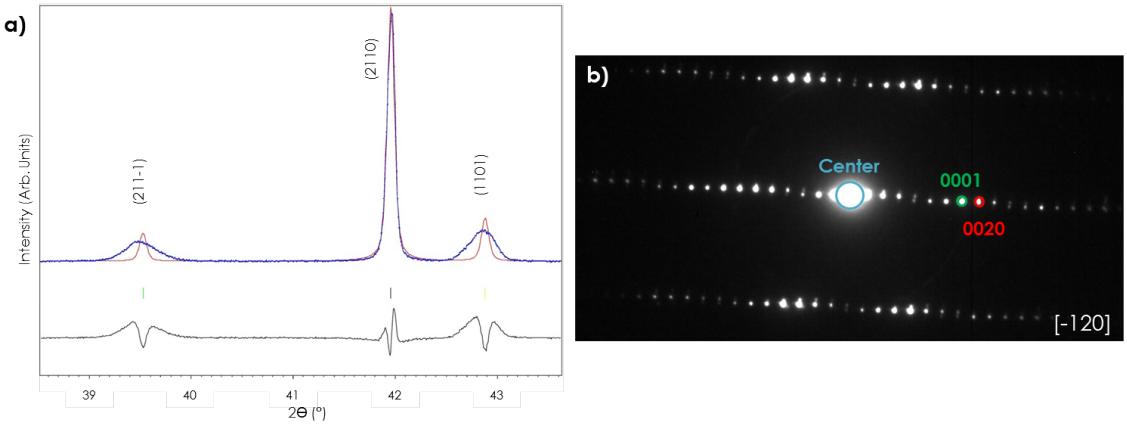

Figure 2.44: *Enlargement in profile matching showing symmetric profile (a) and diffraction pattern from TEM analysis on powder with [-120] zone axis (b) for as-cast $Mn_{32}Si_{68}$ alloy. Looking at the corresponding XRD pattern on we can see that the [Si] (1101) peak presents symmetric profile. The refined lattice parameters from profile matching are: a=5.5271(1) Å, c_{Mn}=4.3654(6) Å, c_{Si}=2.5012(2) Å and c-axis ratio γ=1.7453(3). From TEM analysis is performed the incommensurate character is confirmed.*

The third evidence arises from diffusion couple experiments between Si and MnSi (see figures 2.45 and 2.46). As shown on the SEM image and the EPMA composition profile across the diffusion couple, the interdiffusion zone consists of a single HMS phase with composition corresponding to γ=1.7 and lacking of MnSi striations. This result further confirms that the formation of commensurate phases and the concomitant MnSi walls (striations) result exclusively from solidification.

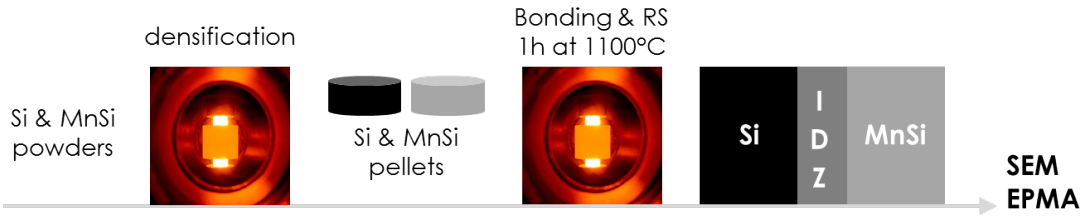

Figure 2.45: *Experimental procedure for diffusion couple experiment. MnSi ingot and pure Si were ground in a mortar to obtain powders that were sieved up to 40 µm. After this step, both MnSi and Si powders were densified by SPS at 1100°C and 1300°C respectively for 10 min under 100 MPa and under vacuum. The two Si and MnSi pellets were metallographically polished and placed in a graphite mold in order to perform the bonding by SPS. The solid state diffusion activated by SPS process was performed at 1100°C under 40 MPa during 1 h in order to create an Inter-Diffusion Zone (IDZ) between the two block halves.*

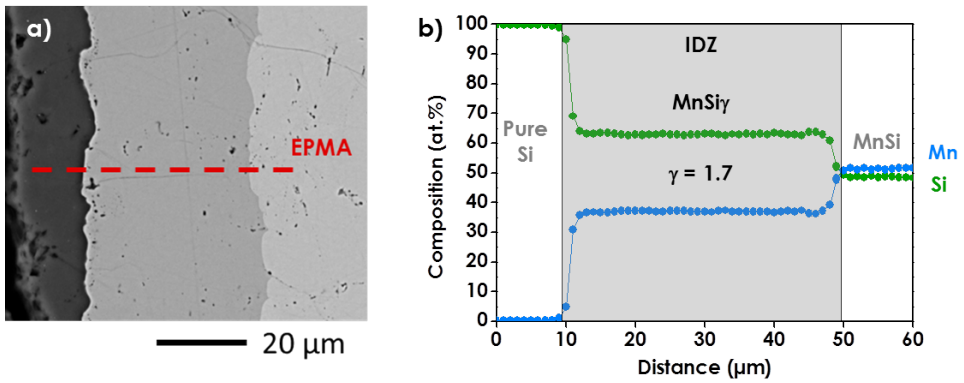

Figure 2.46: *BSE image of Si/MnSi diffusion couple (a) and composition profiles of Si and Mn across the IDZ showed on SEM image by the red dash line (b).*

Figure 2.47 summarizes the importance of the processing route and substitution on the microstructural highlights of HMS, i.e. its commensurability and the presence of MnSi striations. We have evidenced that the occurrence of MnSi striations is related to the formation of a mixture of commensurate phases during solidification, whereas the absence of striations denote the formation of a single doped commensurate structure. The commensurate-incommensurate transition can be induced by post-processing (SPS or thermal treatments) or alloying (micro-substitution). Moreover, as demonstrated by diffusion couple experiments, the formation of an incommensurate structure is favored when the liquid phase is not involved during the synthesis of HMS. This result suggests a new synthesis route for HMS via a solid state reaction, i.e. reactive sintering between Si and MnSi powders, that will be explored hereafter.

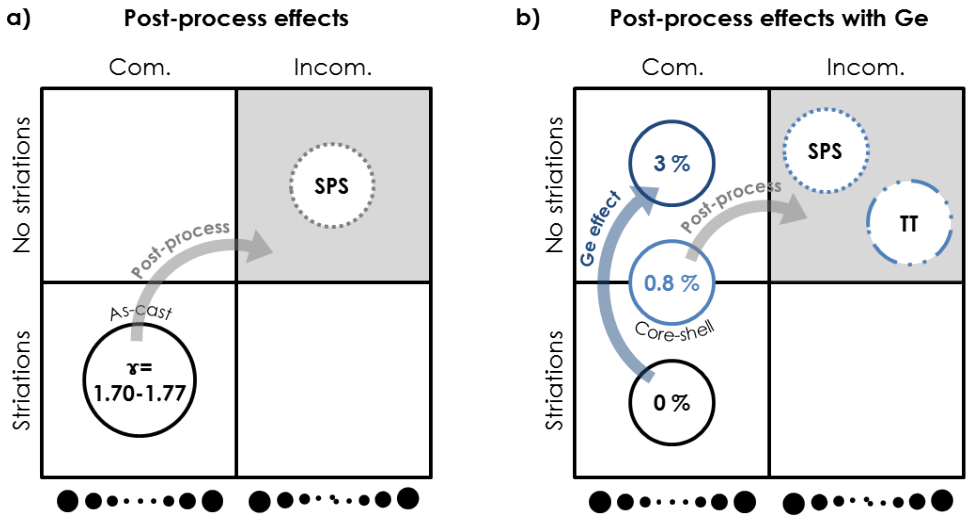

Figure 2.47: *Maps facing the microstructural and structural parameters evolution with the post-processing (a) and with Ge micro-substitution (b). Com. and Incom. abbreviations are used to designate commensurate and incommensurate character.*

2.4 Innovative processing route for HMS-based materials

Experimental procedure The idea is to mix Si and MnSi powders in appropriate amount (nominal composition 1.73) in order to create HMS bulk pellets after SPS: the synthesis and consolidation of HMS will be done in one-single step avoiding the formation of any secondary phases. Prior to reactive sintering both powders were mixed in an agate mortar during 5 min to ensure an homogeneous mix. In order to rule out a possible influence of the SPS, Natural Sintering (NS) is achieved in order to compare HMS characteristics. The two procedures are presented in figure 2.48. The natural sintering of the pellet formed by a mix of cold pressed Si and MnSi powders is done in a Tantalum tube sealed under Argon atmosphere that is then placed in a quartz tube sealed under vacuum for thermal treatment.

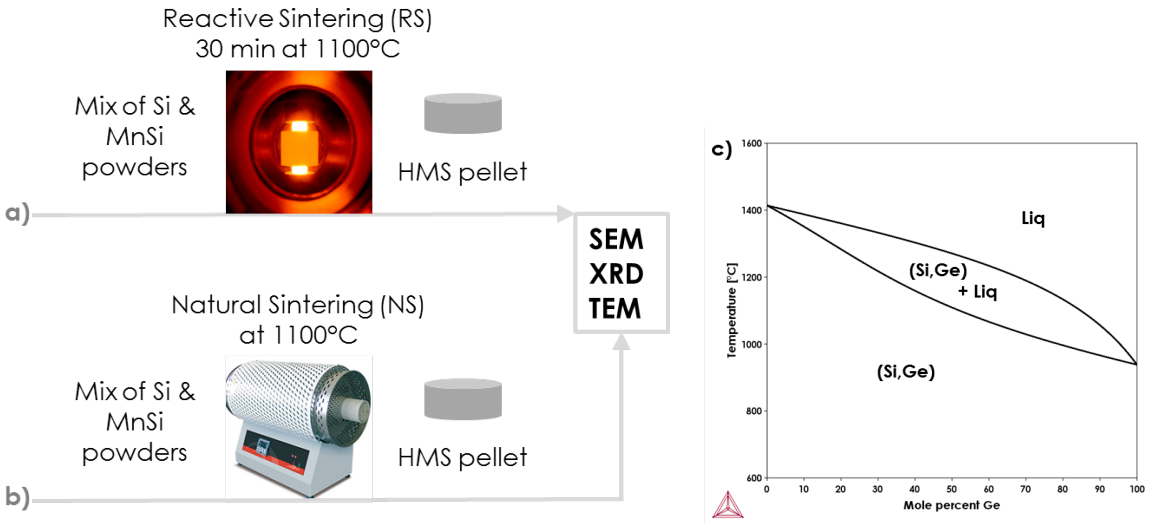

Figure 2.48: *Experimental procedures for reactive sintering (RS) (a) and natural sintering (NS) (b). Binary phase diagram Si-Ge showing a continuous solid solution between Si and Ge elements (c).*

From the Si-Ge binary phase diagram presented on figure 2.48.c. we can see a continuous solid solution between Si and Ge elements. This allow the study of RS doped samples with Ge, the synthesis of such materials was achieved by mixing MnSi and (Si,Ge) powders in appropriate amounts. The (Si,Ge) composition is fixed depending on the desired Ge nominal composition.

Figure 2.49 shows the obtained microstructures after reactive sintering that exhibit low porosity (confirmed by a relative density measured by Archimedes principle of 99.5%) and single phase HMS without any striations. For the Ge-doped sample it is to note that some MnSi primary particles are evidenced due to incomplete reaction.

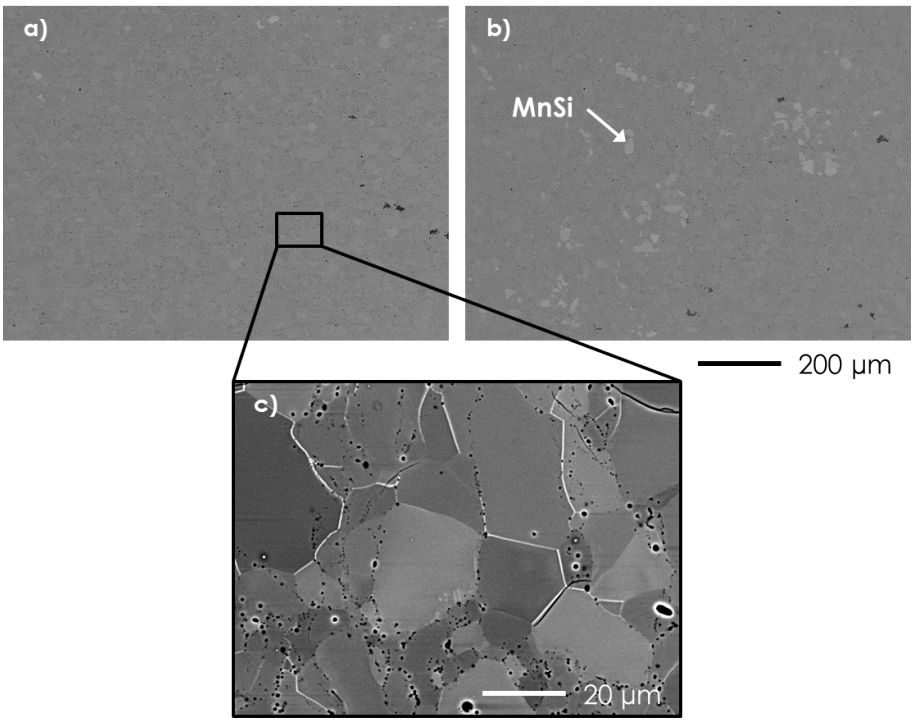

Figure 2.49: *BSE images of reactive sintered alloys: undoped (a,c) and Ge-doped (b).*

The microstructure of the natural sintered sample is shown on figure 2.50.a. where we can see that the formation of the HMS phase is achieved (even if Si and MnSi primarily particles that didn't react are still present in the sample). As the sintering is pressure free the microstructure presents a large amount of porosity. However, since HMS phase is created it is possible to check the lack of MnSi striations in the HMS phase for this sample (see figure 2.50.b.).

Table 2.10 and figure 2.51 presents the XRD analysis for the three studied alloys.

The value of c-axis ratio γ found is in similar to as-SPS alloys issued from liquid-phase process. In addition, symmetric peaks are evidenced on the XRD profiles suggesting an incommensurate character of these alloys.

For the Ge-doped sample obtained via reactive sintering the Ge concentration from EMPA analysis is found to be the same as a doped alloy obtained through liquid-phase process (see figure 2.11).

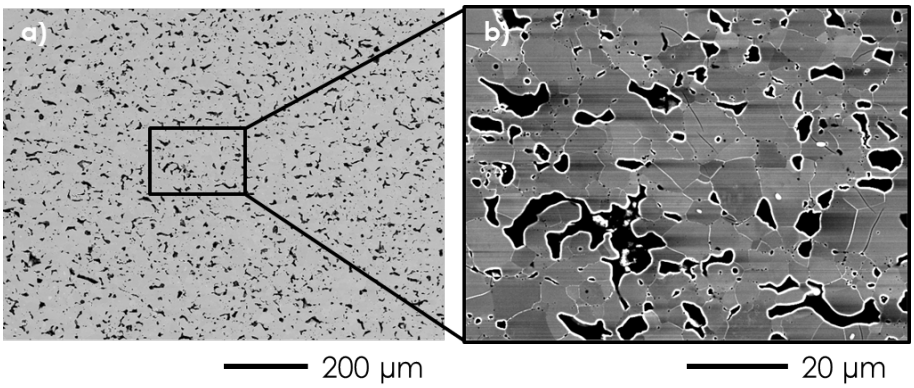

Figure 2.50: *BSE images of the microstructure of natural sintered alloy (a) and enlargement (b).*

Nominal composition	State	a (Å)	c_{Mn} (Å)	c_{Si} (Å)	γ
$MnSi_{1.73}$	RS 1100°C	5.5250(5)	4.3646(4)	2.5083(5)	1.7400(4)
$MnSi_{1.73}$	NS 1100°C	5.5232(0)	4.3643(4)	2.5120(2)	1.7373(8)
$Mn(Si_{0.992}Ge_{0.008})_{1.73}$	RS 1100°C	5.5228(5)	4.3654(6)	2.5223(3)	1.7307(2)

Table 2.10: *Refined parameters from profile matching for $MnSi_{1.73}$ obtained by reactive sintering (RS) and natural sintering (NS) and $Mn(Si_{0.992}Ge_{0.008})_{1.73}$ alloy obtained by reactive sintering (RS).*

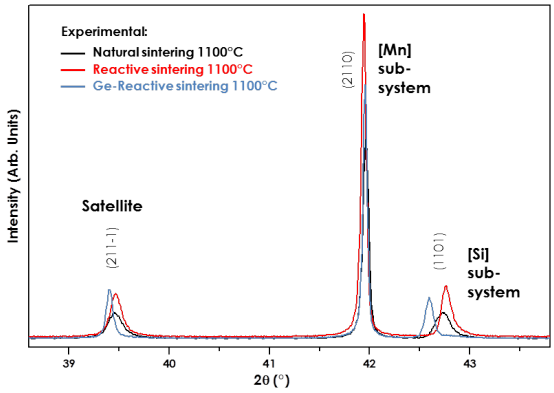

Figure 2.51: *XRD profiles for natural sintering and for reactive sintering: undoped and Ge-doped.*

Composition (at.%)		Mn	Si	Ge
Reactive sintering	without striations	37.5	62.1	0.4
As-SPS	without striations	36.9	62.7	0.4

Table 2.11: *EPMA on* $Mn(Si_{0.992}Ge_{0.008})_{1.73}$ *alloy for reactive sintering and as-SPS.*

Solid state synthesis route leads to the formation of highly pure HMS materials without MnSi striations. XRD patterns suggest that this synthesis route results in the formation of incommensurate HMS phase unlike the liquid-phase route.

2.5 Conclusion

In this chapter, we have developed a strategy based on the (3+1)D superspace group approach to interpret and index both XRD and electron diffraction patterns and unequivocally identify HMS phases. Our results reveal that the liquid-phase processes lead to the formation of a mixture of commensurate HMS phases separated by thin MnSi walls, whereas post-processing and solid state synthesis routes result in the formation of one homogeneous incommensurate phase. We conclude that, contrary to the repeated claims of several authors, it is not possible (or very improbable) to stabilize a desired specific commensurate HMS phase (in bulk). Instead, several distinct commensurate phases coexist in bulk alloys. This could be related to the structural flexibility of the Si helices in the Mn channels.

From a more technological point of view, we have set up processing routes to produce highly pure and fully dense bulk HMS materials in a reproducible manner, i.e. SPS post-processing of casted alloys and one-single step reactive sintering, respectively. The transport properties and thermoelectric performance of the materials thus obtained will be characterized in chapter 4.

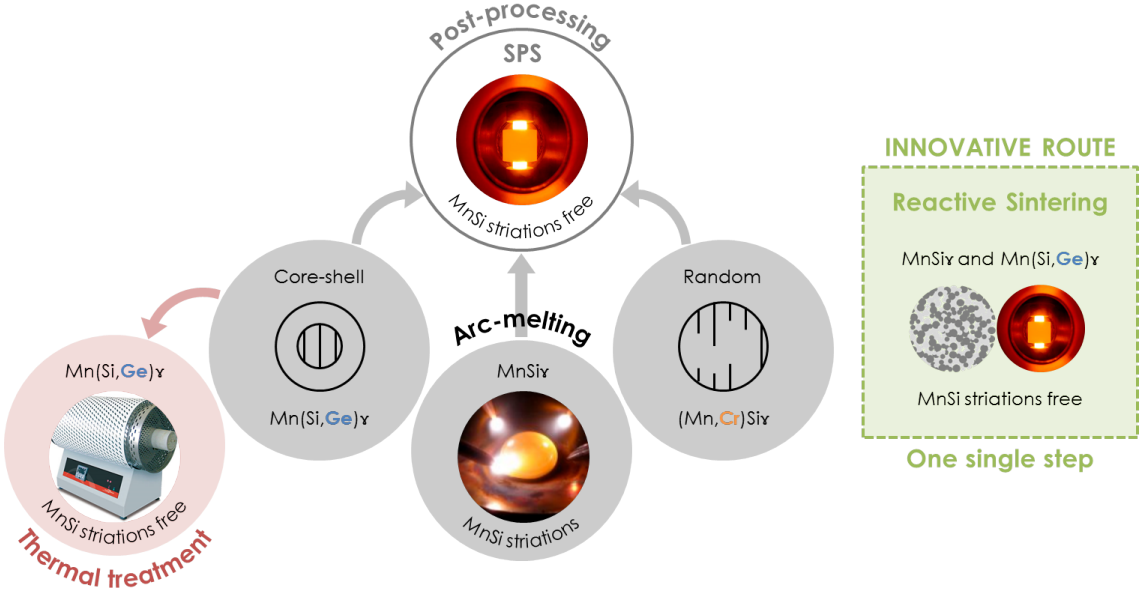

Figure 2.52: *Process pathway for HMS based-alloys.*

Bibliography

[1] A. Berche, E. Ruiz-Theron, J.-C. Tedenac, R.-M. Ayral, F. Rouessac, and P. Jund. Thermodynamic description of the mn-si system: An experimental and theoretical work. *Journal of Alloys and Compounds*, 615:693–702, December 2014.

[2] A. Berche, J.C. Tedenac, and P. Jund. Thermodynamic modeling of the germanium-manganese system. *Intermetallics*, 47:23–30, April 2014.

[3] A. Berche, E. Theron-Ruiz, J.-C. Tedenac, and P. Jund. Thermodynamic study of the ge-mn-si system. *Journal of Alloys and Compounds*, 632:10–16, 2015.

[4] A. Berche, J.C. Tedenac, and P. Jund. Ab-initio calculations and calphad description of cr-ge-mn and cr-ge-si. *Calphad*, 49:50–57, June 2015.

[5] D. C. Fredrickson, S. Lee, and R. Hoffmann. The nowotny chimney ladder phases: Whence the 14 electron rule? *Inorg. Chem.*, 43(20):6159–6167, 2004.

[6] H. W. Knott, M. H. Mueller, and L. Heaton. The crystal structure of $mn_{15}si_{26}$. *Acta Crystallographica*, 23(4):549–555, 1967.

[7] O. Schwomma, A. Preisinger, H. Nowotny, and A. Wittmann. Die kristallstruktur von $mn_{11}si_{19}$ und deren zusammenhang mit disilicid-typen. *Monatshefte fur Chemie*, 95(6):1527–1537, 1964.

[8] G. Flieher, H. Vollenkle, and H. Nowotny. Die kristallstruktur von $mn_{15}si_{26}$ - mangansilicide vom typ mn_nsi_{2n-m}. *Monatshefte fur Chemie*, 98(6):2173–2179, 1967.

[9] G. Zwilling and H. Nowotny. Crystal structure of manganese silicides with $mnsi_{1.7}$ stoichiometry. *Monatshefte fur Chemie*, 102(3):672–677, 1971.

[10] G. Zwilling and H. Nowotny. The crystal structure of the defect manganese silicide, $mn_{27}si_{47}$. *Monatshefte fur Chemie*, 104(3):668–675, 1973.

[11] U. Gottlieb, A. Sulpice, B. Lambert-Andron, and O. Laborde. Magnetic properties of single crystalline mn_4si_7. *Journal of Alloys and Compounds*, 361:13–18, October 2003.

[12] O. Schwomma, H. Nowotny, and A. Wittmann. Die kristallarten $rusi_{1,5}$, $ruge_{1,5}$ und $mnsi_{1,7}$. *Monatshefte fur Chemie*, 94(4):681–685, 1963.

[13] H.Q. Ye and S. Amelinckx. High-resolution electron microscopic study of manganese silicides mnsi$_{2-x}$. *Journal of Solid State Chemistry*, 61(1):8–39, January 1986.

[14] R. De Ridder and S. Amelinckx. The structure of defect manganese silicides. *Materials Research Bulletin*, 6(11):1223–1234, November 1971.

[15] J.M. Higgins, A. L. Schmitt, I. A. Guzei, and S. Jin. Higher manganese silicide nanowires of nowotny chimney ladder phase. *J. Am. Chem. Soc.*, 130(47):16086–16094, November 2008.

[16] S. Van Smaalen. *Incommensurate Crystallography*. Oxford University Press, 2007.

[17] P.M. De Wolff. The pseudo-symmetry of modulated crystal structures. *Acta Crystallographica Section A*, 30(6):777–785, 1974.

[18] Y. Kikuchi, T. Nakajo, K. Hayashi, and Y. Miyazaki. High temperature x-ray diffraction study on incommensurate composite crystal mnsiγ - (3+1)-dimensional superspace approach. *Journal of Alloys and Compounds*, 616:263–267, December 2014.

[19] Y. Miyazaki, D. Igarashi, K. Hayashi, T. Kajitani, and K. Yubuta. Modulated crystal structure of chimney-ladder higher manganese silicides mnsi$_{gamma}$ (*gamma* 1.74). *Phys. Rev. B*, 78(21):214104, December 2008.

[20] I. Kawasumi, M. Sakata, I. Nishida, and K. Masumoto. Crystal growth of manganese silicide, mnsi$_{1.73}$ and semiconducting properties of mn$_{15}$si$_{26}$. *Journal of Materials Science*, 16(2):355–366, 1981.

[21] E.I. Suvorova and V.V. Klechkovskaya. Precipitates of mnsi cubic phase in tetragonal mn$_4$si$_7$ crystal. 58(6):854–861, 2013.

[22] A.J. Zhou, H.G. Cui, J.Z. Li, and X.B. Zhao. Structure and morphology of induction-melted higher manganese silicide. *Acta Phys.Chim. Sin.*, 27(12):2915–2919, 2011.

[23] I. Nishida, K. Masumoto, I. Kawasumi, and M. Sakata. Striations and crystal structure of the matrix in the mnsi-si alloy system. *Journal of the Less Common Metals*, 71(2):293–301, June 1980.

[24] O. Guillon, J. Gonzalez-Julian, B. Dargatz, T. Kessel, G. Schierning, J. Rathel, and M. Herrmann. Field-assisted sintering technology/spark plasma sintering: Mechanisms, materials, and technology developments. *Adv. Eng. Mater.*, 16(7):830–849, 2014.

[25] A. Allam, P. Boulet, and M.-C. Record. Dft calculations of electronic and transport properties of substituted mn_4si_7. *Journal of Alloys and Compounds*, 584:279–288, January 2014.

[26] H. Sun, D. T. Morelli, M. J. Kirkham, H. M. Meyer, and E. Lara-Curzio. The role of boron segregation in enhanced thermoelectric power factor of $cosi_{1-x}b_x$ alloys. *J. Appl. Phys.*, 110(12):123711–4, December 2011.

[27] W. G. Zeier, A. LaLonde, Z. M. Gibbs, C. P. Heinrich, M. Panthofer, G. J. Snyder, and W. Tremel. Influence of a nano phase segregation on the thermoelectric properties of the p-type doped stannite compound $cu_{2+x}zn_{1-x}gese_4$. *J. Am. Chem. Soc.*, 134(16):7147–7154, April 2012.

[28] A.J. Zhou, T.J. Zhu, X.B. Zhao, S.H. Yang, T. Dasgupta, C. Stiewe, R. Hassdorf, and E. Mueller. Improved thermoelectric performance of higher manganese silicides with ge additions. *Journal of Electronic Materials*, 39(9):2002–2007, 2010.

[29] A. Allam, P. Boulet, C.A. Nunes, J. Sopousek, P. Broz, and M.-C. Record. Phase transformations in higher manganese silicides. *Journal of Alloys and Compounds*, 551(0):30–36, February 2013.

[30] J. S. Anderson. On infinitely adaptative structures. *Journal Chemical Society Dalton*, pages 1107–1115, 1973.

[31] W.L. McMillan. Theory of discommensurations and the commensurate-incommensurate charge-density-wave phase transition. *Physical Review B*, 14:1496, 1976.

[32] S. Aubry. *Solitons and condensed matter physics*. Springer, 1978.

Chapter 3

Crystallographic texture control in HMS

The work presented in this chapter aims at developing crystallographically textured HMS materials. The underlying idea is to exploit the expected high anisotropy of the transport properties of this compound as an additional degree of freedom to tune the thermoelectric performance.

Another strong aspect of this chapter is the endeavor that is made to produce highly pure grain oriented HMS in bulk form, allowing for the first time to unambiguously characterize the intrinsic transport properties along different crystallographic directions. This point is very important because it has not been fully resolved until now. Indeed, the hundreds of citations mentioning the anisotropy refer to the same seven papers [1, 2, 3, 4, 5, 6, 7] among which six report the properties of melt-grown single crystals. As we have shown in chapter 2, HMS materials produced by liquid-phase processes are in fact MnSi/HMS layered composites (formation of MnSi striations), so we cannot exclude that the apparent anisotropy measured in these studies would be in fact induced by the oriented plate-like metallic precipitates of MnSi.

Aside from crystal growth methods used to obtain single crystals [4], the development of crystallographic texture in HMS has been explored in the literature only by application of high magnetic fields meant to align HMS powders towards magnetically favored directions before sintering [3]. An increase of 40% of the electrical conductivity was achieved in c-axis oriented materials. The main disadvantage of this approach arises from the fact that it is not scalable since a high magnetic field (10 T) is required.

Texture development in bulk materials generally occurs by deformation, and various thermome-

chanical techniques were successfully applied on thermoelectric compounds exhibiting a significant amount of plasticity at elevated temperature [8]. Unfortunately, HMS alloys present a purely elastic mechanical behavior so thermomechanical processing such as rolling or extrusion is not applicable.

Consolidation under hot unixial compression can also yield to strongly textured materials provided that the starting powders possess crystallographically anisotropic morphologies. This occurs for mechanically ground powders of Bi_2Te_3 alloys due to the easy cleavage of certain planes [9] and in several thermoelectric oxides as discussed by Medlin *et al.* [10]. We have decided to explore a variant of this technique from the experience acquired during this thesis, namely that ground powders of HMS show an isotropic morphology so they would be useless for the present purpose. To circumvent this issue, the idea is to produce anisotropic flakes that will align under compression to give crystallographic textured compacts. We have selected the melt-spinning process because it usually leads to the production of flakes in brittle materials and it can induce grain alignment along preferred growth directions due to the high thermal gradient that is developed through the material thickness during cooling. Another attractive aspect of the melt-spinning is the grain refinement due to high cooling rates, for improvement of both thermoelectric properties and mechanical behavior [11, 12].

The main purpose of this study is to evaluate the degree of grain orientation that can be obtained in the melt-spun flakes and retain in the bulk form after a subsequent consolidation by spark plasma sintering.

In the first section of this chapter, we present the experimental procedure established to produce oriented HMS materials and summarize the characterization techniques used to investigate the microstructural parameters of the materials thus obtained. The texture development and evolution in the melt-spun flakes and the bulk consolidated materials are evidenced by mean of electron backscatter diffraction, in sections 2 and 3, respectively. The possible avenues for improvement of texture are discussed in the last section.

.

3.1 Experimental procedure

3.1.1 Fabrication of crystallographic textured HMS based materials

The procedure developed to produce bulk grain oriented HMS materials is summarized in figure 3.1.

Figure 3.1: *Experimental procedure for the production of isotropic and textured materials with melt-spinning process.*

Production of flakes by melt-spinning

Melt-spinning is a technique to rapidly solidify liquid metals and it is widely used to produce metallic glasses, nanostructured alloys and highly metastable phases [13, 14, 15, 16]. Obtaining HMS flakes is achieved by dropping an inductively melted alloy on a rotating wheel usually made of copper that allows a fast quenching (up to $\sim 10^6$°C/s) due to the high thermal conductivity of the copper.

The HMS flakes were obtained with a Melt Spinner SC from Edmund Bühler GmbH; using a quartz tube with a 0.5 mm diameter nozzle, an overpressure of 350 mbar of Argon and a copper wheel linear speed of 38.5 m/s (i.e. 46 Hz). Prior to the flake production a secondary vacuum was established in the chamber of the melt-spinner. The experiments were performed with 4 g arc melted ingots and after solidification the flakes are selected for characterization ($\sim$3 g), the losses are due to splash and balls created during the solidification.

The HMS flakes are typically 1-2 mm wide, around 20 μm thick and less than 1 cm in length. Experimentally, the melt-spinning conditions were optimized to maximize the production of flakes.

Hereafter, the surface in contact with the copper wheel will be called the contact surface and the opposite surface will be called the free surface. For all the samples of this chapter the nominal composition of the alloys is fixed at γ=1.73.

Consolidation of the flakes by SPS

The melt-spun flakes (2.6 g per pellet) were stacked in a graphite die and consolidated by SPS under various conditions in order to find the optimal dwell temperature leading to the best compromise between grain growth and high density. Another set of samples were prepared from ground flakes in order to obtain isotropic materials for comparison with staked flakes. The ground flakes were densified under the same conditions as ground powder from arc melted route (see figure 3.2). For these two materials the sintering cycle is identical as previously presented in chapter 2.

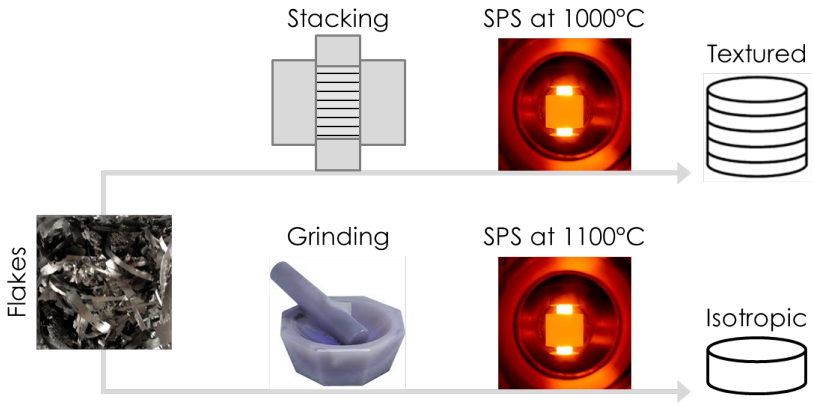

Figure 3.2: *Detailed experimental procedure for isotropic and textured materials.*

Figure 3.3 shows the microstructures in the transverse direction of the stacked pellets as a function of the dwell temperature (850°C to 1100°C). The average grain size is calculated thanks to the intercept method [17]. For this analysis several SEM images where used to analyze 1225 intercepts leading to an uncertainty of 2%. The average grain size values are reported on SEM images on figure 3.3. They range from 8 to 17 μm as sintering temperature increases from 850°C to 1100°C. At 1000°C the relative density is found to be close to 100% and a further increase in temperature leads to an excessive grain growth. At lower temperature the relative density is decreased. In light of these results, we fixed the dwell temperature at 1000°C.

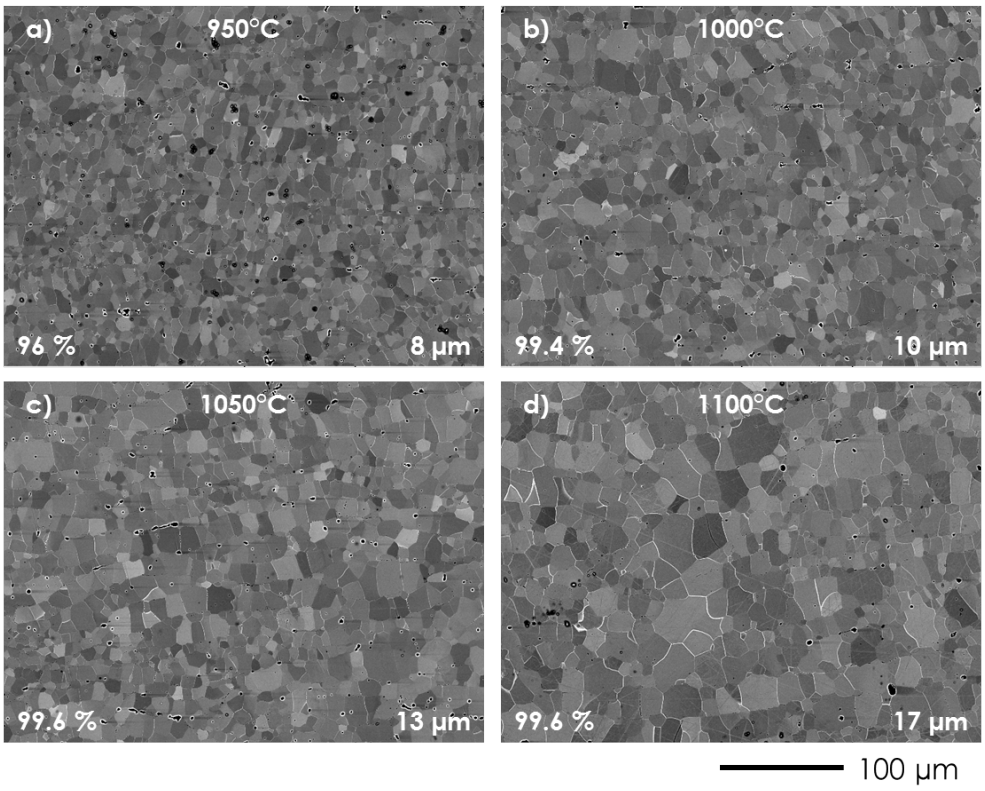

Figure 3.3: *SEM images as a function of the dwell temperature for the stacked flakes densified by SPS at: 950°C (a), 1000°C (b), 1050°C (c) and 1100°C (d); with their respective average grain size and relative density. The average grain size is determined by the intercept method. The density of the materials is measured by Archimedes principle and the relative density is calculated from theoretical density of 5.159 g/cm^3 for HMS.*

3.1.2 Texture analysis

Electron BackScatter Diffraction (EBSD) is a technique used to determine the orientation of crystallized materials. This analysis is used to highlight the grain parameters: size, orientation, boundary character, texture and phase identity of a polycrystalline sample. EBSD analysis was performed in the SEM chamber with an EDAX accessory. The figure 3.4 shows the experimental setup.

The sample is highly tilted at 70° towards the detector where the diffracted electrons are collected in order to maximize the retro-diffusion coefficient. The primary electron beam interacts with the crystallographic planes that are in Bragg position: $2d_{hkl}\sin\Theta = n\lambda$. The two resulting diffracted surfaces are conical and the pair of cones corresponds to the {hkl} and {-h-k-l} family planes. Their interception with a phosphor screen leads to a pair of lines also called Kikuchi bands (due to the low value of Θ i.e. the large opening of the cones). Bright Kikuchi bands correspond to planes in the crystal

lattice and the width of bands is dependent upon electron wavelength and lattice plane spacing.

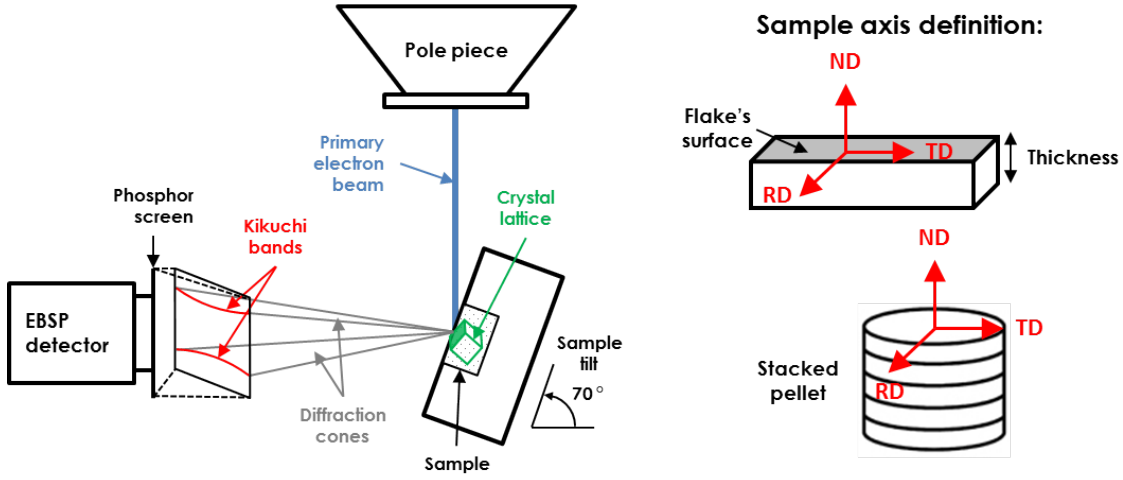

Figure 3.4: *EBSD setup in the SEM chamber (left) and sample axis definition (right).*

The sample is generally set along with the reference coordinate of the measurement. Three directions are defined to correlate the crystal to the sample frame:

- ND: Normal Direction
- TD: Transverse Direction
- RD: Rolling Direction or Reference Direction

In our study, the reference is set as a function of the flake's shape or staked pellet (see figure 3.4).

The EBSP (Electron BackScatter Patterns) contains the angular relationship between the planes, the symmetry of the crystal and orientation information. The patterns are collected with an accelerating voltage of 20 kV, an incident beam current of 4 nA and a working distance of 17 mm.

As evidenced in chapter 2, the superlattice of HMS phases can become very complicated. Due to their resemblance apart from the c-axis length, the smallest HMS phase Mn_4Si_7 is selected in order to reduce the complexity of the crystal structure. This choice is supported by the work of Orekhov *et al.* where the Mn_4Si_7 phase was successfully used with a high confidence index to study doped HMS crystals grown by Bridgman technique [18].

A phase file was created for HMS alloys based on the structure of the commensurate Mn_4Si_7 phase (ICSD # 97393) were 8 Kikuchi bands are needed to index the EBSP. The phase file data are listed on table 3.1 and the selected Kikuchi bands for HMS analysis along with an indexed EBSP are shown on figure 3.5.

Mn_4Si_7 with space group: P-4c2

Atom	#	Site	x	y	z	Occ.
Mn	1	2c	0	0	0	0.25
Mn	2	4i	0.5	0	0.06508(2)	0.5
Mn	3	4h	0.5	0.5	0.12639(3)	0.5
Mn	4	4i	0	0.5	0.19137(3)	0.5
Mn	5	2a	0	0	0.250	0.25
Si	1	8j	0.15715(13)	0.2015(2)	0.11253(4)	1
Si	2	8j	0.32270(12)	0.844419(12)	0.18189(4)	1
Si	3	4e	0.33130(12)	0.33130(12)	0.250	0.5
Si	4	8j	0.34518(10)	0.2274(1)	-0.03800(6)	1

Table 3.1: *Mn_4Si_7 phase file for OIM software used to index the isotropic and textured materials. The first three rows indicate the different Mn and Si atoms and their Wycoff position, the three following rows report the atomic position in the crystal structure (x,y,z) and the last one: Occ. is the abbreviation for the occupancy.*

Kikuchi band	F_{hkl}	d_{hkl}
00-6	29.7	2.919
1-2-3	29.7	2.275
1-2-4	25.3	2.152
1-1-7	28.7	2.107
2-20	33.4	1.953
1-1-8	23.1	1.910
0-3-4	32.6	1.698
3-38	19.8	1.119

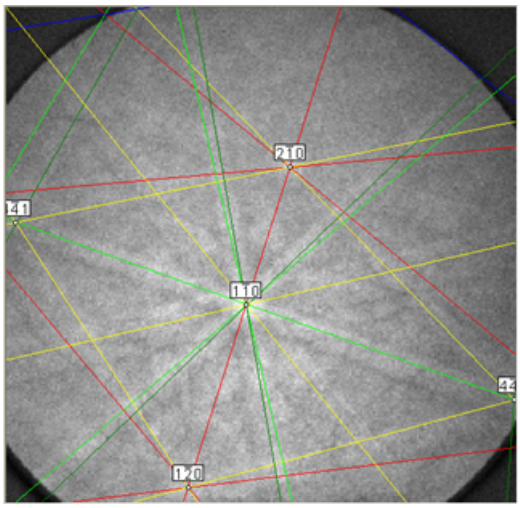

Figure 3.5: *List of the 8 Kikuchi bands selected to index HMS phase (left) and an example of a diffraction pattern where the all the Kikuchi bands are correctly indexed (right). F_{hkl} is the structure factor and d_{hkl} is the interplanar spacing.*

Sample preparation EBSD analysis requires a highly polished surface (free of deformation and pollution) that will guaranty a good quality of the EBSP; as the diffraction comes from the surface of the sample (from 10 to 50 nm in depth).

The preparation of the sample is done thanks to a classical mirror polishing performed with SiC papers (320 to 4000) and a final polishing step with diamond solutions (3 and 1 μm) on a synthetic nap (MD-Nap from Struers). In order to reveal the Kikuchi bands a mechanochemical preparation with a colloidal silica polishing suspension (MasterMet2 from Buehler, 0.02 μm) is performed with a vibratory polisher (VibroMet2 from Buehler) during 3h, 40% of vibrations and 3 loads. This final step removes the minor deformations and leads to a stress-free surface. In order to study the cross-section of the flakes they are maintained perpendicular to the polishing surface thanks to a metallic clip trapped in the conducting resin.

Data analysis The data are analyzed thanks to the Orientation Imaging Microscopy (OIM™) software from EDAX. From Kikuchi diffraction patterns it is possible to build different texture plots (PF, IPF,...) and maps: orientation, grain size, grain boundaries,...

Hereafter we summarize the different plots and maps used during this chapter along with a brief definition.

- Pole Figure (PF): in a PF (hkl), an orientation is described by the position of the equivalent pole planes {hkl} of the crystal. A pole figure is the stereographic projection on the sample plane of the pole density distribution for a family of planes {hkl} in all the directions of the sample. If a sample presents no preferential orientation the points will be randomly spread whereas in a textured sample points will be focused in a specific region.

- Inverse Pole Figure (IPF): is used to easily illustrated the orientations of a sample with a color representation. The IPF shows the position of a sample direction in the crystal frame. Due to the crystal symmetry the representation can be restricted to the standard triangle. The minimum display area triangle changes from symmetry to symmetry and the one for tetragonal system is showed on figure 3.6. Full red, green and blue are attributed to grains whose <001>, <100> and <110> directions, respectively, are parallel to the projection of the IPF. The intermediate orientations are colored by RGB mixture of primary components.

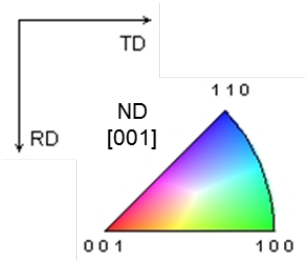

Figure 3.6: *Standard triangle in the normal direction for a tetragonal structure.*

- Image Quality (IQ) map: shows the quality of the EBSP with a gray scale where black color is attributed to blurred Kikuchi diagrams and white to distinct ones. This map is useful to locate the grain boundaries that will appear in black or dark gray.
- IPF map: shows the microstructure of a sample where each grain is colored as a function of its crystallographic orientation.
- Crystal direction map: shows the directions of interest along with the corresponding area fractions. The directions are given with a tolerance (°) extracted from pole plot analysis.
- Grain size map: shows the distribution of grain sizes along with the corresponding area fractions. The color scale is set depending on the sample grain sizes and on the aim of this representation.

3.2 Characterization of the melt-spun flakes

3.2.1 Structure and microstructure

Figure 3.7 presents the topographies of the contact and free surfaces of a flake. Opposite surfaces present a very different aspect: the contact surface shows surface roughness due to the footprints of the argon bubbles trapped during the experiment. Contrary to the free surface that presents a roughness due to the free grain growth. At this side of the flake several islands exhibiting different grain sizes are observed.

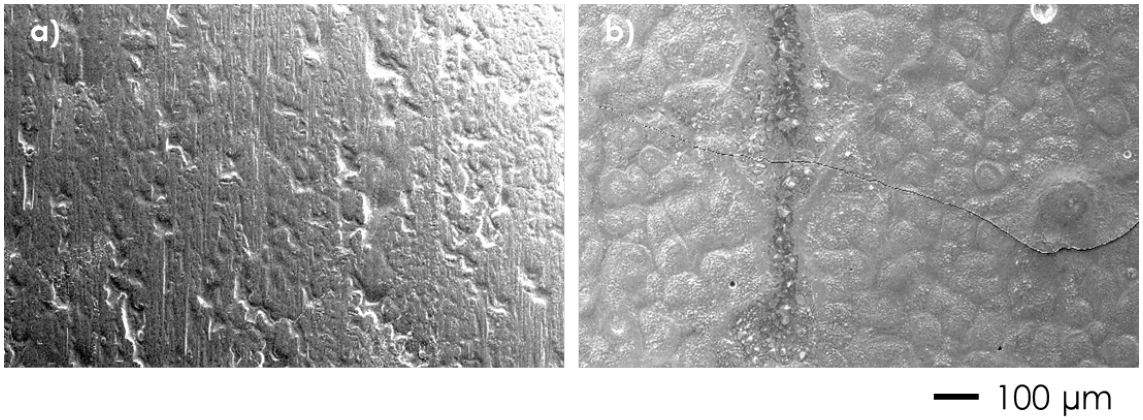

Figure 3.7: *SE images of the contact surface (a) and free surface (b) of one as-spun HMS flake with composition* $MnSi_{1.73}$.

The two enlargements of both surfaces on figure 3.8 show that the shape of the grains is flat on the contact side leading to a low roughness contrary to what is observed in the free surface. We can also notice a refinement of the Si eutectic aggregates present on both surfaces that were already highlighted in arc-melted samples. It is to notice that MnSi primary dendrites were not evidenced.

The grain size is refined compared with arc-melting process: from hundreds of μm to tens, however the optimized conditions of melt-spinning do not lead to a nanostructuration.

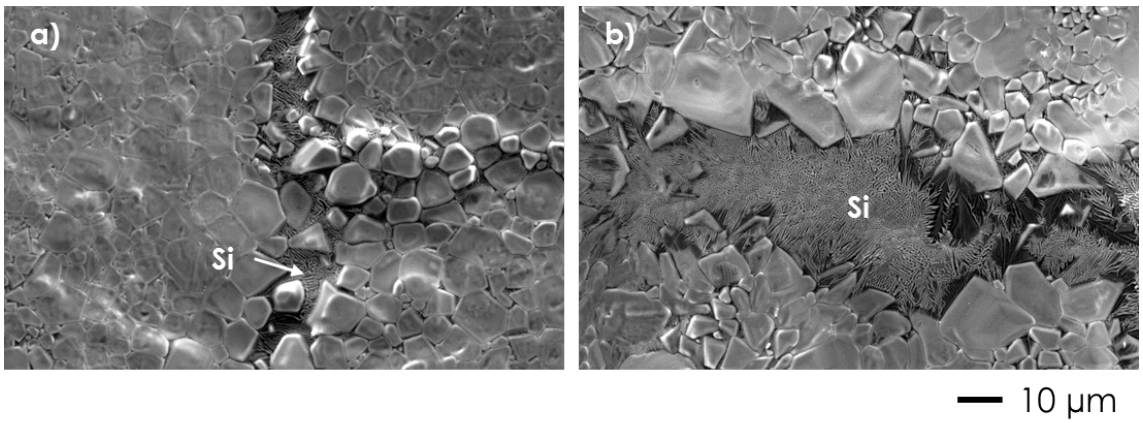

Figure 3.8: *Enlarged SE images of the contact surface (a) and free surface (b) of one as-spun flake of* $MnSi_{1.73}$.

In order to measure the average grain size at the flake surface a map highlighting the grains distribution is presented on figure 3.9. The grains are smaller than 15 μm, mainly distributed from 0 to 10 μm and the average grain size is found to be 6 μm. Between the arc melting and melt-spinning techniques the grain size is at least divided by 20, showing a great grain size refinement.

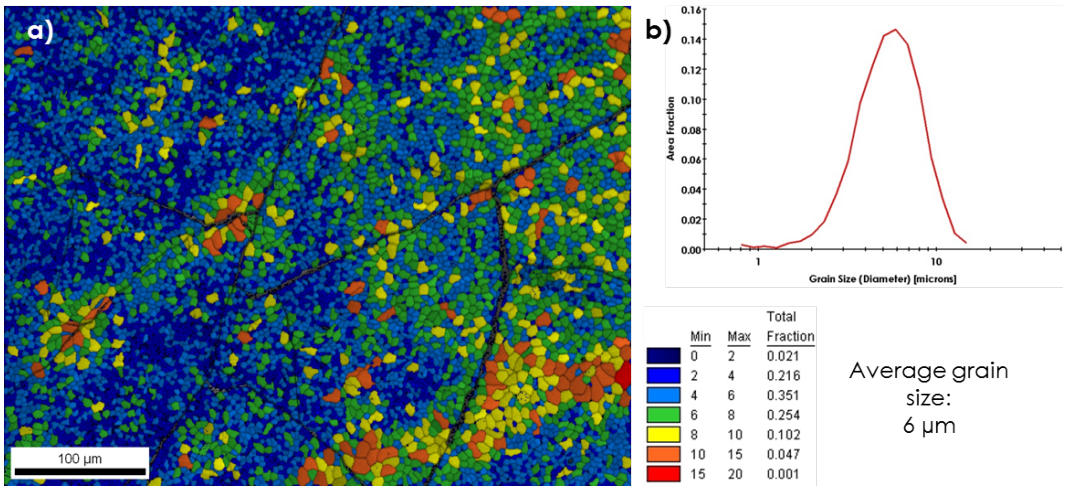

Figure 3.9: *Grain size map (a) and grain size variation (b) at the flake's surface. The colored scale highlights the grain size distribution from 0 to 20 μm.*

Figure 3.10 shows an image used to measure the thickness of the flakes that is found to vary in the range 15-25 μm. The thickness of the flakes is very sensitive to the processing parameters: melt temperature, wheel temperature or gas pressure. During the experiment these conditions can be slightly changed from the first drop to the ending one and lead to a variation in the flake's thickness

[19]. In addition, elongated grains in the direction of the thermal gradient are found in the thickness of the flakes between the contact surface and the free surface (see figure 3.10). MnSi striations are also evidenced. As evidenced in chapter 2 for arc-melted samples the presence of MnSi striations was always related to the formation of a mixture of commensurate HMS phases and associated to the asymmetric broadening of the [Si] and satellites peaks in the XRD patterns. To verify either or not it is the case for melt-spun flakes, we perform an XRD analysis.

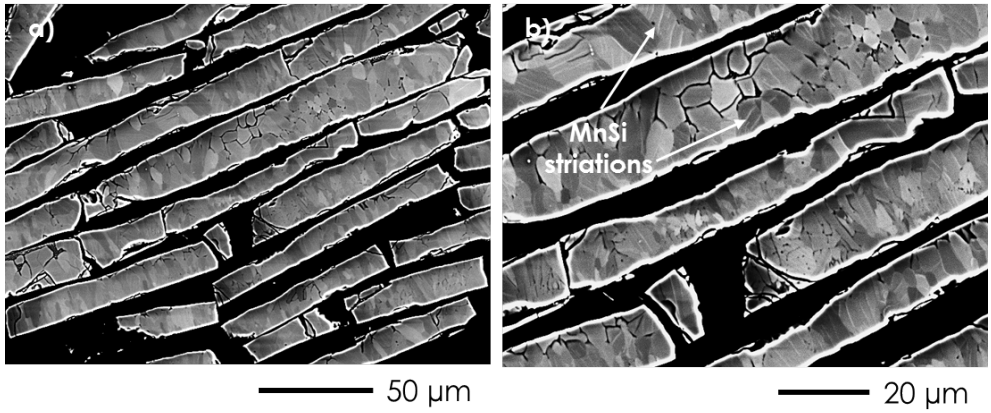

Figure 3.10: *BSE images in crystallographic contrast of the cross-section of the flakes taken in crystallographic contrast (a) and enlargement (b).*

Profile matching refinement performed on powder is shown on figure 3.11 and the refined lattice parameters from profile matching are: a=5.5218(1) Å, c_{Mn}=4.3653(2) Å, c_{Si}=2.5225(2) Å and c-axis ratio $\varkappa$=1.7305(4).

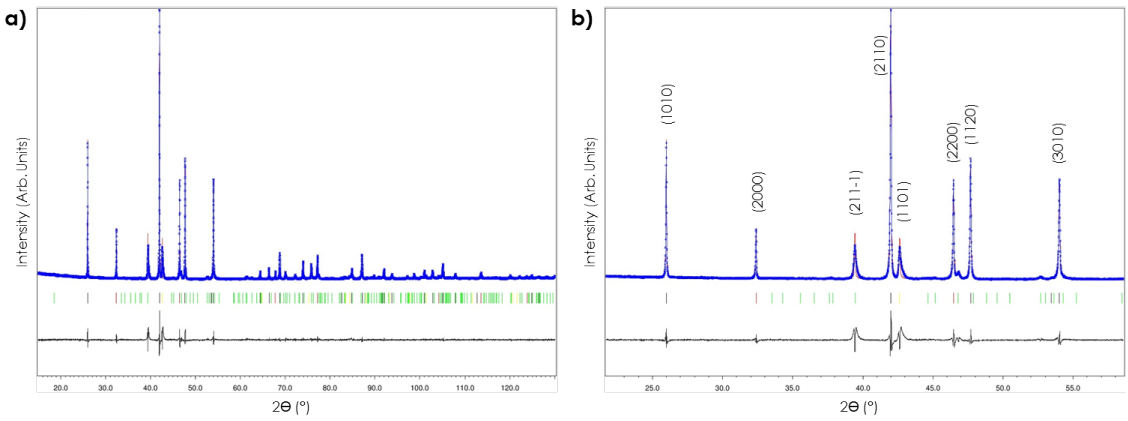

Figure 3.11: *Profile matching for melt-spun $MnSi_{1.73}$ alloy: complete (a) and enlargement (b).*

Figure 3.12.a. focuses on [Si] peak (1101) where we can observe the expected asymmetric broad-

ening. According to the simulated XRD patterns (see figure 3.12), the main contributions arises from the reflections of $Mn_{11}Si_{19}$ (γ=1.72727...) and $Mn_{15}Si_{26}$ (γ=1.73333...). For the arc melted samples the main contributions were $Mn_{15}Si_{26}$ and $Mn_{27}Si_{47}$. It appears that the formation of HMS phase with smaller c parameter is formed by the melt-spinning.

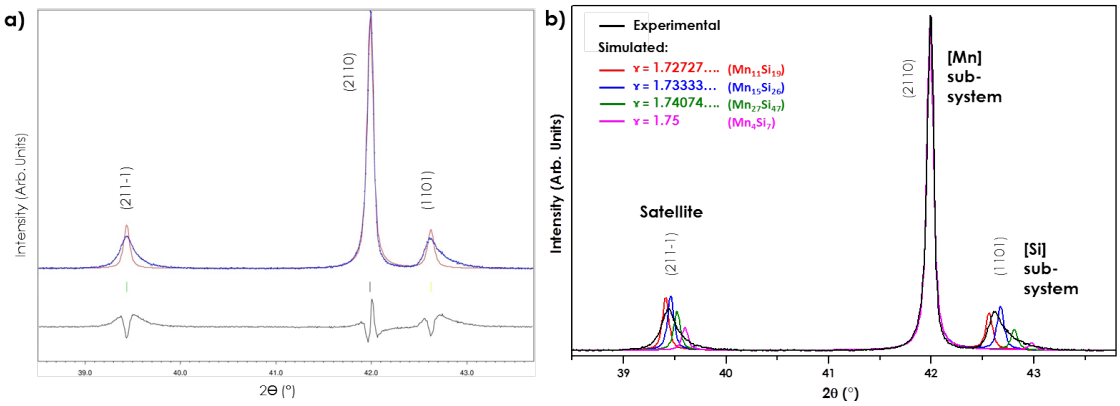

Figure 3.12: *Enlargement in profile matching for melt-spun $MnSi_{1.73}$ alloy (a) and simulated XRD patterns of the four commensurate HMS phases superposed on experimental data for melt-spun $MnSi_{1.73}$ alloy (b).*

These results confirm the main structural and microstructural parameters associated to a liquid-phase process (mixture of commensurate HMS phases and presence of MnSi striations) and highlight three differences with arc-melted samples: the grain size, the lack of MnSi dendrites and a change in the distribution of HMS commensurate phases. We will hereafter focus on the textural study of the flakes thanks to EBSD analysis.

Melt-spun HMS flakes present a mixture of commensurate phases and exhibit MnSi striations which are typical characteristics observed with liquid-phase processes.
Refined grain size is found compared to as-cast samples and an elongated grain shape are evidenced within the thickness of the flakes.

3.2.2 Grain orientation

Figure 3.13 presents a IQ+IPF map along with the IPF and texture plots of a flake surface (normal direction) and the IQ+IPF map of the cross-section of a flake (transverse direction) are shown on figure 3.14. The surface presents cracks resulting from the flakes preparation as HMS is a brittle material.

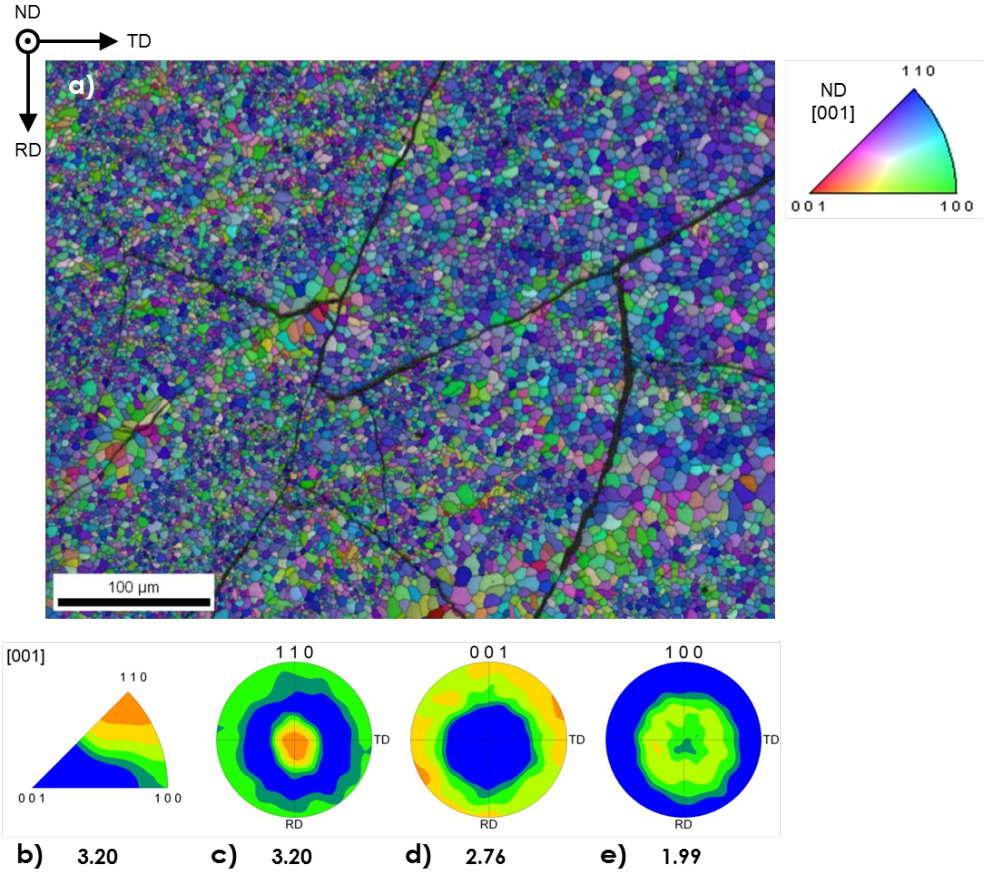

Figure 3.13: *IQ+IPF map (a), IPF [001] (b), PF (110) (c), PF (001) (d) and PF (100) (e) at the surface of the flake. More than 8000 grains are analyzed. The texture is normalized on a scale of 5 and the maximum of texture is indicated above each IPF and PF.*

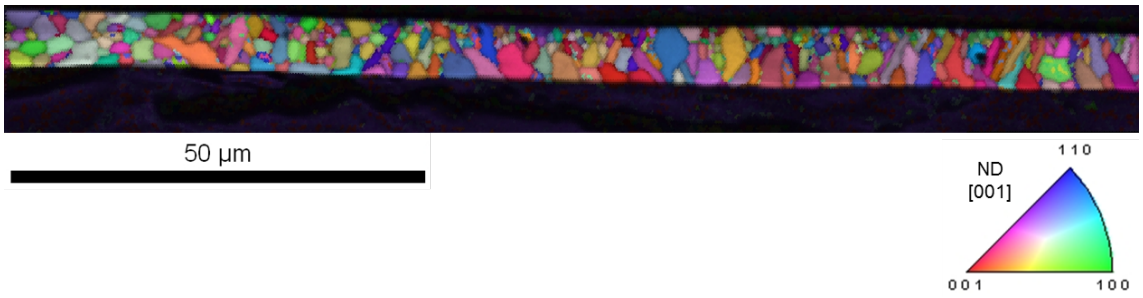

Figure 3.14: *IPF+IQ map of the cross-section of a flake.*

On the surface, the grain orientation along the <110> direction (blue grains) is obvious while the grain orientation in the cross-section is nearly isotropic with a slight preferential orientation along the <001> direction (red grains). The IPF along the normal direction [001] (see figure 3.13.b.) clearly

reflects the orientation of grains along the <110> direction.

The analysis of the texture plot (110) shown on figure 3.13.c. indicates that the material develops a fiber texture in which the [110] axis is oriented parallel to normal direction and posses a free rotation around this axis. The central spot is due to the (110) planes whereas the (-110) planes are shown by the external ring at 90° from normal direction. This texture leads to a c-axis that is uniformly oriented in the rolling plane describing a ring-like, as observed on the pole figure (001) (see figure 3.13.d.) that is the reason why we cannot observe (001) planes (red color) at the flake's surface. Finally, the pole figure (100) (see figure 3.13.e.) highlights that the (100) planes are uniformly oriented around 45° from the normal direction..

In order to quantify the texture of the flake figure 3.15 shows the crystal direction map where the (110) and (001) planes are highlighted in blue and red respectively. The (110) planes represent half of the analyzed area at the flake's surface whereas the (001) planes are not evidenced.

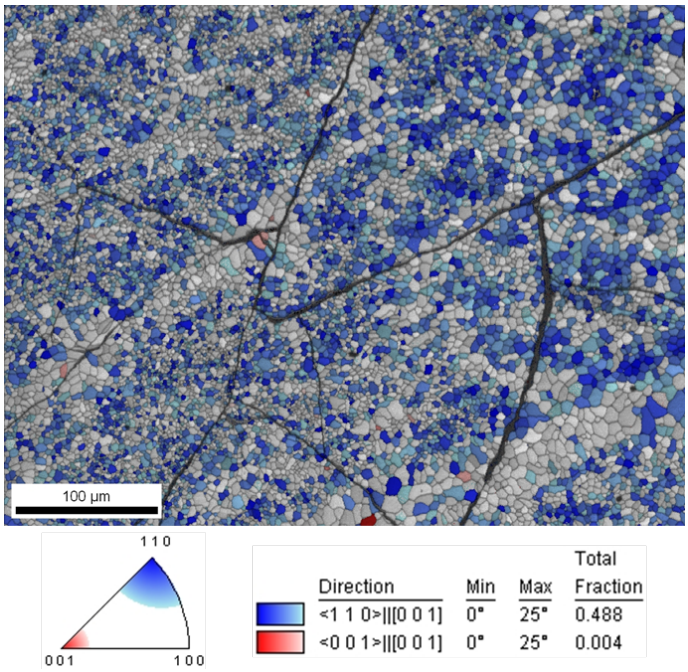

Figure 3.15: *Crystal direction map where (110) and (001) planes are highlighted respectively in blue and red at the surface of the flake. For each plane the area fraction is indicated showing that half of the grains are oriented in <110> direction whereas (001) oriented planes are not evidenced.*

3.2.3 Discussion about the texture development

Figure 3.16 describes the texture that is developed in melt-spun HMS flakes as evidenced by EBSD analysis. The crystal structure of HMS is drawn with respect to the cross-section in order to highlight the (110) planes preferentially oriented parallel to the flake's surface and the c-axis that is isotropically distributed in the equatorial plane ("ring-like"). This fiber-like texture that is developed during the solidification is determined by the preferential growth direction and the thermal gradient.

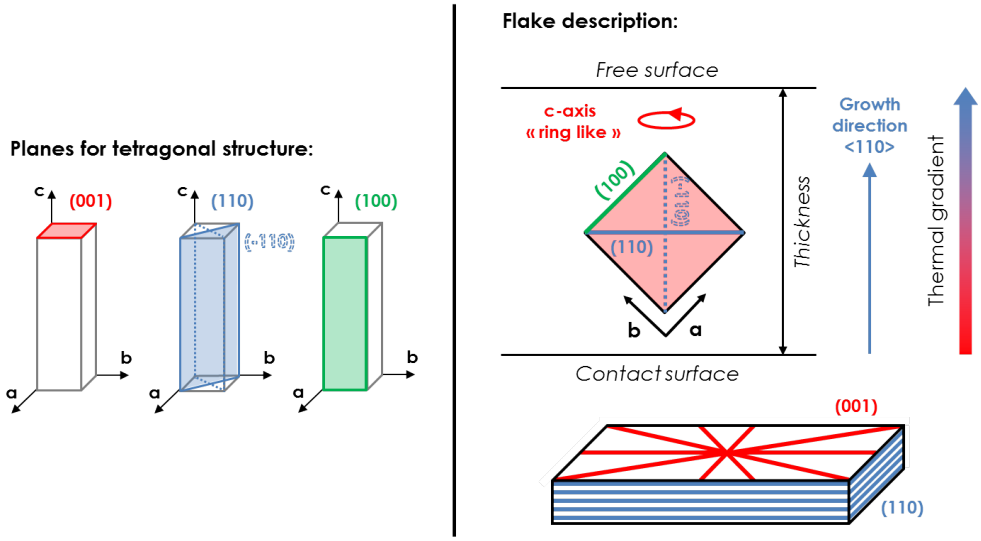

Figure 3.16: *Description of the texture of the flakes. The planes (001), (110) and (100) are drawn in the tetragonal structure (left) and their respective orientation is drawn on the cross-section and on the 3D representation of a flake (right).*

At the beginning of the solidification, when the first HMS crystallites start to form in contact with the copper wheel, those with the preferred direction aligned towards the direction of heat flux (perpendicular to the wheel surface, in others words throughout the flakes thickness) will be promoted, preventing the growth of the others orientations.

From a general point of view, the preferred growth direction is strongly correlated to the crystal structure and the direction of heat conduction, however more factors can interplay so it is difficult to predict the preferred orientation of the growing solid-liquid interface.

In their theoretical study, Chattopadhyay *et al.* [20], predicted that for tetragonal (bct) crystals the growth rate along the <110> direction is the fastest among all other directions because it corresponds to the higher atomic density. These results are in agreement with the experimental work of Weinberg and Chalmers [21] where <110> is found to be the preferred orientation of bct-tin, whereas O'Hara [22]

considered that pure tin grows in a direction 12° away from <110>. As discussed by Chattopadhyay *et al.* [20], the resultant growth direction of bct is selected by the combined effect from the <110> and <100> directions. The directions we observed for HMS, mainly <110> and to a less extend <100>, match well the predicted and observed preferential growth of others tetragonal crystals.

It is also interesting to note that the thermal conductivity of HMS crystals is supposed to be two times higher in directions perpendicular to the c-axis, so the growth of HMS is expected to be favored in these directions where the thermal conductivity is increased with respect to the thermal gradient.

Melt-spun flakes are posses a fiber-like texture of the (110) planes at their surface.

3.3 Characterization of the bulk samples

3.3.1 Structure and microstructure

Figure 3.17 presents the microstructures of the ground and stacked compacts after SPS consolidation.

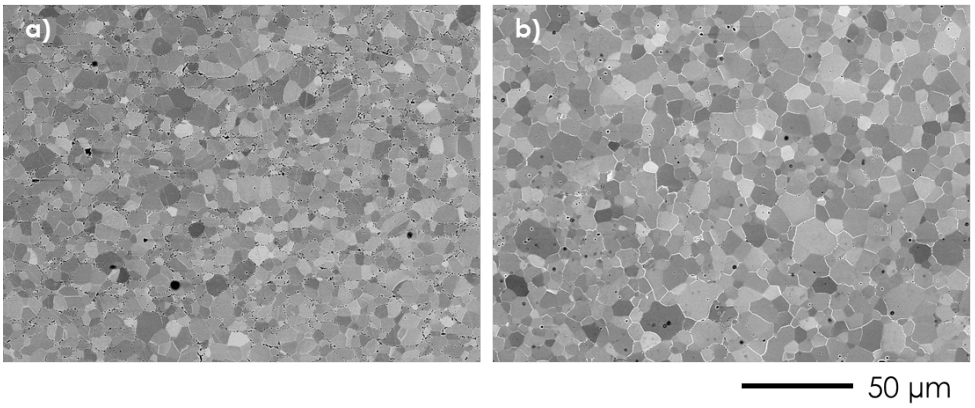

Figure 3.17: *BSE images taken in crystallographic contrast for ground (a) and stacked (b) compacts.*

Contrary to what is observed for ground materials from arc melting route (chapter 2) the grain morphology of melt-spun samples is uniform with less porosity at grain boundaries. Stacked materials made of staked flakes presents the cleanest grain boundaries. In addition, for both samples MnSi striations are not observed in HMS phase after post-processing.

Table 3.2 shows the refined parameters obtained for the melt-spun materials after SPS. In comparison with the melt-spun material (figure 3.12.a.) no significant changes are evidenced in the cell parameters.

Material	SPS	a (Å)	c_{Mn} (Å)	c_{Si} (Å)	γ
Ground	1100°C	5.5247(6)	4.3643(1)	2.5075(4)	1.7404(8)
Stacked	1000°C	5.5222(2)	4.3639(4)	2.5172(0)	1.7336(5)

Table 3.2: *Refined lattice parameters a, c_{Mn}, c_{Si} and γ obtained by profile matching for ground and stacked compacts after post-processing.*

However, contrary to what was observed in chapter 2 for casted samples the asymmetric broadening of the [Si] peak (1101) is still present after post-processing for the textured sample (see figure 3.18). As observed in the diffraction pattern (see figure 3.19) HMS is incommensurate.

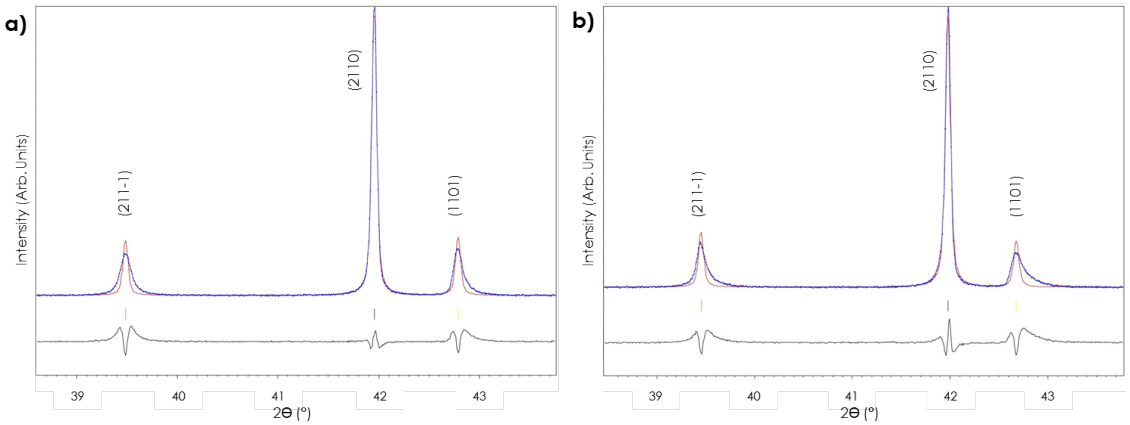

Figure 3.18: *Enlargement in profile matching for ground (a) and stacked (b) materials.*

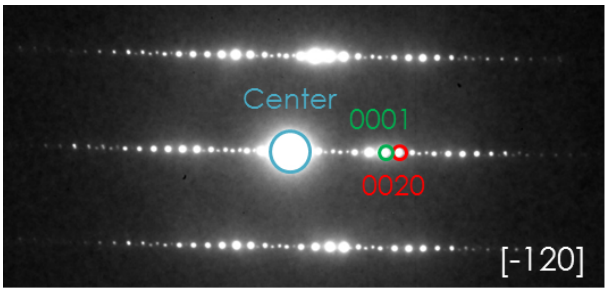

Figure 3.19: *Diffraction pattern of the stacked material taken along [-120] zone axis the on powder showing the incommensurate character of HMS phase. The incommensurate character is confirmed after analysis of several diffraction patterns performed on different powder particles.*

The microstructures of consolidated compacts present a uniform grain size distribution with a low porosity content, clean grains boundaries and without MnSi striations.

After post-processing the incommensurate character is evidenced for ground and stacked bulk materials.

3.3.2 Texture

Ground compacts Figure 3.20 presents an IQ+IPF map along with the IPF for an ground pellet. As expected this pellet is fully isotropic and do not present any texture.

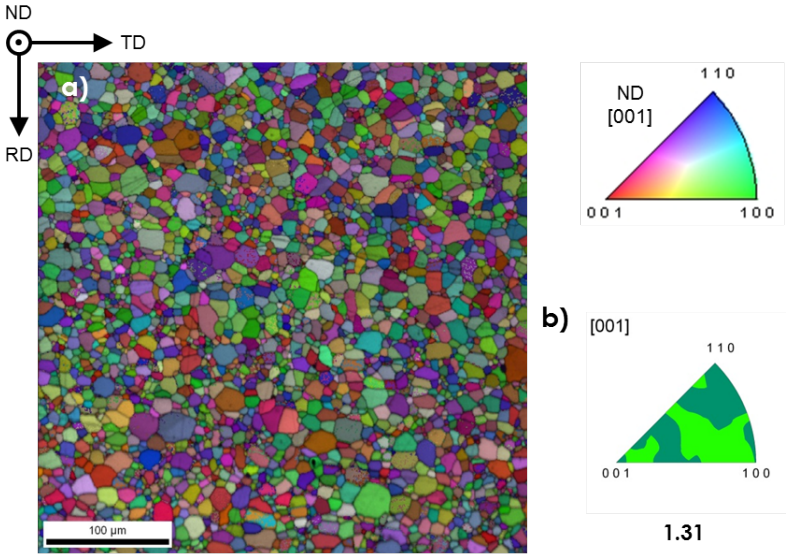

Figure 3.20: *IQ+IPF map (a) and IPF [001] (b) of the isotropic pellet in the normal direction. More than 2500 grains are analyzed. The texture is normalized on a scale of 5 and the maximum of texture is indicated above the IPF.*

Stacked compacts Figure 3.21 presents the IQ+IPF maps in the normal and transverse directions along with the corresponding IPF and texture plots. The stacking of the flakes is easily observed in the transverse cut. From IPF analysis (see figures 3.21.b. and e.) we confirm the presence of mainly oriented (001) grains in the transverse direction and mainly oriented (110) grains in the normal direction. The pole figure (001) (see figure 3.21.c.) of the transverse direction confirms the development of the c-axis ring-like texture within the thickness of the flakes. And the pole figure (110) (see figure 3.21.f.) of the normal direction presents a typical fiber-like texture similar to the one obtained at the flake's surface.

After SPS we successfully retain the texture of the flakes leading to a textured bulk material.

However, a diminution of the maximum of the pole figure is observed.

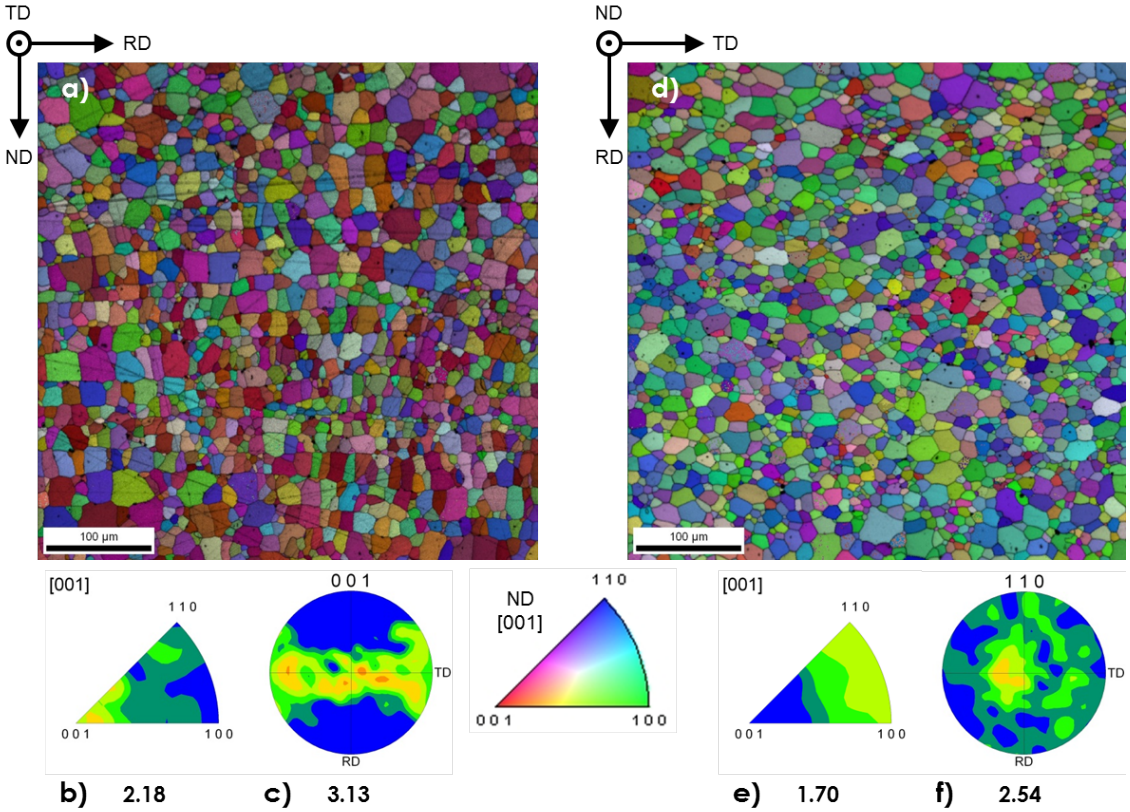

Figure 3.21: *IQ+IPF map, IPF [001] and PF (001) of the textured pellet in the transverse direction (a,b and c) and in the normal direction (d,e and f) where more than 1500 grains are analyzed. The texture is normalized on a scale of 5 and the maximum of texture is indicated above each IPF and PF.*

Figure 3.22 shows the crystal direction map where the (110) planes are highlighted in blue and in comparison to the flake's surface previously analyzed we observe a decrease of about 10% in their area fraction (from 0.488 to 0.376). This decrease comes from flake's rotation, sliding, crushing and bending that can occur during their stacking in the graphite die before the densification.

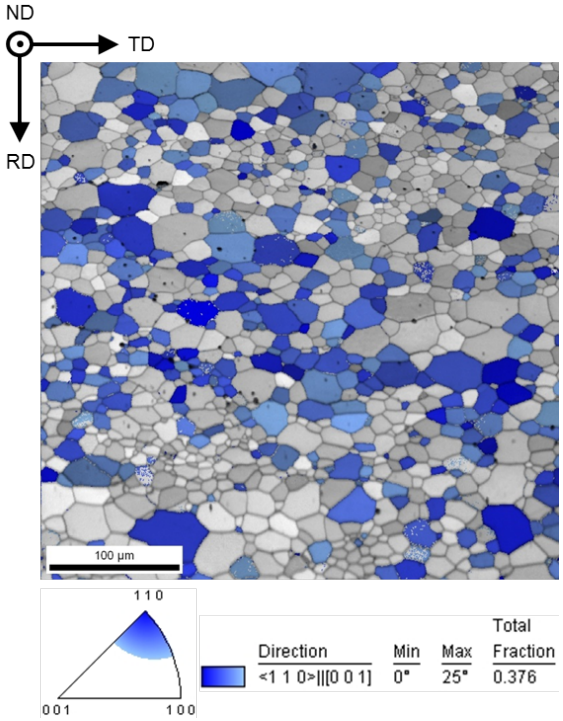

Figure 3.22: *Crystal direction map where (110) planes are highlighted in blue. The area fraction is indicated showing close to 40% of the area fraction is oriented in <110> direction. More than 800 grains are analyzed.*

Textured bulk HMS samples are successfully obtained through melt-spinning followed by SPS procedure even if a diminution of the texture is observed.

3.3.3 Possible avenue for texture strengthening

The issues related to the imperfect stacking of the flakes during the sample preparation being hardly avoidable, an alternative solution to enhance the texture of the final compacts would be to start with texturally stronger flakes.

As discussed in the book of F.J. Humphreys and M. Matherly [23], a texture can be strengthen during annealing due to a phenomena called oriented growth. The underlying mechanism is that some orientations of grains have a growth advantage compared to others because their grain boundary mobility is higher. There is evidence that the mobilities are dependent on grain boundary orientation so that certain orientation relationships are associated with a rapid growth rate [24]. It is this relationship between the fast-growing orientations and boundary structure which can enhance the texture of grain

oriented materials during annealing because the misorientation distribution is altered. To this respect, it was observed that special boundaries which have a high density of coincidence sites often exhibit fast rates of growth.

To take advantage of this oriented growth phenomena, we have investigated the effect of annealing on the crystallographic texture of the melt-spun HMS flakes. The annealed texture is shown on figure 3.23. It is observed that grain growth results in substantial strengthening of the fiber like texture of the flakes. This suggests a strategy for enhancing the texture of bulk HMS materials by using annealed flakes during consolidation.

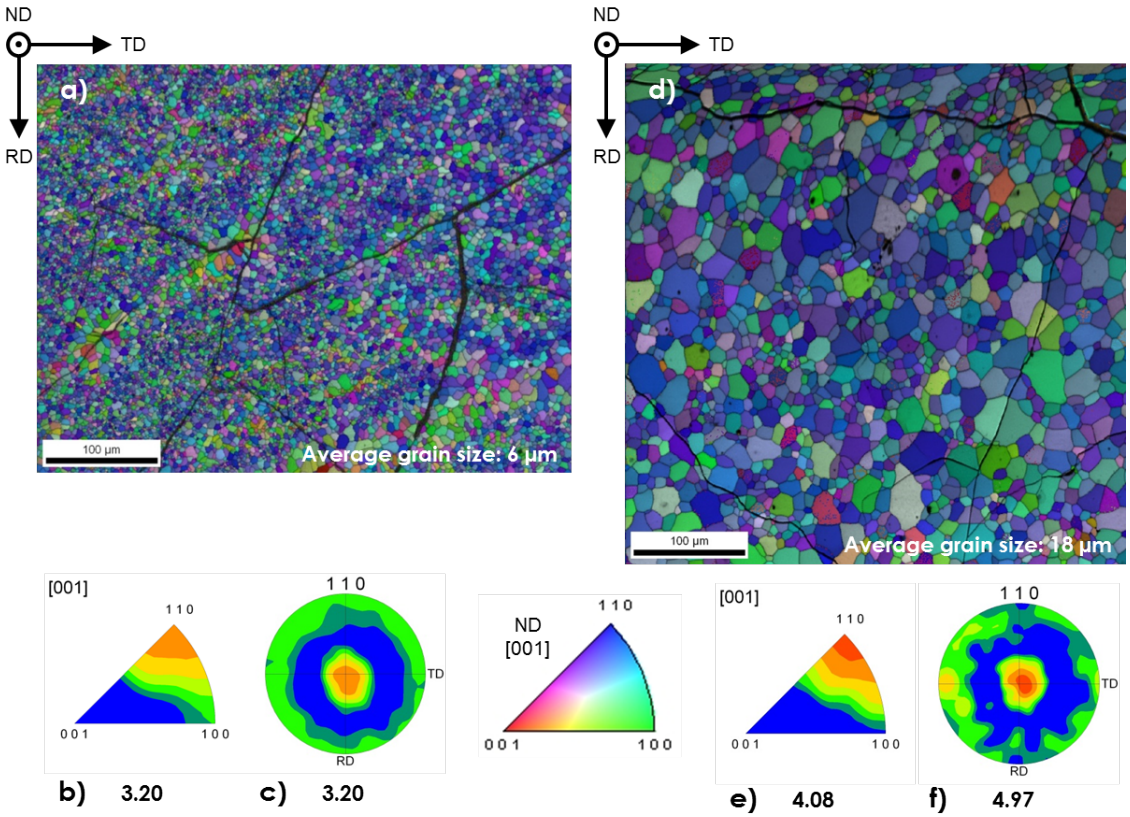

Figure 3.23: *IPF and 110 PF for as-spun flake (a, b and c) and thermal treated flake at 1000°C during 7 days (d, e and f) where respectively more than 8000 and 1000 grains are analyzed. The average grain growth (from 6 to 18 µm) is correlated to an increase of the maximum of pole figures 110 (orange to red) from 3.20 to 4.97. In addition, from crystal direction map analysis the area fraction of (110) planes at the surface is increased of 5% after thermal treatment. It is important to note that when we measure the texture after grain growth, we have fewer grains contributing to the texture spread so it can introduce a bias in the orientation distribution and give the impression of a stronger texture. To avoid this artefact, we have increased the sampling so we are confident with the veracity of texture enhancement during annealing.*

3.4 Conclusion

In this work, we have fabricated <110> grain oriented $MnSi_{1.73}$ bulk materials by consolidation of anisotropic flakes produced by melt-spinning. Due to the high cooling rate experienced by the melt during melt-spinning, the formation of secondary phases classically observed in casted samples (see chapter 2) is strongly limited, leading to fully dense and highly pure bulk HMS materials with clean grain boundaries, and free of MnSi striations. In melt-spun flakes, the mixture of commensurate HMS phases formed during rapid solidification is shifted towards short c-axis length compared to the arc melting route. After consolidation by SPS the incommensurable character of the bulk HMS materials is also confirmed.

The crystallographic texture of the melt-spun flakes and the consolidated compacts was characterized by EBSD. For the flakes, the fiber-like texture of the (110) planes results from solidification of undercooled melt proceeding with preferential growth in the <110> crystallographic direction. After consolidation of stacked flakes by spark plasma sintering, the texture is retain but weaken in the compacts.

The resulting crystallographic texture will permit to measure the transport perpendicular to the <001> direction (perpendicular to c-axis) and in plane (001) which provide a mean to evaluate, for the first time, the effect of grain orientation by it-self (without the influence of MnSi striations (see figure 3.24). However, we will not have access to the thermoelectric properties parallel to c-axis. These points, as well as the influence of the various process on the transport properties of HMS, will be addressed in the next chapter.

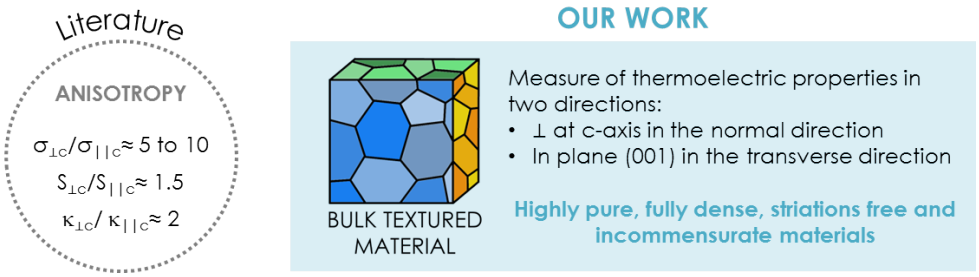

Figure 3.24: *Anisotropy study in HMS alloys.*

Bibliography

[1] I. Engstrom and B. Lonnberg. Thermal expansion studies of the group iv-vii transition-metal disilicides. *Journal of Applied Physics*, 63(9):4476–4484, 1988.

[2] A.A. Baikov L.D. Ivanova. Higher manganese silicide based materials. *Journal of Thermoelectricity*, 3:60–66, 2009.

[3] H Kaga, Kinemuchi Y., and Watari K. Fabrication of c-axis oriented higher manganese silicide by a high-magnetic-field and its thermoelectric properties. *Journal of Materials Research*, 22:2917–2923, 2007.

[4] I. Kawasumi, M. Sakata, I. Nishida, and K. Masumoto. Crystal growth of manganese silicide, $mnsi_{1.73}$ and semiconducting properties of $mn_{15}si_{26}$. *Journal of Materials Science*, 16(2):355–366, 1981.

[5] Y. Sadia, Z. Aminov, D. Mogilyansky, and Y. Gelbstein. Texture anisotropy of higher manganese silicide following arc-melting and hot-pressing. *Intermetallics*, 68:71–77, January 2016.

[6] G. Zwilling and H. Nowotny. Crystal structure of manganese silicides with $mnsi_{1.7}$ stoichiometry. *Monatshefte fur Chemie*, 102(3):672–677, 1971.

[7] G. Zwilling and H. Nowotny. Anisotropy of the electrical conductivity of $mn_{27}si_{47}$. *Monatshefte fur Chemie*, 105(4):666–670, 1974.

[8] R. Srinivasan, K. McReynolds, N. W. Gothard, and J. E. Spowart. Texture development during deformation processing of the n-type bismuth telluride alloy $bi_2se_{0.3}te_{2.7}$. *Materials Science and Engineering: A*, 588:376–387, December 2013.

[9] J. Goldsmid G.S. Nolas, J. Sharp. *Thermoelectrics-Basic Principles and New Materials Developments*, volume 45. Springer-Verlag Berlin Heidelberg, 2001.

[10] D.L. Medlin and G.J. Snyder. Interfaces in bulk thermoelectric materials: A review for current opinion in colloid and interface science. *Current Opinion in Colloid & Interface Science*, 14(4):226–235, August 2009.

[11] W. Luo, H. Li, Y. Yan, Z. Lin, X. Tang, Q. Zhang, and C. Uher. Rapid synthesis of high thermoelectric performance higher manganese silicide with in-situ formed nano-phase of mnsi. *Intermetallics*, 19(3):404–408, March 2011.

[12] W. Luo, H. Li, F. Fu, W. Hao, and X. Tang. Improved thermoelectric properties of al-doped higher manganese silicide prepared by a rapid solidification method. *Journal of Electronic Materials*, 40(5):1233–1237, 2011.

[13] S. Gorsse, G. Orveillon, O.N. Senkov, and D.B. Miracle. Thermodynamic analysis of glass-forming ability in a ca-mg-zn ternary alloy system. *Physical Review B*, 73(22):224202, 2006.

[14] S. Gorsse, B. Chevalier, and G. Orveillon. Magnetocaloric effect and refrigeration capacity in gd60al 10mn30 nanocomposite. *Applied Physics Letters*, 92(12), 2008.

[15] W. Xie, S. Wang, S. Zhu, J. He, X. Tang, Q. Zhang, and T. M. Tritt. High performance bi_2te_3 nanocomposites prepared by single-element-melt-spinning spark-plasma sintering. *Journal of Materials Science*, 48(7):2745–2760, 2013.

[16] C. Yu, T.-J. Zhu, K. Xiao, J.-J. Shen, S.-H. Yang, and X.-B. Zhao. Reduced grain size and improved thermoelectric properties of melt spun (hf,zr)nisn half-heusler alloys. *Journal of Electronic Materials*, 39(9):2008–2012, 2010.

[17] P.M. De Wolff. The pseudo-symmetry of modulated crystal structures. *Acta Crystallographica Section A*, 30(6):777–785, 1974.

[18] A. S. Orekhov and F. Y. Solomkin. Sem/eds/ebsd study of the behaviour of ge, mo and al impurities in complex-doped crystals of higher manganese silicide. *Journal of Physics: Conference Series*, 471(1):012016, 2013.

[19] V. I. Tkatch, A. I. Limanovskii, S. N. Denisenko, and S. G. Rassolov. The effect of the melt-spinning processing parameters on the rate of cooling. *Materials Science and Engineering: A*, 323:91–96, January 2002.

[20] C. Chattopadhyay, S. Sangal, and K. Mondal. A relook at the preferred growth direction of the solid-liquid interface during solidification of pure metals. *Acta Materialia*, 58(16):5342–5353, 2010.

[21] B. Chalmers F. Weinberg. Further observations on dendritic growth in metals. *Canadian Journal of Physics*, 30(5):488–502, 1952.

[22] S. O'Hara. Controlled growth of tin dendrites. *Acta Metallurgica*, 15(2):231–236, 1967.

[23] F.J. Humphreys and M. Hatherly. *Recrystallization and related annealing phenomena*. Elsevier, 2004.

[24] D.W. Bainbridge, H.L. Choh, and E. H. Edwards. Recent observations on the motion of small angle dislocation boundaries. *Acta Metallurgica*, 2(2):322–333, 1954.

Chapter 4

Thermoelectric properties

In this chapter, we present and discuss the transport properties (Seebeck coefficient, thermal and electrical conductivities) of the pure HMS and Ge-doped materials produced from the manufacturing routes developed in chapters 2 and 3. For commodity reasons, they are summarized in table 4.1. All these materials are fully dense, highly pure, and present a homogeneous microstructure consisting in the single incommensurate HMS phase. They differ only by the manufacturing route, the doping and the texture.

The first section presents the experimental procedure used to measure the transport properties.

In the second section, we use properties charts to appreciate how particular parameters and manufacturing processes influence the properties of HMS materials.

Manufacturing process	**Liquid phase route**				**Solid state route**
Name	AC	GI	MS	MSO	RS
Description	As-cast ingots produced by arc-melting	Materials produced by SPS consolidation of ground ingots	Materials produced by densification of ground melt-spun flakes	Textured materials obtained by consolidation of stacked melt-spun flakes	Materials produced by reactive sintering of MnSi and Si powders during consolidation in the SPS
Related chapter	2	2	3	3	2

Table 4.1: *Recap of the studied materials obtained from liquid phase processes (arc-melting and melt-spinning) and solid-state synthesis (reactive sintering).*

4.1 Experimental procedure

Power factor The Power Factor (PF=$S^2\sigma$ in W/m.K) was measured on rectangular bars of 3*3*7 mm^3 size (ZEM-3, Ulvac GmbH) where the electrical conductivity and the Seebeck coefficient are simultaneously measured under helium atmosphere. A switching technique of four-point direct current gives the electrical conductivity and a static direct current method based on the slope voltage versus temperature-difference curves measures the Seebeck coefficient.

Thermal conductivity The thermal conductivity is calculated thanks to the following relationship: $\kappa = \rho\alpha C_p$ where ρ is the density (kg.m^{-3}) measured by Archimedes principle, α the thermal diffusivity (m^2.s^{-1}) is measured by Laser Flash diffusivity (LFA 457, Netzsch) under argon and C_p the heat capacity (J.kg^{-1}.K^{-1}) measured by Differential Scanning Calorimetry (DSC 850 PerkinElmer) under argon.

C_p was measured on ground undoped materials sintered at 1100°C from arc-melting and melt-spinning routes and compared to the data of the literature (see figure 4.1). We can see that our results are in agreement with both experimental and theoretical values. In addition, we confirm the independence of the C_p with respect to the process (i.e. the microstructure).

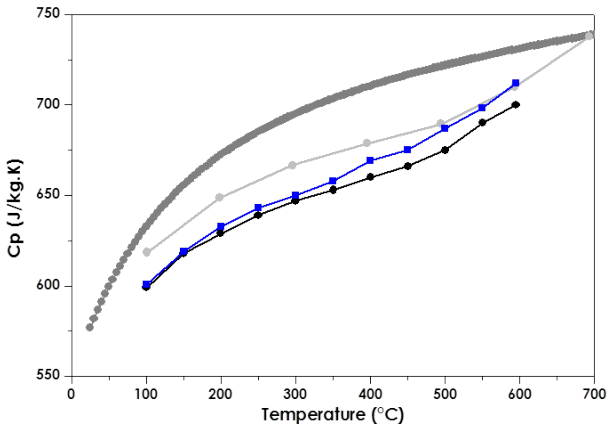

Figure 4.1: *C_p values for ground materials from arc-melting (black circle) and melt-spinning (blue square) routes sintered at 1100°C. Experimental (light gray) [1] and theoretical (dark gray) [2] C_p values from the literature are also reported.*

Stacked compacts In order to characterize the stacked compacts obtained after SPS in the two directions several cuts are performed and shown on figure 4.2.

Squares of 6x6 mm² and ∼1 mm of thickness were cut to measure the thermal conductivity. A rectangular bar was extracted from the middle of the previous squares to measure the electronic transport properties. The blue part was used to investigate the microstructural parameters.

Due to the measurement setup, the power factor and the thermal conductivity for one direction need to be measured in a different cut. Thus, the cut in the normal direction (parallel to the stacking of the ribbons) will permit to measure the $\kappa \perp$ to c-axis and power factor in plane (001) and the cut in the transverse direction the measurement of the two complementary κ in plane (001) and power factor $\perp$ to c-axis.

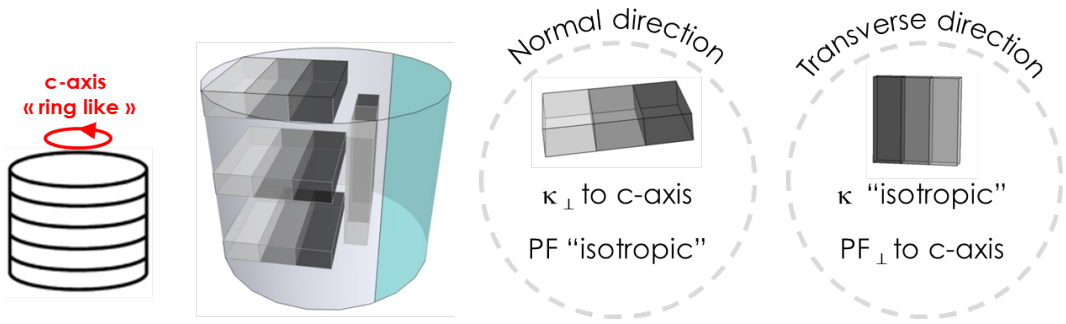

Figure 4.2: *Sample cuts for thermoelectric measurements on stacked compacts. The normal direction allows the measurement of $\kappa \perp$ to c-axis and power factor (PF) in plane (001) meanwhile the transverse cut leads to κ in plane (001) and power factor (PF) $\perp$ to c-axis.*

Starting powders The ground materials are made from densified powders issued from arc melted ingots and as-spun flakes. The reactive sintered materials are obtained from a densified mixture of MnSi and Si/(Si,Ge) powders.

The MnSi alloy was prepared by arc melting technique and the powder XRD pattern confirms the synthesis of pure MnSi compound obtained from the melt through congruent melting point (see figure 4.3).

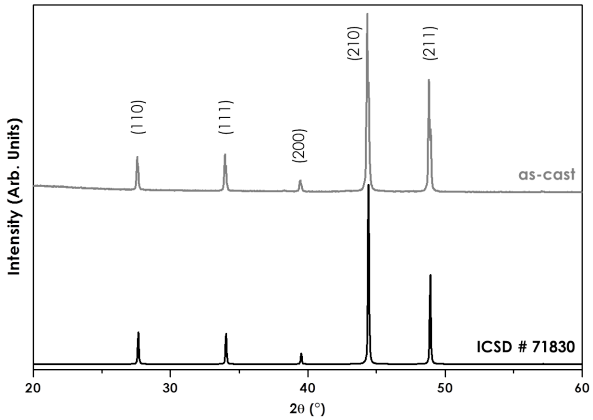

Figure 4.3: *Powder XRD patterns: theoretical (ICSD # 71830) and as-cast for MnSi compound showing a pure synthesis.*

Figure 4.4 presents the morphology of the four starting powders after the sieving step (40 µm). For all the powders, angular shape due to the brittle mechanical comportment of the ingots and flakes is observed and a rough estimation leads to a particle range from tens of µm to hundreds of nanometers.

Laser granulometry (Mastersizer 2000, Malvern) was used to get an accurate characterization of the powders (see figure 4.5). The detection limit of the equipment is 50 nm. The distribution width is defined by three values D10, D50 and D90. The D50, median, represents the diameter where half of the population lies below this value. Similarly, D10 and D90 are respectively the limits for 10 and 90 percent of the population. The volume distribution shows a non-symmetric and monomodal distribution for the powders from $MnSi_{1.73}$ flakes, Si and MnSi ingots with a shoulder at low values and average sizes respectively around 27, 14 and 21 µm. Powder from $MnSi_{1.73}$ ingot present a bimodal distribution with two main contributions respectively around 2 and 40 µm. The distribution of sizes ranges from 300 nm to 80 µm for the four powders. The converted results in number distribution showed that the majority of the particles are down to 2 µm (brittle mechanical behavior).

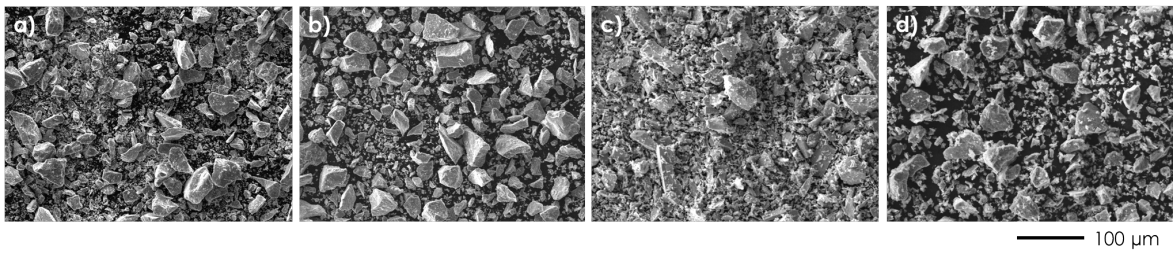

Figure 4.4: *SE images of ground $MnSi_{1.73}$ ingot (a), $MnSi_{1.73}$ flakes (b), MnSi ingot (c) and pure commercial Si (d). The powders after sieving (40 µm) exhibit angular shape.*

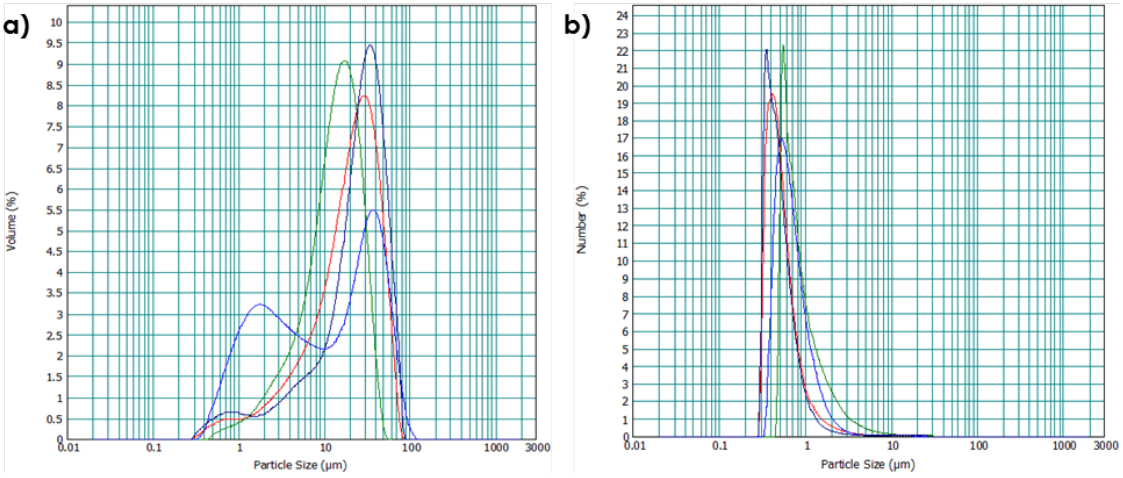

Distribution (µm)	D10	D50	D90
$MnSi_{1.73}$ ingot	1.1	10.4	50.9
$MnSi_{1.73}$ flakes	3.9	26.7	54.3
MnSi	3.7	13.8	29.0
Si	3.8	21.1	46.9

Distribution (µm)	D10	D50	D90
$MnSi_{1.73}$ ingot	0.4	0.6	1.2
$MnSi_{1.73}$ flakes	0.3	0.5	0.8
MnSi	0.5	0.8	1.9
Si	0.3	0.5	0.9

Figure 4.5: *Particles size distribution in volume (a) and number (b) of powders from $MnSi_{1.73}$ ingot (blue), $MnSi_{1.73}$ flakes (purple), MnSi ingot (green) and pure commercial Si (red) after sieving (40 µm). D10, D50 and D90 values (µm) for each powder are presented above the curves for the volume and number distributions.*

4.2 Results

4.2.1 Transport properties and thermal behavior

Figure 4.6 shows the thermal dependence of the transport properties of HMS materials studied in chapters 2 and 3. They all behave as degenerated semiconductors. For the electrical conductivity and the Seebeck coefficient opposite trends are classically observed, with an increase of the Seebeck with temperature and a decrease for the electrical conductivity. For these two properties the bipolar effect is observed around 500°C. At low temperature due to phonon-phonon scattering the thermal conductivity decreases whereas after 500°C the thermal conductivity increases due to the bipolar effect (creation of electron/hole pairs).

From the literature data the reported transport properties around 500°C range as follows:

- thermal conductivity from 1.7 to 3.5 W/m.K.
- electrical conductivity from 1.4 10^4 to 4.7 10^4 S/m.
- Seebeck coefficient from 1.9 10^{-4} to 2.4 10^{-4} V/K.

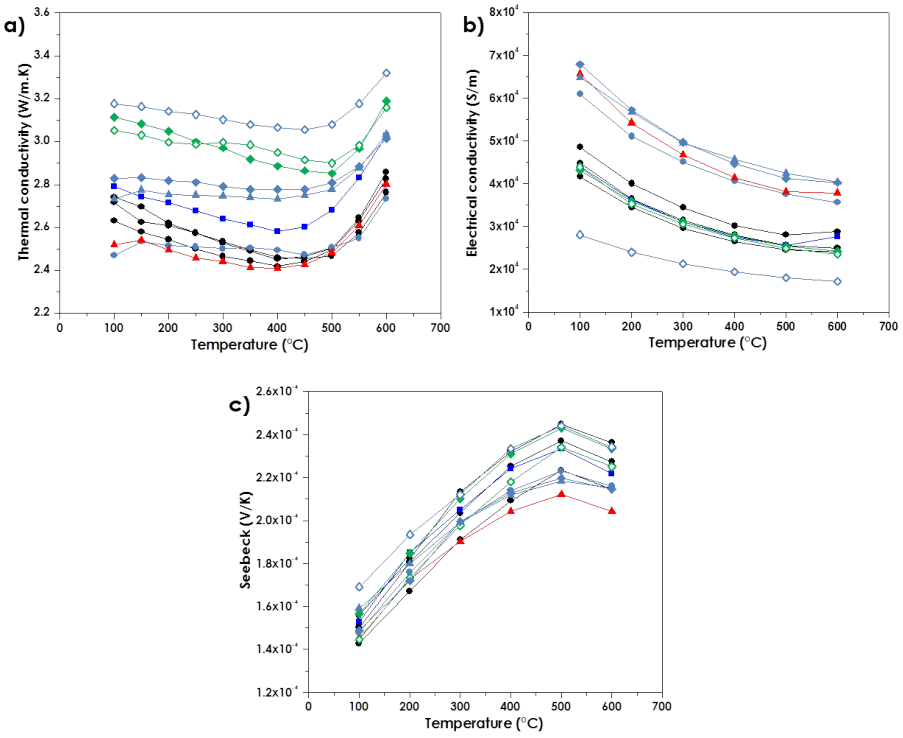

Figure 4.6: *Thermal dependencies of the thermal conductivity (a), electrical conductivity (b) and Seebeck coefficient (c) for the materials investigated during thesis.*

Our values stand in the literature ranges and span from 2.5 to 3.1 W/m.K for the thermal conductivity, from 1.8 10^4 to 4.1 10^4 S/m for the electrical conductivity and from 2.1 10^{-4} to 2.4 10^{-4} V/K for the Seebeck coefficient. Hole dominant carrier behavior providing the p-type conduction (i.e. positive Seebeck coefficient) is confirmed. As observed in the literature, for HMS based alloys the highest variability is observed for the electrical conductivity.

4.2.2 Power factor/thermal conductivity trade-offs

In this section, we use property charts to appreciate how particular parameters and manufacturing processes influence the properties of HMS materials. The chart shows always two set of properties: the power factor - which is the product of the square of the Seebeck coefficient and the electrical conductivity (numerator of the figure of merit zT) - is plotted against the thermal conductivity (denominator of zT). As explained in chapter 1, the positions occupied by the materials on the charts illustrate their performance as the figure of merit increases from the bottom right to the upper left corner. In addition of our materials, we have represented the results from the literature. A total of 30 HMS-based alloys gives the ranges of properties for this class of thermoelectric materials.

We have classified the ways the properties change into 3 categories:

- **Microstructure** to illustrate the effect of porosities and secondary phases.
- **Process and doping** to compare how the liquid-phase and solid state (reactive sintering) processes enable to manipulate the properties, and how Ge doping change the property profiles.
- **Texture and doping** to explore the true intrinsic anisotropy of HMS.

Microstructure

Except in the work Bernard-Granger *et al.* [1] from which HMS compacts with high relative densities (99.8%) were obtained, the literature data give thermoelectric properties measured on samples exhibiting either an important amount of porosities (relative densities ranging between 75 and 97%) and/or a significant amount of secondary phases (MnSi, Si), making quite hazardous the evaluation of the intrinsic transport properties of HMS and the explore of the underlying physics controlling the properties.

In an attempt to tie it all together, we have measured the transport properties of compacts exhibiting various amount of porosities and impurities. They were prepared by the manufacturing routes

described in chapter 2 by tuning the sintering temperature (from 950°C to 1100°C) and the nominal alloy composition (γ=1.73, 1.75 and 1.77). The results are plotted on figure 4.7. The arrows illustrate the pathways followed when the relative density increases (in red) and when the amount of secondary phase decreases (in black).

We can conclude that the best material is obtained for the highest density and the lowest impurity content which result from the following conditions: 1100°C for the sintering temperature and γ=1.73 for the nominal composition (see figure 4.8). Such a trend is not a big surprise but it nicely illustrates the great sensitivity of the power factor towards both porosity and impurities whereas the thermal conductivity changes only slightly. It also shows that consolidation of the as-cast ingots is a mandatory step as the important amount of impurity and porosity in the solidified microstructures moves the power factor and the resulting zT far downwards.

In the case of undoped materials, the best zT of 0.43 at 500°C is obtained for the ground compact $MnSi_{1.73}$ densified at 1100°C. This set of composition (γ=1.73) and sintering temperature (1100°C) provides highly pure and fully dense HMS materials as shown in chapter 2.

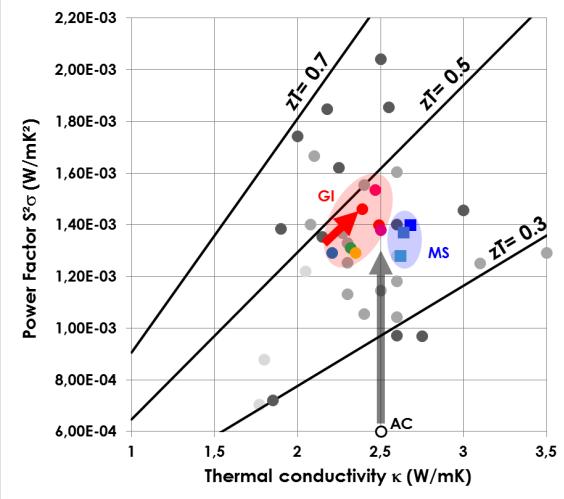

Figure 4.7: *Thermoelectric material property chart at 500°C. Ground ingots (GI) with nominal composition $MnSi_{1.73}$ as a function of the dwell temperature: 950°C (in blue), 1000°C (in green), 1050°C (in orange) and 1100°C (in red). Materials with different nominal compositions (γ=1.73, 1.75 and 1.77) are represented for GI (circles: red for 1.73, pink for 1.75 and purple for 1.77) and MS (squares: dark blue for 1.73, medium blue for 1.75 and light blue for 1.77). The properties of an as-cast (AC) $MnSi_{1.73}$ material presenting cracks are also reported. The data from the literature for doped (in dark gray), undoped (in medium gray) and composites (in light gray) materials are reported.*

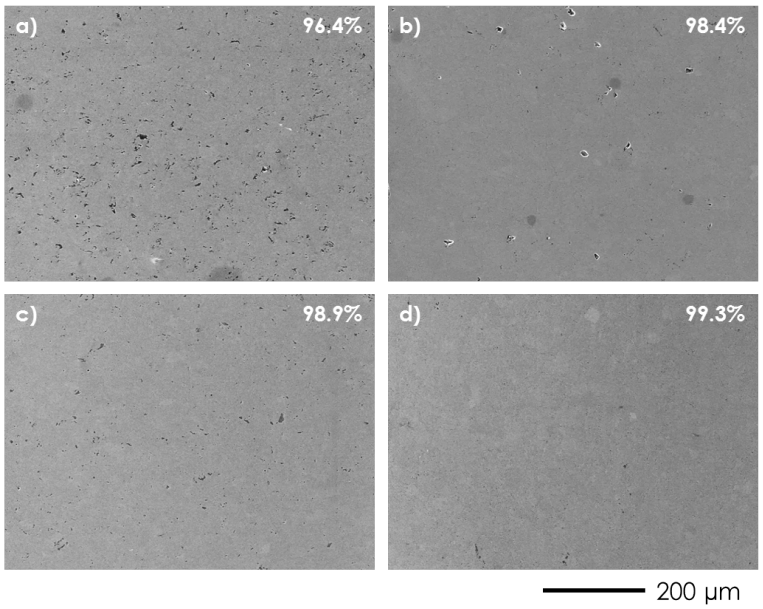

Figure 4.8: *SE images and their relative density for GI materials as a function of the SPS dwell temperature: 950°C (a), 1000°C (b), 1050°C (c) and 1100°C (d). The density of the materials is measured by Archimedes principle and the relative density is calculated from theoretical density of 5.159 g/cm^3 for HMS.*

Undoped material produced by SPS consolidation of ground ingot with nominal composition $MnSi_{1.73}$ presents a zT=0.43 at 500°C.

Process and doping

Figure 4.9.a. compares the performances of HMS alloys as a function of the processes. The new route (so called reactive sintering) developed in the chapter 2 were HMS alloys have been produced by solid-state diffusion between MnSi and Si particles exhibit an improvement of 23% in zT compared to classical liquid-phase processes, i.e. zT=0.53 at 500°C, one of the best for undoped samples of the state-of-art.

In addition, the improvement of the performances for Ge-doped HMS alloys (with nominal composition $Mn(Si_{0.992}Ge_{0.008})_{1.73}$) for doped ingots and MnSi/(Si,Ge) reactive sintering is presented on figure 4.9.b. For the liquid-phase process route an improvement of 32% in zT is reached whereas for the reactive sintering route this improvement is limited at 6% in zT due to the presence of MnSi residual primary particles (already evidenced in chapter 2) which adversally increase the thermal conductivity.

However, it is reasonable to expect a potential zT of 0.63 for Ge-doped reactive sintered materials if the reaction is complete, reaching to the best materials of the state-of-art.

By comparison of our doped samples with the literature we can observe that a similar zT of 0.58 is achieved by Zhou *et al.* [3] for the same Ge nominal composition. They produce the Ge-doped materials through induction melting followed by Hot Pressing at 900°C during 60 min. Since no relative density is reported and looking at the low value of the thermal conductivity this sample might contain a non negligible amount of porosities. From the point of view of the application (design requirements) an high electrical conductivity is preferred at equiperformant zT, hence our results match with this trend (3.8 10^4 S/m compared to 3.0 10^4 S/m for Zhou *et al.* [3]) so we believe that rationalizing processes and doping effects will support efficient thermoelectric development.

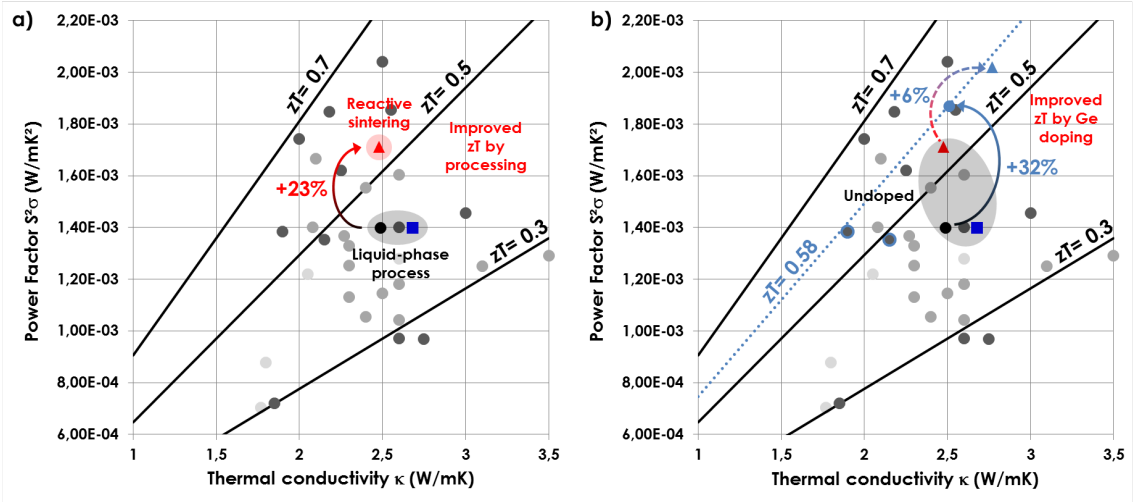

Figure 4.9: *Thermoelectric material property charts at 500°C. Comparison between liquid-phase processes (black circle:GI and blue square:MS) and reactive sintering (RS) (red triangle) routes (a). Comparison between* $Mn(Si_{0.992}Ge_{0.008})_{1.73}$ *materials from GI (blue circle) and RS MnSi/(Si,Ge) (blue triangle) process (b). The data from the literature for doped (in dark gray), undoped (in medium gray) and composites (in light gray) materials are reported. The Ge-doped samples from the literature are highlighted with a blue contour.*

As shown in figures 4.10 and 4.11, the reactive sintering process and the Ge additions move upwards the zT compared to the liquid-phase process and the undoped materials, respectively, mainly because the electrical conductivity is enhanced whereas the others properties do not change significantly. Electrical conductivity is governed by the concentration and the mobility of the charge carriers, the first one can be affected by solutes (doping/alloying elements) and the second by both the solutes and the microstructure. With respect to the effect of the manufacturing route, in the absence of Hall measure-

ments, we can reasonably suppose that the observed changes reflect the sensitivity of the hole mobility to the microstructure, i.e. the charge carriers can be scattered by obstacles such as precipitates and grain boundaries.

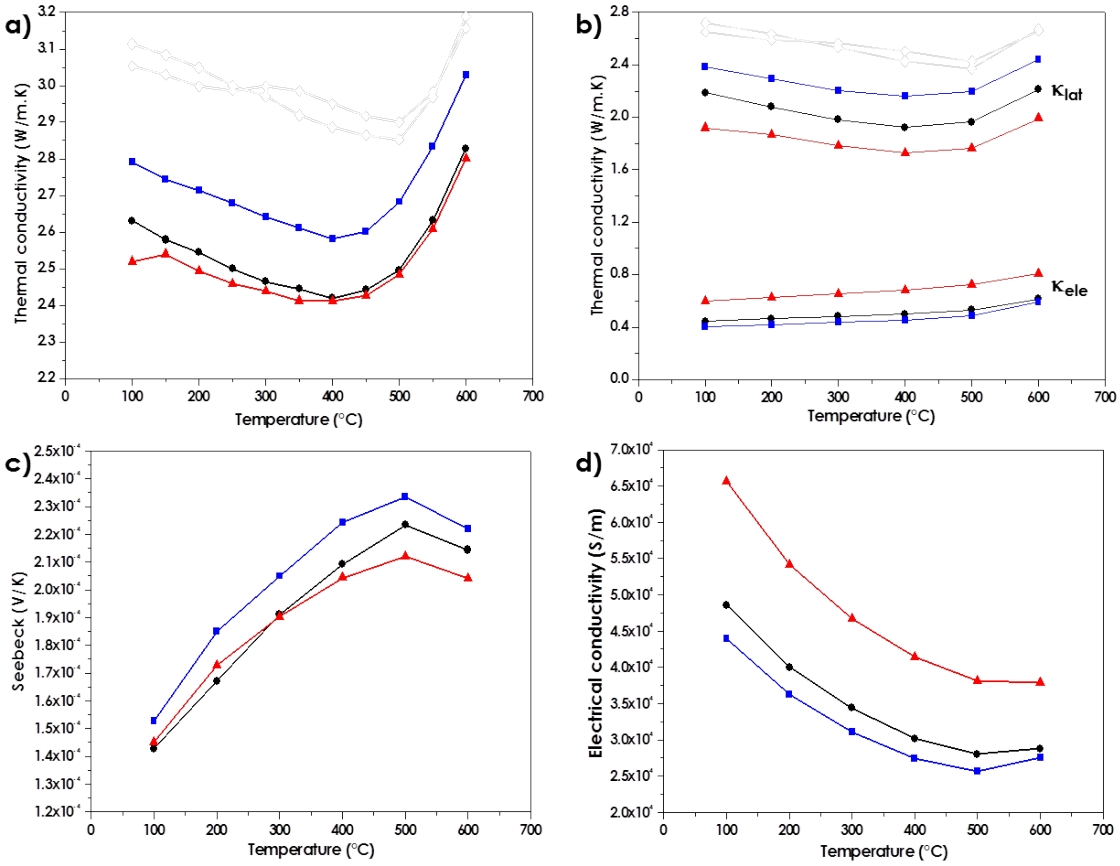

Figure 4.10: *Total thermal conductivity (a), electronic (K_{ele}) and lattice (K_{lat}) thermal contributions to the thermal conductivity (b), Seebeck coefficient (c) and electrical conductivity (d) for undoped $MnSi_{1.73}$ materials from GI (black circle), RS MnSi/Si (red triangle) and MS (blue square).*

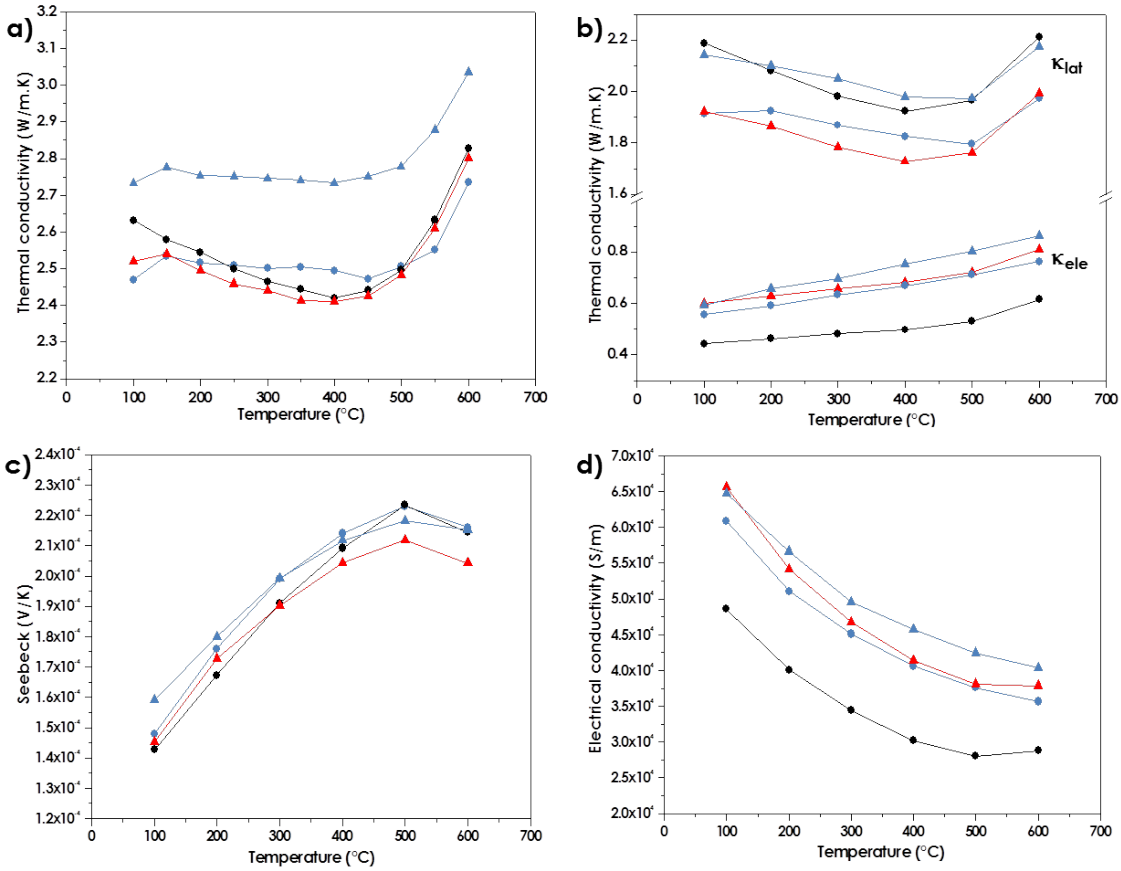

Figure 4.11: *Total thermal conductivity (a), electronic (K_{ele}) and lattice (K_{lat}) thermal contributions to the thermal conductivity (b), Seebeck coefficient (c) and electrical conductivity (d) for $Mn(Si_{0.992}Ge_{0.008})_{1.73}$ materials (light blue) obtained from GI (circle) and RS MnSi/(Si,Ge) (triangle). Undoped materials obtained from GI and RS are also reported with black circle and red triangle, respectively.*

As shown in chapter 2 and figures 4.12 and 4.13, the only distinguishing parameters between materials issued from liquid-phase and reactive sintering routes are the amount and neatness of the grain boundaries. In reactive sintered materials, grain boundaries present less porosity and Si impurities, so the density of the scattering centers is decreased. With respect to the effect of Ge, it is either attributed to a change of the density number of MnSi striations or to an increase of the carrier concentration [4, 3, 5]. The first mechanism can be understood as the scattering effect of the microstructure (platelet precipitates) and the second as a doping effect. We can now clarify this point since the property measurements have been performed on doped and undoped samples having the same microstructure, i.e. homogeneous and free of MnSi striations in all cases. Our results suggest that the enhancement of the electrical conductivity of HMS with Ge addition is more likely due to an increase of the carrier

concentration. Since Ge is electroneutral for HMS, its positive effect was interpreted from first principle calculations as the reflect of changes in the density of states near the Fermi level due to disruption of the Si helices [4].

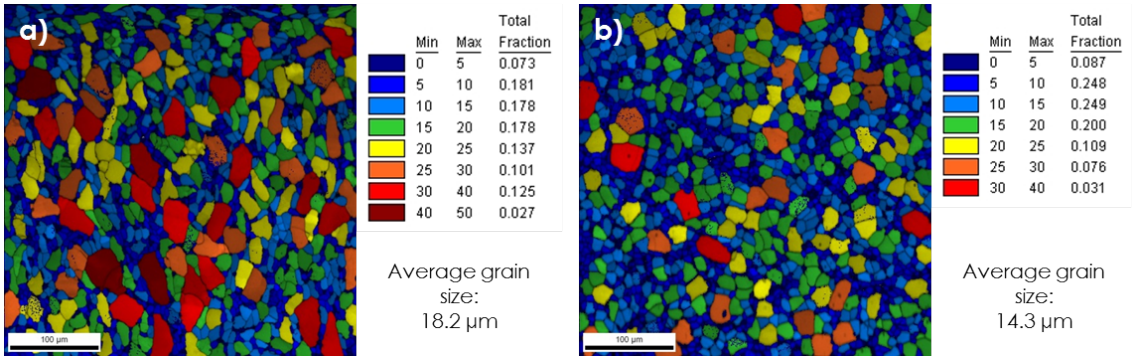

Figure 4.12: *Grain size map, area fractions and average grain size for GI (a) and RS (b) materials. The colored scale highlights the grain size distribution from 0 to 50 µm.*

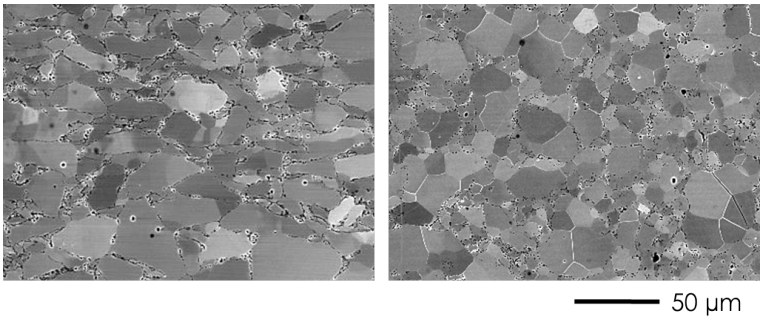

Figure 4.13: *BSE images for the GI (a) and RS (b) materials.*

Reactive sintering process is leading to one of the best zT (0.53 at 500 °C) for undoped materials with an innovative cost saving process, consistent with automotive design requirements.
Ge doping is effective in increasing the performance (zT=0.58 for liquid-phase process), however an optimization is needed to further increase the zT for Ge-doped solid-state route.

Texture and doping

Figure 4.14 shows the positions occupied by the crystallographically textured $MnSi_{1.73}$ material, and the concomitant effect of Ge-doping (0.8 at.%), in the thermoelectric properties chart.

Very surprisingly, the undoped sample exhibit approximatively the same properties in the nor-

mal and transverse direction (respectively, perpendicular to the c-direction and in-plane), whereas we observe a tremendous effect of the grain orientation in Ge-doped samples having similar texture strength:

- zT=0.27 is obtained in the quasi-isotropic direction
- zT=0.53 in the direction $\perp$ to c-axis

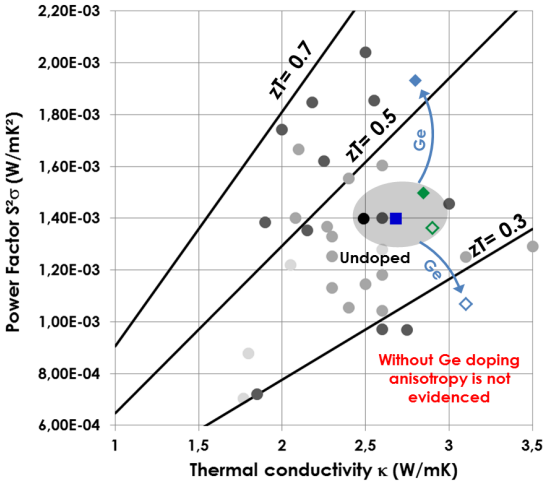

Figure 4.14: *Thermoelectric material property chart at 500°C. $MnSi_{1.73}$ (green diamond) and $Mn(Si_{0.992}Ge_{0.008})_{1.73}$ (light blue diamond) MSO materials. The properties measured in the direction $\perp$ to c-axis are associated to filled diamond and the ones in plane direction with open diamond. The data from the literature for doped (in dark gray), undoped (in medium gray) and composites (in light gray) materials are reported.*

As shown in figure 4.14, the properties measured on grain oriented samples in the direction perpendicular to c-axis and in-plane (quasi-isotropic) suggest that HMS exhibit a high degree of transport properties isotropy. This is in contradiction with what is claimed in the literature.

From a careful review of the available literature data the anisotropy in transport properties in HMS alloys is reported in 8 papers from which 6 are dealing with single crystals where the presence of MnSi striations are reported [6, 7, 8, 9, 10, 11, 12, 13]. As a consequence the measurement of the thermoelectric properties perpendicular and parallel to the c-axis are influenced by the presence of such oriented plate-like metallic precipitates in HMS that are sufficient to induce anisotropy, as suggested by Levinson [6]. In addition, Ivanova *et al.* highlighted that a strong reduction of the anisotropy is observed in Ge-doped single crystals [9]. As previously shown in chapter 2 the Ge microsubstitution was effective in preventing the formation of MnSi striations. Thus, the fact that the Ge-doped single

crystals are becoming isotropic is an additional argument to prove that the claimed anisotropy of HMS is due to the presence MnSi striations. This statement is supported by Engstrom *et al.* work [11] where most of Silicides alloys present isotropic properties. It is clear that no study has measured the intrinsic properties of HMS phase in the directions perpendicular and parallel to c-axis, it was always the properties from a lamellar composite HMS/MnSi.

We end with two papers that have reported the anisotropy of the properties in bulk textured materials [12, 13]. In a work recently published [13], the authors report an enhancement of about 10% of the zT value of HMS compacts in the direction parallel to the pressing direction compared to the transverse direction. Despite the lack of EBSD analysis, it was claimed from XRD patterns a preferred crystallographic orientation in parallel to the pressing direction. This assumption is very speculative so we tried to reproduce their results. Figure 4.15 shows the microstructure of HMS compacts obtained from consolidation of ground ingots. As shown by the EBSD analysis, the material thus obtained does not present any crystallographic texture.

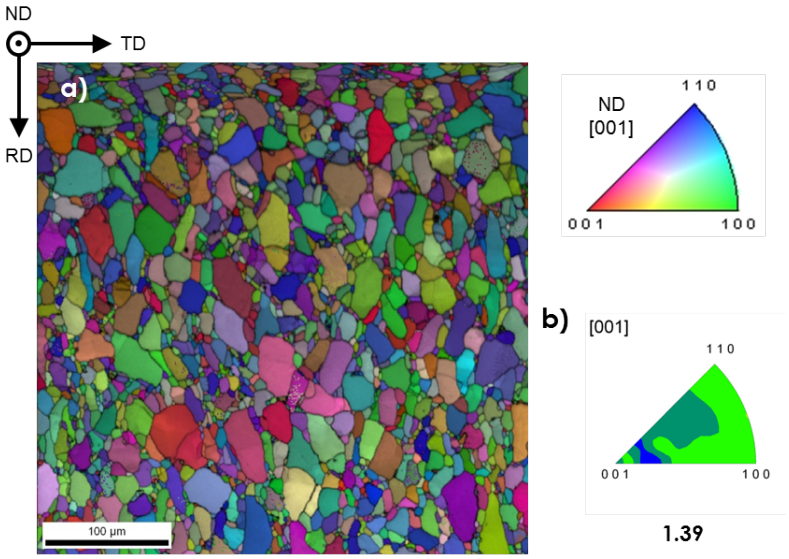

Figure 4.15: *IQ+IPF map (a) and IPF [001] (b) of the GI material in the normal direction. More than 1500 grains are analyzed. The texture is normalized on a scale of 5 and the maximum of texture is indicated above the IPF.*

Unlike texture undoped HMS, grain oriented Ge-doped HMS samples show a higher electrical conductivity perpendicular to the c-direction compared to the in plane direction while the Seebeck coefficient and the thermal conductivity are almost independent of the texture (see figure 4.16). From our best knowledge it is the first time that such unique characteristic, in which the relationship between

the crystallographic texture and the transport properties is expressed only through doping. The lack of orientation dependence we observed for pure HMS has evidenced the isotropy of the transport properties of this compound, so the origin of the texture dependence for doped samples must have another origin.

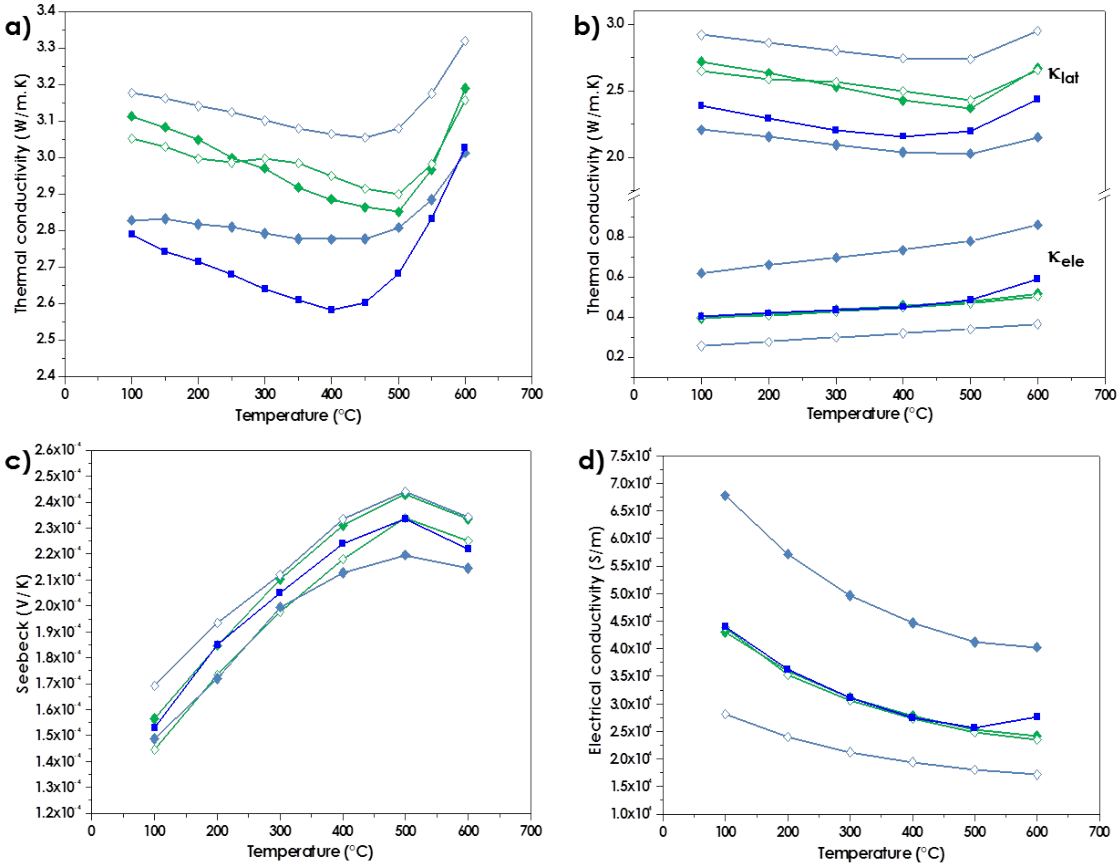

Figure 4.16: *Total thermal conductivity (a), electronic (K_{ele}) and lattice (K_{lat}) thermal contributions to the thermal conductivity (b), Seebeck coefficient (c) and electrical conductivity (d) for undoped $MnSi_{1.73}$ (green diamond) and $Mn(Si_{0.992}Ge_{0.008})_{1.73}$ (light blue diamond) MSO materials. The properties measured in the direction $\perp$ to c-axis are associated to filled diamond and the one in plane with open diamond. Undoped material from MS route and presenting isotropic properties is reported (blue square).*

Several papers show that texture can drastically alters the grain boundary misorientation distribution [14, 15]. Garcia *et al.* [14] have studied the relationship between crystallographic texture and grain boundary character. They established that fiber-like textured samples (as it is the case for our textured HMS materials) exhibit a high density of low-angle misorientations while random materials have a high probability of large-angle misorientation. Moreover, the anisotropy of the grain boundary

segregation is a phenomena that has been reported for long time [16, 17]. Several studies also evidenced that the segregation occurs preferentially more at high-energy boundaries than low-energy ones [18, 19]. Finally, since the grain boundary energy depend on the grain boundary character, one can expect that crystallographic texture may induce a selective segregation, and thus create percolative paths for charge carrier in specific directions. Experimental investigations combining maps of grain boundary misorientations and 3D atomic maps would be useful to verify this scenario (see for example Herbig *et al.* [20]), and to this respect, our grain oriented samples offer a reliable mean to evaluate the effect of the grain boundary texture on the thermal and electronic transport properties.

For undoped highly pure textured bulk materials that do not present MnSi striations the anisotropy in the transport properties is not observed.

For Ge doped textured compact a strong splitting is observed between the two directions.

4.3 Conclusion

We have characterized the transport properties and evaluated the thermoelectric performance of pure and Ge-doped HMS materials produced via different manufacturing processes. Using property charts to track the material pathways, we have outlined and discussed the effect of the microstructure, process, doping and texture of the transport properties of HMS. It has been shown that our materials compete well with the state-of-the-art (best zT=0.67 at 500°C for Al-doped $MnSi_{1.75}$ prepared by gas atomization process followed by SPS consolidation).

We have reported that for crystallographically textured HMS materials, the relationship between texture strength and electrical conductivity showed a unique behavior in which the electrical conductivity is independent of the grain orientation for pure (undoped) HMS while it becomes highly sensitive for Ge-doped HMS. Adequate analysis of the grain boundary texture and segregation is required to gain a better understanding of the underlying physic controlling the link between crystallographic texture, doping and transport properties. Nevertheless this study opens up new directions for enhancing the thermoelectric properties through the interplay between texture (control of the grain boundary character) and doping (leading to segregation), i.e. engineering of the anisotropy of the grain boundary segregation.

Bibliography

[1] G. Bernard-Granger, M. Soulier, H. Ihou-Mouko, C. Navone, M. Boidot, J. Leforestier, and J. Simon. Microstructure investigations and thermoelectrical properties of a p-type polycrystalline higher manganese silicide material sintered from a gas-phase atomized powder. *Journal of Alloys and Compounds*, 618:403–412, 2014.

[2] T.G. Chart. Thermochemical data for transition metal-silicon systems. 5(3):241–252, 1973.

[3] A.J. Zhou, T.J. Zhu, X.B. Zhao, S.H. Yang, T. Dasgupta, C. Stiewe, R. Hassdorf, and E. Mueller. Improved thermoelectric performance of higher manganese silicides with ge additions. *Journal of Electronic Materials*, 39(9):2002–2007, 2010.

[4] A.J. Zhou, X.B. Zhao, T.J. Zhu, S.H. Yang, T. Dasgupta, C. Stiewe, R. Hassdorf, and E. Mueller. Microstructure and thermoelectric properties of sige-added higher manganese silicides. *Materials Chemistry and Physics*, 124:1001–1005, 2010.

[5] X. Chen, A. Weathers, D. Salta, L. Zhang, J. Zhou, J. B. Goodenough, and L. Shi. Effects of (al,ge) double doping on the thermoelectric properties of higher manganese silicides. *Journal of Applied Physics*, 114(17):173705, 2013.

[6] L. M. Levinson. Investigation of the defect manganese silicide mn_nsi_{2n-m}. *Journal of Solid State Chemistry*, 6(1):126–135, January 1973.

[7] G. Zwilling and H. Nowotny. Anisotropy of the electrical conductivity of $mn_{27}si_{47}$. *Monatshefte fur Chemie*, 105(4):666–670, 1974.

[8] I. Kawasumi, M. Sakata, I. Nishida, and K. Masumoto. Crystal growth of manganese silicide, $mnsi_{1.73}$ and semiconducting properties of $mn_{15}si_{26}$. *Journal of Materials Science*, 16(2):355–366, 1981.

[9] A.A. Baikov L.D. Ivanova. Higher manganese silicide based materials. *Journal of Thermoelectricity*, 3:60–66, 2009.

[10] X. Chen, A. Weathers, J. Carrete, S. Mukhopadhyay, O. Delaire, D.A. Stewart, N. Mingo, S.N. Girard, J. Ma, D.L. Abernathy, J. Yan, R. Sheshka, D.P. Sellan, F. Meng, S. Jin, J. Zhou, and L. Shi. Twisting phonons in complex crystals with quasi-one-dimensional substructures. *Nature Communications*, 6:6723, 2015.

[11] I. Engstrom and B. Lonnberg. Thermal expansion studies of the group iv-vii transition-metal disilicides. *Journal of Applied Physics*, 63(9):4476–4484, 1988.

[12] H Kaga, Kinemuchi Y., and Watari K. Fabrication of c-axis oriented higher manganese silicide by a high-magnetic-field and its thermoelectric properties. *Journal of Materials Research*, 22:2917–2923, 2007.

[13] Y. Sadia, Z. Aminov, D. Mogilyansky, and Y. Gelbstein. Texture anisotropy of higher manganese silicide following arc-melting and hot-pressing. *Intermetallics*, 68:71–77, January 2016.

[14] R. E. Garcia and M. D. Vaudin. Correlations between the crystallographic texture and grain boundary character in polycristalline materials. *Acta Materialia*, 55:5728–5735, 2007.

[15] E.D. Specht A. Goyal and D.M. Kroeger. Effect of texture on grain boundary misorientation distributions in polycristalline high temperature superconductors. *Applied Physics Letters*, 68, 1996.

[16] B.D. Powell and D.P. Woodruff. *Phil. Mag.*, 34, 1976.

[17] M.P. Seah and E.D. Hondros. *Proceeding Royal Society*, 1973.

[18] H. Gleiter. The segregation of copper at high angle grain boundaries in lead. *Acta Metallurgica*, 18:117–121, 1970.

[19] A. Joshi. Segregation at selective grain boundaries and its role in temper embrittlement of low alloy steels. *Scripta Metallurgica*, 9:251–260, 1975.

[20] M. Herbig, D. Raabe, Y.J. Li, P. Choi, S. Zaefferer, and S. Goto. Atomic-scale quantification of grain boundary segregation in nanocrystalline material. *Physical review letters*, page 126103, 2014.

Conclusion

This thesis aimed at manufacturing sustainable thermoelectric HMS-based materials for large-scale waste heat harvesting applications with the following characteristics:

- Demonstrated thermoelectric performance for p-type in the temperature range 300-500°C.
- Non-toxic, non-critical and abundant constituting elements.
- High chemical and thermal stability of the material.
- Low raw material cost.

Our approach was based on metallurgical and solid state chemistry concepts which entail that both the structure and the microstructure represent the links to be studied between processes and properties.

The main technological challenge was to develop a manufacturing route to produce $MnSi_{1.73}$ alloys with the right composition and microstructure by means of a reliable and scalable process.

- We have demonstrated the efficiency of the liquid-phase process followed by SPS consolidation to obtain highly dense and homogeneous materials.
- An innovative processing route based on reactive sintering was shown to enhance the performance of the materials thus obtained.
- In order to fabricate crystallographically textured materials, rapid cooling by the melt-spinning technique was successfully applied.

The main scientific challenge was to gain a better understanding of the materials highlights including its commensurability, microstructure and anisotropy in order to optimize the electronic and thermal transport properties.

- A great effort was dedicated to the development of a strategy based on the (3+1)D superspace group approach in order to interpret and index both XRD and electronic diffraction patterns and unequivocally identify HMS phases. We evidenced that several distinct commensurate phases always coexist in as-cast state, and the commensurate-incommensurate transition that occurs, depending of the applied processes. Our results revealed that the liquid-phase processes lead to the formation of a mixture of commensurate HMS phases separated by thin MnSi walls, whereas post-processing and solid state synthesis routes result in the formation of one homogeneous incommensurate phase.

- It was also revealed the relationship between crystallographic texture and transport properties of HMS alloys. Electrical conductivity showed a unique behavior in which the electrical conductivity is independent of the grain orientation for pure (undoped) HMS while it becomes highly sensitive for Ge-doped HMS. Therefore, we evidenced that pure HMS phase (without MnSi striations) presents isotropic transport properties.

- Ashby diagrams were used to track the pathways in the thermoelectric material properties space, the present work stressed the effect of the microstructure, process, doping and texture of the transport properties of HMS. With a thermal conductivity of 2.5 W/m.K, an electrical conductivity of $3.8\ 10^4$ S/m, a Seebeck coefficient of $2.2\ 10^{-4}$ V/K, and a resulting of zT=0.58 at 500°C, our best Ge-doped HMS material compete well with the state-of-the-art.

The above progresses that were made beyond the state-of-art during this thesis provide the following prospects for future works:

- Optimize and scale-up the reactive sintering route based on a easy scalable process to investigate the durability of such processed materials during service use.

- Investigate a new way to enhance the thermoelectric properties through the interplay between texture (control of the grain boundary character) and doping (leading to segregation). The engineering of the anisotropy of the grain boundary with different doping elements could provide new insights for HMS development.

Abstract

Generating electricity from waste heat by means of thermoelectric generators may represent a very interesting opportunity to significantly reduce the impact of road transportation. In this context, Higher Manganese Silicide (HMS) based alloys are studied as p-type semiconductors to achieve a sustainable scale-up of this technology. Through a strategy coupling metallurgy and solid state chemistry, this work revisits the knowledge on HMS and reveals the relationship between the phases, the microstructure and the manufacturing process. This systematic study has lead to the establishment of design guidance to maximize the performance and thus, to a new synthesis route. In addition, the production of grain oriented and highly pure HMS materials evidences the isotropy of the transport properties of HMS. Finally, this study suggests a relationship between grain boundary texture and segregation in doped-HMS, opening new directions for enhancing thermoelectric properties.

Keywords: functional metallurgy, solid state chemistry, Higher Manganese Silicide, thermoelectricity, texture, microstructure, inco/commensurate.

Résumé

Valoriser l'énergie perdue sous forme de chaleur par les moteurs thermiques en électricité via des générateurs thermoélectriques permettrai de diminuer l'empreinte carbone des transports routiers. Une sélection des matériaux basée sur des critères de performance, de coût et de développement durable a conduit au choix du siliciure de manganèse $MnSi_\gamma$ (semi-conducteur de type p). En s'appuyant sur une approche couplant la métallurgie et la chimie du solide, ce travail revisite l'état de l'art sur ces alliages et révèle les relations entre la structure (inco/commensurabilité), la microstructure et le procédé. Une meilleure compréhension de ces liens a permis d'acquérir un contrôle plus précis des microstructures, et par conséquent d'optimiser les propriétés thermoélectriques, et a conduit à la mise au point d'une nouvelle voie de synthèse pour $MnSi_\gamma$. De plus, la production de matériaux purs et texturés a permis de mettre en évidence l'isotropie des propriétés de transport de la phase $MnSi_\gamma$. Enfin, cette étude suggère une relation entre la texture des joints de grains et la ségrégation dans des alliages dopés, ouvrant de nouvelles perspectives pour améliorer les propriétés thermoélectriques.

Mots-clés: Métallurgie fonctionnelle, chimie du solide, siliciures de manganèse, thermoélectricité, texture, microstructure, inco/commensurabilité.